



**Michigan
Technological
University**

Michigan Technological University
Digital Commons @ Michigan Tech

Dissertations, Master's Theses and Master's Reports

2019

OPTIMAL POWER FLOW CONTROL OF NETWORKED DC MICROGRIDS

Eddy H. Trinklein

Michigan Technological University, ehtrinkl@mtu.edu

Copyright 2019 Eddy H. Trinklein

Recommended Citation

Trinklein, Eddy H., "OPTIMAL POWER FLOW CONTROL OF NETWORKED DC MICROGRIDS", Open Access Dissertation, Michigan Technological University, 2019.

<https://doi.org/10.37099/mtu.dc.etr/836>

Follow this and additional works at: <https://digitalcommons.mtu.edu/etr>



Part of the [Acoustics, Dynamics, and Controls Commons](#), [Controls and Control Theory Commons](#), [Electrical and Electronics Commons](#), [Electro-Mechanical Systems Commons](#), and the [Power and Energy Commons](#)

OPTIMAL POWER FLOW CONTROL OF NETWORKED DC MICROGRIDS

By

Eddy H. Trinklein

A DISSERTATION

Submitted in partial fulfillment of the requirements for the degree of

DOCTOR OF PHILOSOPHY

In Mechanical Engineering-Engineering Mechanics

MICHIGAN TECHNOLOGICAL UNIVERSITY

2019

© 2019 Eddy H. Trinklein

This dissertation has been approved in partial fulfillment of the requirements for the Degree of DOCTOR OF PHILOSOPHY in Mechanical Engineering-Engineering Mechanics.

Department of Mechanical Engineering Engineering Mechanics

Dissertation Advisor: *Dr. Gordon G. Parker*

Committee Member: *Dr. Jason R. Blough*

Committee Member: *Dr. Wayne W. Weaver*

Committee Member: *Dr. John E. Beard*

Department Chair: *Dr. William W. Predebon*

Dedication

To my wife Sara and our two beautiful children, Andrew and Amelia.

Contents

List of Figures	xi
List of Tables	xv
Preface	xvii
Acknowledgments	xix
Abstract	xxi
1 Introduction	1
2 Towards Online Optimal Power Flow of a Networked DC Micro- grid System	9
2.1 Networked Microgrid Modeling	10
2.2 Optimal Reference Command Generation Methods	18
2.2.1 Networked Microgrid Steady State Power Flow Form	19
2.2.2 Solution Methods	20
2.2.2.1 All Currents and Duty Cycles	21
2.2.2.2 Interconnection Currents and Duty Cycles	21

2.2.2.3	Lagrange Multipliers	24
2.2.2.4	Interconnection Currents	27
2.2.2.5	Lagrange Multipliers Example	29
2.2.2.6	Interconnection Currents Example	36
2.3	Results and Discussion	37
2.3.1	Increasing Number of Assets Case	40
2.3.2	Increasing Number of Microgrids Case	41
2.4	Conclusions	43
3	Exergy Optimal Multi-Physics Aircraft Microgrid Control Archi-	
	tecture	47
3.1	Networked DC Microgrids with Similar Bus Voltages	48
3.2	Hamiltonian Feed Forward and Feed Back Formulation	53
3.3	Aircraft Microgrid Model	58
3.3.1	Electrical System	59
3.3.2	Pulsed Load and Thermal System	61
3.3.2.1	Lumped Thermal Model	63
3.3.2.2	Coolant Tank	66
3.4	Optimal Electrical Grid Management	67
3.5	Simulation Runs	69
3.5.1	Exergy Based Thermal Management	69

3.5.2	Bus Voltage Regulation Performance Relative to Optimization	
	Update Rate	73
3.6	Conclusions	77
4	Hardware-in-the-Loop Verification of Exergy Optimal Microgrid	
	Control Strategy	79
4.1	Microgrid Model	80
4.1.1	Electrical System - Typhoon HIL	80
4.1.2	Pulsed Load and Thermal System - Opal-RT	83
4.2	Hardware Description	84
4.2.1	Connections Between Equipment	84
4.2.2	Data and Model Synchronization	86
4.2.3	Analog Channel Calibration	87
4.2.4	Online Duty Cycle Bias Determination	89
4.3	Microgrid Control Strategy	92
4.3.1	Hamiltonian Control	93
4.3.2	Thermal Controller	93
4.3.3	Optimizer Implementation	94
4.3.3.1	UDP Ethernet Communication	94
4.4	Results and Discussion	96
4.5	Conclusions and Future Work	105
5	Conclusion and Future Work	107

5.1	Conclusions	107
5.2	Suggestions for Future Work	108
	References	109
A	Letters of Permission	117
A.1	Letter of Permission for Chapter 2	118
B	Support Matrices and Notation For Chapter 3	119
C	Support Tables and Circuit Schematics for Chapter 4	125

List of Figures

2.1	Example of a two-microgrid network illustrating the notation used.	11
2.2	A five state boost converter schematic used to develop the one state models for the optimal reference duty cycle and current strategy development.	12
2.3	One state boost converter averaged model used to connect sources to microgrid buses and microgrid buses to transmission lines of Eq. 2.1 through Eq. 2.4 with idealized net source $u + v$	13
2.4	A two-microgrid networked configuration with one transmission line.	30
2.5	Time-to-solution comparison of reference command generators for the increasing number of assets case. Interconnection is abbreviated as IC.	42
2.6	Time-to-solution comparison of reference command generators for the increasing number of microgrids case. Interconnection is abbreviated as IC.	43
3.1	Microgrid Source Connected Through Boost to Voltage Bus, $v_{i,j} + u_{i,j} < V_{B_j}$	49

3.2	Microgrid Source Connected Through Buck Converter to Voltage Bus, $v_{i,j} + u_{i,j} > V_{B_j}$	50
3.3	buck/Boost Power Converter Architecture with Integral Storage. . .	50
3.4	Aircraft Electrical Distribution System Modeled as Two Networked Microgrids.	59
3.5	Pulsed Load Thermal Model.	64
3.6	Coolant Tank Thermal Model.	67
3.7	Dominant Thermal Model States where $C_t = 3855.9$ kJ/K and $T_{ref} = 104.0$ °C.	72
3.8	System Exergy, Pump Energy, and Tank Temperature as a Function of T_{ref} and C_t	74
3.9	Bus Voltages vs. Optimization Update Rate, dt , where $C_t = 3855.9$ kJ/K and $T_{ref} = 104.0$ °C.	76
4.1	SCADA Interface of Three Bus Interconnected Microgrid Block Dia- gram and based on [1].	81
4.2	Top Level Model Schematic as implemented on the Typhoon HIL 600.	82
4.3	HIL Hardware Setup.	85
4.4	Block Diagram of Co-Simulation and Communication Signal Types.	86
4.5	Calibration Result of Typhoon Analog Channel 1.	88
4.6	Calibration Result of Online Duty Cycle Determination Optimization.	92
4.7	Optimal Duty Cycle Settings vs. Time Varying Load Powers. . . .	98

4.8	Bus Voltage Comparison Of Three Pulses With and Without Optimal Duty Cycle Settings.	102
4.9	Zoomed In View of Bus Voltage Comparison.	103
4.10	Thermal System Response Comparison With and Without Optimal Duty Cycle Settings.	104
A.1	Permission Grant for Chapter 2	118
C.1	Typhoon HIL 600 HPS Generator & MB Bus Schematic.	127
C.2	Typhoon HIL 600 LPS Generator & HP Bus Schematic.	128
C.3	Typhoon HIL 600 MBFC Power Converter Schematic.	128
C.4	Typhoon HIL 600 HPFC Power Converter Schematic.	129
C.5	Typhoon HIL 600 FC Bus Schematic.	129

List of Tables

2.1	Timing Comparison Model Setup	39
3.1	Aircraft Model Electrical Setup	62
3.2	Aircraft Model Thermal System Parameters	63
3.3	Normalized Simulation Timing Study of Optimization Update Rate	75
4.1	Energy Storage Requirements for u_{HESM} and u_{EAU} for 75 Pulses (kJ)	100
4.2	UDP Round Trip Statistics (s)	101
C.1	Opal-RT to Typhoon HIL 600 PWM Connections	125
C.2	Opal-RT to Typhoon HIL 600 Analog Connections	126

Preface

Portions of the research presented in this dissertation were conducted in collaboration with the following co-authors, Dr. Gordon G. Parker, Dr. Micheal D. Cook, Dr. Wayne W. Weaver Jr., and Dr. Rush D. Robinett III. The contributions from each of the authors are discussed per chapter as follows:

Chapter 1: Introduction - was written in collaboration with Dr. Parker where he provided editing support and technical guidance. The portions of content contained in this chapter is submitted to *International Journal of Electrical Power & Energy Systems*.

Chapter 2: Towards Online Optimal Power Flow of a Networked DC Microgrid System - was written in collaboration with Dr. Parker, Dr. Robinett, and Dr. Weaver. Dr. Parker contributed to the modeling and notation, edited the manuscript, and provided technical guidance. Dr. Robinett provided technical comments and reviewed the manuscript. Dr. Weaver provided technical comments and edited the manuscript. The content contained in this chapter was previously published in *IEEE JOURNAL OF EMERGING AND SELECTED TOPICS IN POWER ELECTRONICS* with permission given in Appendix A.

Chapter 3: Exergy Optimal Multi-Physics Aircraft Microgrid Control Architecture - was written in collaboration with Dr. Cook, Dr. Parker and Dr. Weaver. Dr. Cook developed the Hamiltonian controller and edited the manuscript. Dr. Parker developed the initial electro-thermal model, provided technical guidance and reviewed the manuscript. Dr. Weaver provided technical comments and reviewed the manuscript. The content contained in this chapter is submitted to *International Journal of Electrical Power & Energy Systems*.

Chapter 4: Hardware-in-the-Loop Verification of Exergy Optimal Microgrid Control Strategy - was written in collaboration with Dr. Cook, Dr. Parker and Dr. Weaver. Dr. Parker provided technical guidance and edited the manuscript. Dr. Cook and Dr. Weaver provided technical comments and reviewed the manuscript. The content contained in this chapter is submitted to *International Journal of Electrical Power & Energy Systems*.

Acknowledgments

I want to sincerely thank my wife Sara Trinklein. Her support during the writing of this dissertation was incredibly helpful. I'm sure it was trying at times when I spent nights and weekends working while Sara was chasing around Andrew and Amelia.

I thank my parents, Howard and Debra Trinklein, and sister Alison Trinklein, for their continued support and encouragement.

I have been extremely fortunate to have Dr. Gordon Parker as my adviser. Over the past ten years and dozens of projects, his guidance, insight, and patience have truly been a positive experience and one I hope to emulate with my colleagues and students. It has been a pleasure working with you over the years and for the advise, life lessons, stories, and kindness.

I want to thank the members of my Ph.D. committee Jason Blough, John Beard, and Wayne Weaver Jr. I've really enjoyed working with each of you on this and other projects.

I want to thank Dr. John Dexter Bird III who taught me that it can take tremendous effort to accomplish goals and to not give up.

I want to thank Doug and Janet Counts for their support and mentoring especially when I was just starting my education. I appreciated the opportunity to learn hard work ethic, the opportunity to fund my education, and hone my engineering skills through practice.

The interactions, conversations, stories and camaraderie of Trever Hassell and his family, Matthew Heath, Robert Jane, Micheal Cook, and many others have been greatly appreciated and a source inspiration.

This work was supported by the U.S. Department of Defense, Office of Naval Research under the award No. N00014-16-1-3044. The views and conclusions contained in this document are those of the authors and should not be interpreted as representing the official policies, either express or implied, of the Office of Naval Research or the U.S. Government.

Abstract

The US military is moving toward the electrification of many weapon systems and platforms. Advanced weapon systems such as high energy radar, electro-magnetic kinetic weapons and directed energy pose significant integration challenges due to their pulsed power electrical load profile. Additionally, the weapons platforms, including ships, aircraft, and vehicles can be studied as a mobile microgrids with multiple generation sources, loads, and energy storage. There is also a desire to extend the mission profile and capabilities of these systems. Common goals are to increase fuel efficiency, maintaining system stability, and reduce energy storage size as typically required to enable pulsed load devices. To achieve these goals, there is an opportunity to optimize system performance by considering system wide exergy, a measure of the useful energy within the system. By studying exergy, systems with multi-physical coupling, as with electrically pulsed devices that require cooling, the system can be optimized holistically. While numerous optimization approaches exist, many focus on the long term, hours to days, energy management problem. Furthermore, advance control strategies such as the Hamiltonian Surface Shaping Power Flow Controller (HSSPFC) require feedforward operating points about which storage is actuated to maintain stability. Storage size can be reduced by combining the HSSPFC with exergy based optimization strategies designed for sub-second update rates. In this

dissertation, several numerical and closed form/numerical hybrid optimization strategies were developed where speed of solution was explored vs. microgrid asset size, in non-realtime simulation. Then an exergy based optimization strategy was combined with the HSSPFC on a three bus networked microgrid model using average switch mode models, pulse loading, and a thermal system. The three bus model was then extended to a co-simulation on Hardware-in-the-loop (HIL) using an Opal-RT OP5700 and Typhoon HIL 600 realtime simulators, where the optimization was executed asynchronously through UDP Ethernet communication. The storage utilization was reduced by orders of magnitude when comparing two cases of optimized vs. non-optimized generation settings. Bus voltage regulation was within 5 % where there was a trade off between optimization update rate, transient regulation, and storage utilization. Contributions of this work are summarized as follows. An exergy based, asynchronous, optimization strategy was developed to work in concert with the HSSPFC strategy where sub-second update rates were achieved. A co-simulation test bench was developed to allow the study of advanced control strategies through the use of multiple realtime HIL simulators. The methodology for integrating the HIL simulators is given including wiring, calibration, signal scaling, and implementation specific details. An on-line optimization strategy was also developed to interact with the HIL system and used for determining power converter duty cycle biases.

Chapter 1

Introduction¹

A microgrid is a fresh look at an old concept with its origin back the dawn of electrification of the late 1800's [2]. At that time, electricity generation was local, and produced mainly through the use of steam power. Starting in the early 1900's, a great expansion of the electric grid took place leading to consolidation and the interconnection of much US electricity consumers and giving rise to natural monopolies in control of electric generation and distribution [3]. To contrast the ubiquitous monolithic grid, the microgrid is a digression back to local generation and consumption. By definition, a microgrid contains its own generation by means of either fossil or renewable, local electrical loads, energy storage mechanisms and the ability to connect or run islanded from other grids [4].

¹The material contained in this chapter has been submitted to *International Journal of Electrical Power & Energy Systems*.

Examples of existing microgrids can be found throughout the US and abroad. A quintessential civilian microgrid can be found in Alameda County in California where the Santa Rita Jail contains diesel, solar, and wind generation along with fuel cell and battery storage systems [5]. Another civilian microgrid can be found on the campus of University of California at San Diego (UCSD) where a Combine Heat and Power (CHP) unit was installed along with a photovoltaic (PV) array forming a grid connected microgrid [6]. CHP provides building level heating and/or cooling through the use of the waste heat produced by a co-generation unit while also meeting electrical needs. CHP substantially offsets operating costs making installations financially attractive [7], [8]. In military operations, microgrids occur by necessity in Forward Operation Base (FOB) camps where connection to an existing grid is not possible [9]. The modernization of the US navy has lead to electrification of ship's subsystems and their structure resembles a microgrid's architecture [10, 11, 12, 13].

The example microgrids listed above have an alternating current (ac) distribution system. This inevitably begs the question of whether direct current (dc) microgrids should be considered when much of the existing infrastructure is based on alternating current. The relevance of dc vs. ac distribution, similar to the original concept of microgrids, dates back to the days of Thomas Edison who was a proponent of dc, while Nikola Tesla and George Westinghouse favored ac. Ultimately, ac distribution won the argument, partly due to the technological limitations of the time and partly due to concerns of safety and economics. Recently however, high power switching electronics,

based on silicon or silicon-carbide, are enabling a redesign of grid structures and allowing microgrids to use dc for distribution. Furthermore, dc distribution has the potential for higher efficiency as compared to ac based microgrids if the primary generation sources are also inherently dc, such as fuel cells and PV [14]. A microgrid with rotary generation sources, such as fossil fuel diesel or wind turbines, will require at least one conversion from ac to dc before feeding into a dc distribution system. In this work, the grid models will be considered agnostic to energy conversion mechanism which represent the dc sources. Similar to ac systems, when transferring dc long distance or between grids, utilizing high voltages minimizes resistive power dissipation and reduces economic costs [15]. This suggests that if multiple microgrids were to be connected, the interconnections should use voltages higher than their local operating bus voltages.

A natural expansion of the individual microgrid is the networking of multiple microgrids for the purpose of enhanced resiliency, stability, and ancillary services to enhanced power quality [16, 17, 18]. This networking of microgrids in the literature occurs at both large scale state sized connections greater than 45 MW as in [19, 20, 21] and less than 45 MW local distribution feeder sized networked microgrids as described by Sousa in [22].

An explanation of how microgrid networking could occur is given by Trinklein [23] as: “Networking of individual microgrids could occur by electrically connecting the distribution buses of two or more microgrids by high voltage interconnections to allow shared generation assets among the loads within this new network. The microgrids would then need a power flow coordinating control scheme to dictate how to best utilize the combined generation assets, stabilize the system, and maintain bus voltage specifications. Networked microgrids could operate individually or coordinated depending on overall operation goals, such as maximizing system efficiency. An example of maximizing efficiency would be operating a majority energy sources near or at their individual peak efficiency while maintaining power flow and bus voltage constraints. Furthermore, networking enhances system operational flexibility and allow for scheduled maintenance of local generation assets while other networked generation assets cover the system loads. The cost of networking lies with additional power electronics for interconnection, additional communication links, control hardware and software.”

Optimal power flow coordination between generation assets, on existing grids utilize numerical optimization approaches focused on hour or longer time horizon solutions. In work by Fazlollahi et al. [24], economics, emissions and grid efficiency are optimized through generation asset placement and daily energy planning. A multiple objective optimization strategy was explored by Sousa et al. [22] where a trade off is considered between operating costs and voltage regulation. While the number of generation and load assets studied were in the thousands, suggesting a scalable solution,

solution time or expected update rates were not provided. Another multiple objective strategy focusing on fuel costs, emissions, voltage variation, and power losses was examined by Ghasemi et al. [25] where economic considerations were the central focus. The optimization was designed long term power planning and solution times were 25 to 58 seconds depending on algorithm employed and grid size. Another economic based optimization was studied by Neves et al. [26], where demand response was exercised through dispatchable solar/thermal or heat pump systems. The system was load dominated with 144 loads and four diesel generators. A 24 hour planning window was used and solution time wasn't examined. Economic and generation emissions were the focus of optimization by Elsie [27]. Scalability and a flexible grid architecture were not considered. In these cases, the time to solution is less important due to the relatively slow generation response time and aggregate load rates on the order of seconds to hours. The time delay between a load change on a networked microgrid and implementing an optimal solution was studied in [28], where bus regulation was improved. Considering networked microgrids and modern power electronics which enable them, sub-second dynamic response times are expected [29, 30]. This will require a new paradigm in control methodology to leverage optimization strategies to improve grid operation at smaller time scales. Furthermore, the operation of microgrids with multiple sources will require a methodology for balancing its generation resources, lending itself to optimization techniques.

Many systems have multi-physical dynamics that interact and require management. For example, power converters used in microgrids have electrical and thermal requirements which must be controlled to ensure proper operation. One way to optimize electro-thermal systems together is to consider system wide exergy destruction. Exergy destruction is the dissipation of useful energy through irreversible entropy production. In electrical systems, a source of exergy destruction is resistive i^2R losses. An example of exergy dissipation in thermal systems would be dissipation of energy by conduction or convection within a cooling system. Exergy optimization was shown to improve the efficiency of HVAC systems [31], improve the performance of internal combustion engines [32] and reduce fossil fuel usage [33].

The recent popularity of pulsed load devices, such as radar, lasers [34], electromagnetic kinetic weapons [35] has presented a challenge for integration into electrical networks. A key enabler has been to incorporate distributed storage at point of consumption to stabilize bus voltages during load transients. Advanced control schemes, such as the Hamiltonian Surface Shaping Power Flow Control [36] or just Hamiltonian controller, are designed to actuate the distributed storage and provide stability guarantees. However, the Hamiltonian controller requires feedforward generation settings to avoid excessive storage capacity and utilization. There is an inverse trade-off between the rate at which generation set point changes are implemented and required storage capacity. Additionally, optimization based control schemes enable power balancing among multiple generation sources and to achieve other objectives such as

minimizing exergy destruction. To be effective at reducing storage size, the implementation of the optimization scheme must be efficient. In this paper, an exergy based optimization control scheme is demonstrated on a microgrid model that is co-simulated on two real-time HIL simulators.

Chapter 2

Towards Online Optimal Power

Flow of a Networked DC Microgrid

System ¹

In this chapter, the intent is to bring the concept of energy management from the minutes to hours time frame down to the sub-second level. This will reduce the energy storage size required for pulse load implementation, allow optimizing a system

¹In reference to IEEE copyrighted material which is used with permission in this thesis, the IEEE does not endorse any of Michigan Technological University's products or services. Internal or personal use of this material is permitted. If interested in reprinting/republishing IEEE copyrighted material for advertising or promotional purposes or for creating new collective works for resale or redistribution, please go to http://www.ieee.org/publications_standards/publications/rights/rights_link.html to learn how to obtain a License from RightsLink. A permission letter can be found in Appendix A.

holistically from an electrical perspective, and provide feedforward power flow generation set points as required by the HSSPFC. To this end, the possibility of extending a closed form solution used for multiple generation assets on single microgrids to networked microgrids was explored. A closed form solution could be orders of magnitude faster than pure numerical approaches, but was not found. Instead, the power flow solution was divided into closed form and numerical hybrid approaches where three such algorithms were developed and compared to a pure numerical approach. The scalability of four optimization techniques were studied as compared to number of networked microgrids and generation assets. The kernel of each optimization technique was to determine exergy optimal set point commands for any networked microgrid configuration based on i^2R losses within each power converter. The dynamic equations were assumed to have reached steady state and storage inputs considered to be zeroed driving the generation sources to meet electrical demand. This chapter forms the theoretical foundation for the remaining chapters using simplified average mode power converters and neglecting thermal electrical coupling later developed in Chapter 3 and further refined in Chapter 4.

2.1 Networked Microgrid Modeling

A scalable networked microgrid simulation, described in [37], was developed in MATLAB & Simulink that allows for the study of control and optimization algorithms

including their scalability effects. An example microgrid network illustrating the nomenclature used in the subsequent equation development is shown in Figure 2.1. In this example, both microgrid buses have two sources, and each microgrid bus is connected to two transmission lines. The microgrids' low voltage sources provide current to their higher bus voltage microgrids through boost converters. The microgrids are in turn supplying current to higher voltage transmission lines, again through boost converters.

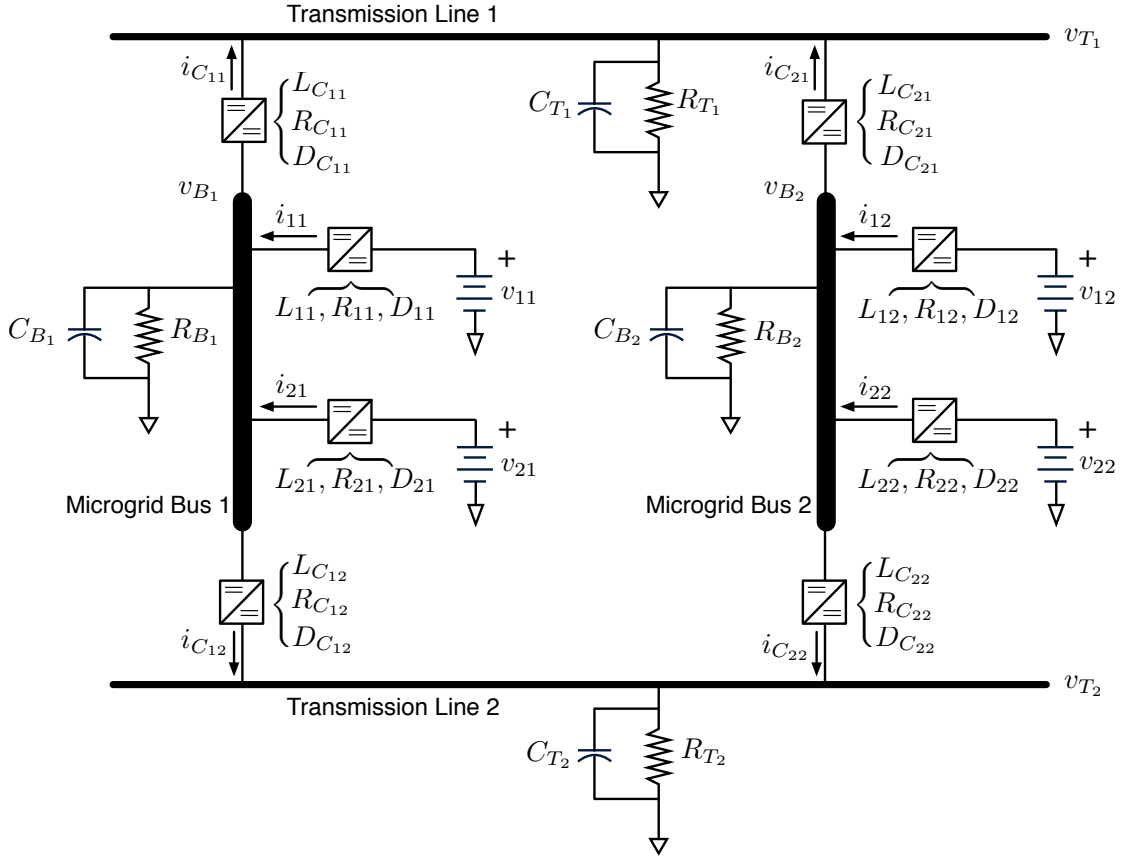


Figure 2.1: Example of a two-microgrid network illustrating the notation used.

The converter models, used for the optimal power apportionment strategy developed in Section 2.2, are based on a reduced order version of the five-state boost converter model schematic shown in Figure 2.2. The one-state model is shown in Figure 2.3 and exploits the following assumptions:

1. The converter is located close to the source, v . Therefore, the parasitic line effects (R_{line} , L_{line} , C_{line}) can be considered negligible.
2. The converter is also located close to the dc bus. Therefore, the parasitic line effects (R_{out} , L_{out}) can also be considered negligible. The output capacitance of each converter C_{out} can then be lumped into the total single capacitance of the bus C_l .

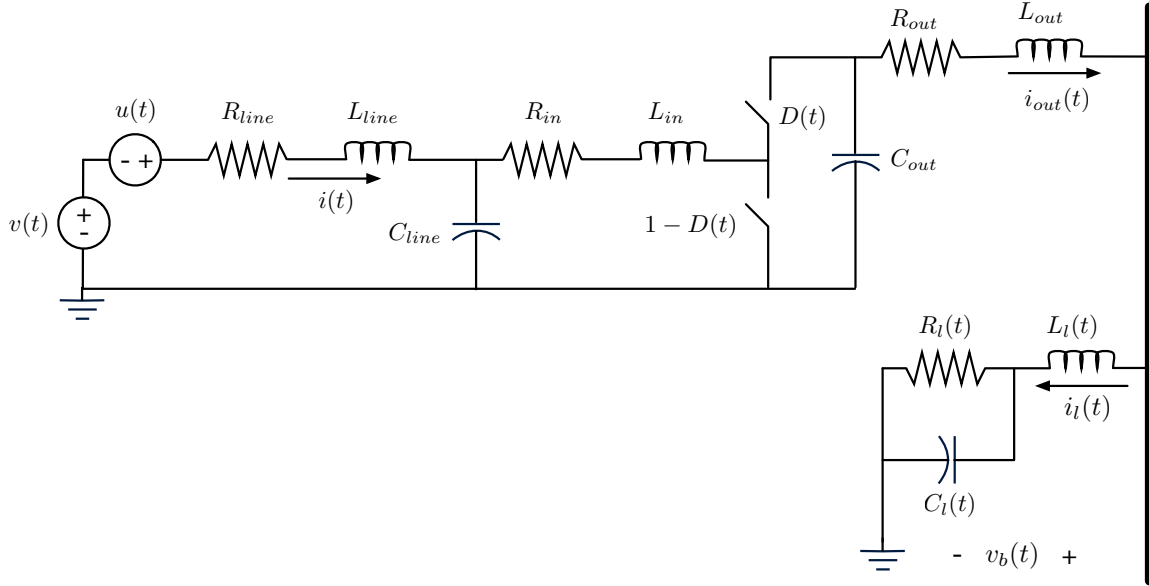


Figure 2.2: A five state boost converter schematic used to develop the one state models for the optimal reference duty cycle and current strategy development.

This model form was recently used for developing an optimal power flow solution for a single microgrid where both transient and steady-state responses were examined on a hardware-in-the-loop (HIL) simulation [38]. The HIL simulation used, switching converter models illustrating that a one-state boost converter model was adequate for computing power flow solutions. It was also used to examine the effect of invalid information exchange between assets for a single dc microgrid when using the HSSPFC scheme [39].

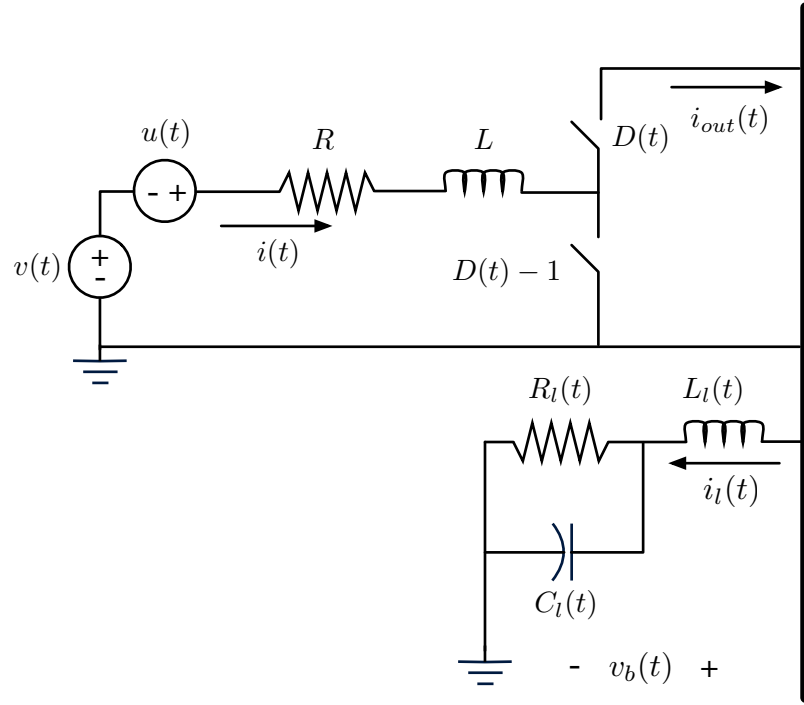


Figure 2.3: One state boost converter averaged model used to connect sources to microgrid buses and microgrid buses to transmission lines of Eq. 2.1 through Eq. 2.4 with idealized net source $u + v$.

The networked dc microgrid differential equations, developed in [37], are given in Eq. 2.1 through Eq. 2.4. They can be used to model any topology consisting of p microgrids connected to q transmission lines. The $p \times q$, boolean matrix, E , defines

how the microgrids and transmission lines are connected while the elements of the p -dimensional vector \underline{m} specify the number of distributed generation assets in the j th microgrid. In a similar manner, the elements of the p -dimensional vector \underline{m}_L define the number of unique resistive loads on each microgrid. Each transmission line and microgrid also have a net load represented by a parallel resistive and capacitive element. Equation 2.1 is the source-to-microgrid, averaged boost converter equation based on the lumped model of Figure 2.3. The model allows the microgrid-to-transmission line boost converters to switch their current direction. Therefore, Eq. 2.2 through Eq. 2.4 are given as two cases with either the microgrid bus voltage higher than the transmission line voltage $v_{T_k} \leq v_{B_j}$ or the reverse of this where $v_{T_k} > v_{B_j}$. Equation 2.2 is the microgrid-to-transmission line boost converter model. Equations 2.3 and 2.4 are the microgrid and transmission line load equations.

The distributed generation assets attached to the microgrids are shown with voltages $v_{ij} + u_{ij}$ in Eq. 2.1 indicating the net combination of sources (e.g. fossil fuel generators or renewables) and stored energy (e.g. chemical or mechanical). It is assumed that an inner control system is managing storage and so the sum is available to the network to manage the loads. This inner and outer level control approach is described in [40] and [41]. The objective of the optimal power apportionment strategy is to compute a set of feedforward reference current and duty cycle settings such that the p microgrid bus voltages and the q transmission line voltages are maintained in the presence of time-varying source voltages and electrical loads. It is further assumed that the dynamic

response of the microgrid is significantly faster than the source and load variations and so the right sides of Eq. 2.1 through Eq. 2.4 can be set to zero resulting in a set of $\sum_{j=1}^p \underline{m}_j + \sum_{j=1}^p \sum_{k=1}^q E_{jk} + p + q$ coupled algebraic equations with $2 \sum_{j=1}^p \underline{m}_j + 2 \sum_{j=1}^p \sum_{k=1}^q E_{jk}$ unknowns in the $\sum_{j=1}^p \underline{m}_j$ duty cycles, D_{ij} , the $\sum_{j=1}^p \underline{m}_j$ currents, i_{ij} , the $\sum_{j=1}^p \sum_{k=1}^q E_{jk}$ duty cycles of the converter connections between microgrids and transmission lines, $D_{C_{jk}}$, and their $\sum_{j=1}^p \sum_{k=1}^q E_{jk}$ currents, $i_{C_{jk}}$. In summary, when $2 \sum_{j=1}^p \underline{m}_j + 2 \sum_{j=1}^p \sum_{k=1}^q E_{jk} > p + q$ there is the possibility of creating a power flow solution that satisfies all of the algebraic equations while minimizing a specified objective function. In the remainder of this paper we'll develop several solutions to the optimal power apportionment problem that satisfy the steady state version of Eq. 2.1 through Eq. 2.4 while minimizing the power lost in the parasitic resistances.

Let

- L_{ij} = i^{th} boost converter (BC) inductance on the j^{th} microgrid bus [H]
- i_{ij} = i^{th} BC current on the j^{th} microgrid bus [A]
- R_{ij} = i^{th} BC resistance on the j^{th} microgrid bus [Ω]
- D_{ij} = i^{th} BC duty cycle on the j^{th} microgrid bus [%]
- v_{ij} = i^{th} BC source voltage on the j^{th} microgrid bus [V]
- u_{ij} = i^{th} BC storage voltage on the j^{th} microgrid bus [V]
- C_{Bj} = j^{th} microgrid bus capacitance [F]
- R_{Bj} = j^{th} microgrid load [Ω]
- v_{Bj} = j^{th} microgrid bus voltage [V]
- R_{Lj} = j^{th} microgrid additional loads [Ω]
- u_{Bj} = j^{th} microgrid storage [A]
- i_{Cjk} = connection current between the j^{th} microgrid bus and the k^{th} transmission line [A]
- L_{Cjk} = connection inductance between the j^{th} microgrid bus and the k^{th} transmission line [H]
- R_{Cjk} = connection resistance between the j^{th} microgrid bus and the k^{th} transmission line [Ω]
- D_{Cjk} = connection duty cycle between between the j^{th} microgrid bus and the k^{th} transmission line [%]
- u_{Cjk} = connection storage between the j^{th} microgrid bus and the k^{th} transmission line, [V]
- C_{Tk} = k^{th} transmission line capacitance [F]
- R_{Tk} = k^{th} transmission line load [Ω]
- u_{Tk} = k^{th} transmission line storage [A]
- p = number of microgrids [nondimensional (n.d.)]
- q = number of transmission lines [n.d.]
- \underline{m}_j = number of BCs connected to the j^{th} microgrid bus [n.d.]
- m_{Lj} = number of additional resistive loads on the j^{th} microgrid bus [n.d.]
- E_{jk} = $p \times q$ connectivity matrix defining the connections between the j^{th} microgrid bus and k^{th} transmission line. $E_{jk} = 1$ means that microgrid j is connected to transmission line k and $E_{jk} = 0$ means they are disconnected [n.d.]

$$L_{ij} \frac{di_{ij}}{dt} = -R_{ij} i_{ij} - D_{ij} v_{Bj} + v_{ij} + u_{ij}, \quad (2.1)$$

$$i = 1 \dots \underline{m}_j, \quad j = 1 \dots p$$

$$L_{C_{jk}} \frac{di_{C_{jk}}}{dt} = \begin{cases} -R_{C_{jk}} i_{C_{jk}} - D_{C_{jk}} v_{T_{jk}} + v_{Bj} + u_{C_{jk}}, & v_{T_k} > v_{Bj}, \\ -R_{C_{jk}} i_{C_{jk}} + v_{T_k} - D_{C_{jk}} v_{Bj} + u_{C_{jk}}, & v_{T_k} \leq v_{Bj}, \end{cases} \quad (2.2)$$

$$j = 1 \dots p, \quad k = 1 \dots q \quad \forall \quad E_{jk} \neq 0$$

$$C_{Bj} \frac{dv_{Bj}}{dt} = \begin{cases} \sum_{i=1}^{\underline{m}_j} D_{ij} i_{ij} - \frac{v_{Bj}}{R_{Bj}} - \sum_{i=1}^{m_{Lj}} \frac{v_{Bj}}{R_{Li}} + u_{Bj} - \sum_{\substack{k=1 \\ E_{jk} \neq 0}}^q i_{C_{jk}}, & v_{T_k} > v_{Bj}, \\ \sum_{i=1}^{\underline{m}_j} D_{ij} i_{ij} - \frac{v_{Bj}}{R_{Bj}} - \sum_{i=1}^{m_{Lj}} \frac{v_{Bj}}{R_{Li}} + u_{Bj} + \sum_{\substack{k=1 \\ E_{jk} \neq 0}}^q D_{C_{jk}} i_{C_{jk}}, & v_{T_k} \leq v_{Bj}, \end{cases}$$

$$j = 1 \dots p \quad (2.3)$$

$$C_{T_k} \frac{dv_{T_k}}{dt} = \begin{cases} \sum_{\substack{j=1 \\ E_{jk} \neq 0}}^p D_{C_{jk}} i_{C_{jk}} - \frac{v_{T_k}}{R_{T_k}} + u_{T_k}, & v_{T_k} > v_{B_j}, \\ - \sum_{\substack{j=1 \\ E_{jk} \neq 0}}^p i_{C_{jk}} - \frac{v_{T_k}}{R_{T_k}} + u_{T_k}, & v_{T_k} \leq v_{B_j}, \end{cases} \quad (2.4)$$

$$k = 1 \dots q$$

2.2 Optimal Reference Command Generation

Methods

Minimizing electrical losses, and thus minimizing fuel consumption for fossil fuel generation, is a typical microgrid management objective [25], [26]. Therefore, the objective function of Eq. 2.5, introduced in [38], that minimizes lost energy through parasitic resistances internal to the boost converters is used.

$$J = \sum_{j=1}^p \sum_{i=1}^{\underline{m}_j} R_{ij} i_{ij}^2 + \sum_{j=1}^p \sum_{\substack{k=1 \\ E_{jk} \neq 0}}^q R_{C_{jk}} i_{C_{jk}}^2 \quad (2.5)$$

2.2.1 Networked Microgrid Steady State Power Flow Form

To aid the solution, the networked microgrid equations are formulated in terms of power and a steady state assumption is imposed. Multiplying the steady-state version of Eq. 2.1 through 2.4 by i_{ij} , $i_{C_{jk}}$, v_{B_j} , and v_{T_k} results in a power representation of the networked microgrid equations, shown in Eq. 2.6 through Eq. 2.9.

$$0 = -R_{ij}i_{ij}^2 - P_{ij} + v_{ij}i_{ij}, \quad i = 1 \dots \underline{m}_j, \quad j = 1 \dots p \quad (2.6)$$

$$0 = \begin{cases} -R_{C_{jk}}i_{C_{jk}}^2 - P_{C_{jk}} + v_{B_j}i_{C_{jk}}, & v_{T_k} > v_{B_j}, \\ -R_{C_{jk}}i_{C_{jk}}^2 + v_{T_k}i_{C_{jk}} - P_{C_{jk}}, & v_{T_k} \leq v_{B_j}, \end{cases} \quad (2.7)$$

$$j = 1 \dots p, \quad k = 1 \dots q \quad \forall \quad E_{jk} \neq 0$$

$$0 = \phi_{B_j} = \sum_{i=1}^{\underline{m}_j} P_{ij} - P_{B_j} - \sum_{i=1}^{\underline{m}_{Lj}} P_{BL_{ij}} - \sum_{\substack{k=1 \\ E_{jk} \neq 0 \\ v_{T_k} > v_{B_j}}}^q i_{C_{jk}}v_{B_j} + \sum_{\substack{k=1 \\ E_{jk} \neq 0 \\ v_{T_k} \leq v_{B_j}}}^q P_{C_{jk}}, \quad j = 1 \dots p \quad (2.8)$$

$$0 = \phi_{T_k} = \sum_{\substack{j=1 \\ E_{jk} \neq 0 \\ v_{T_k} > v_{B_j}}}^p P_{C_{jk}} - \sum_{\substack{j=1 \\ E_{jk} \neq 0 \\ v_{T_k} \leq v_{B_j}}}^p i_{C_{jk}} v_{T_k} - P_{T_k}, \quad k = 1 \dots q \quad (2.9)$$

The power transfer between sources and microgrids, P_{ij} , and between microgrids via transmission lines, $P_{C_{jk}}$, are shown in Eq. 2.10 and Eq. 2.11 and are unknowns.

$$P_{ij} = D_{ij} v_{B_j} i_{ij} \quad (2.10)$$

$$P_{C_{jk}} = \begin{cases} D_{C_{jk}} v_{T_k} i_{C_{jk}}, & v_{T_k} > v_{B_j} \\ D_{C_{jk}} v_{B_j} i_{C_{jk}}, & v_{T_k} \leq v_{B_j} \end{cases} \quad (2.11)$$

The resistive losses, $P_{B_j} = v_{B_j}^2 / R_{B_j}$, $P_{BL_{ij}} = v_{B_j}^2 / R_{L_i}$ and $P_{T_k} = v_{T_k}^2 / R_{T_k}$ are known since the microgrid and transmission line nominal voltages, v_{B_j} and $v_{T_{jk}}$, are known.

2.2.2 Solution Methods

Four methods are developed below to obtain the optimal power apportionment solution. They have different properties, as will be seen through an example, in terms of their solve time and physical interpretation. It would be tempting to only focus on

the most computationally efficient approach, but it may be of interest to grid management designers to see the trade-offs between computational requirements and physical insight. Two of the more complex algorithms are explained through a small example to illustrate the process. The first method is the most general and its solution can be implemented with an numerical optimization algorithm that allows equality constraints. The other three methods reduce the numerical problem size by leveraging the quadratic form of the objective function to combine numerical and closed form solution methods.

2.2.2.1 All Currents and Duty Cycles

A straightforward approach to the optimization task was implemented by solving for the $2 \sum_{j=1}^p \underline{m}_j + 2 \sum_{j=1}^p \sum_{k=1}^q E_{jk}$ unknowns in D_{ij} , $D_{C_{jk}}$, i_{ij} , and $i_{C_{jk}}$ boost converter duty cycles and currents. Eq. 2.6 through Eq. 2.9 are implemented as constraint equations while minimizing the objective function Eq. 2.5. This approach is considered the baseline for timing comparisons in Section 2.3.

2.2.2.2 Interconnection Currents and Duty Cycles

Investigation of expanding the closed form solution found in [38] of the single microgrid topology to the networked microgrid topology is confounded by the coupling

introduced in Eq. 2.3. These p equations can in general contain both source-to-microgrid currents, i_{ij} , and microgrid-to-transmission line currents, $i_{C_{ij}}$. An increase in performance was found by applying the closed form solution for the individual microgrid buses and a numerical approach for the connection $D_{C_{ij}}$ duty cycles and $i_{C_{ij}}$ currents. This reduces the number of free variables to $2 \sum_{j=1}^p \sum_{k=1}^q E_{jk}$, which reduces computation time for topologies with large quantities of distributed generation and like the full solution, a feasible solution is always generated.

The individual microgrid buses can be solved closed form if the P_{ij} power flow is known for each bus. Observing Eq. 2.6, there are $\sum_{j=1}^p \underline{m}_j$ quadratic equations in terms of the currents i_{ij} . Solving for the currents, and using the negative solution gives $i_{ij}(P_{ij})$ shown in Eq. 2.12 where at this point the P_{ij} are unknowns. Of the two possible i_{ij} solutions, this one ensures i_{ij} has the smallest magnitude and thus the proper choice for reducing power consumed by parasitic resistances. When $P_{ij} > 0$ power flows from the generators to their microgrids. While this is considered the nominal operating condition, it's important to note that flowing current from the microgrid to a generator is a possible scenario if distributed storage is co-located with the generator, and it is desired to increase the state-of-charge of the energy storage system when the generator is not producing power. That case is easily accommodated with a negative P_{ij} . The microgrid buses in Eq. 2.8 can be rearranged and solved for P_{ij} , where we introduce a new term of requested power $P_{r_{ij}}$ between each microgrid and transmission line. Since the closed form solution is computed each iteration of

the numerical optimization process, the $D_{C_{ij}}$ duty cycles and $i_{C_{ij}}$ currents are known and allow solution of the optimal boost converter currents of Eq. 2.12 and their duty cycles using Eq. 2.10. In summary, the steps for the Interconnection Currents and Duty Cycles approach are:

1. Choose a set of $P_{r,j}$ connection power flow requests of Eq. 2.14. This requires solving the transmission and connection constraints, Eq. 2.7 and 2.9 respectively.
2. Calculate the closed form solution for each P_{ij} microgrid boost converter power of Eq. 2.13.
3. Calculate the objective function of Eq. 2.5, then iterate on Steps 1-3 using a numerical optimization algorithm until the minimum objective function value is found.
4. Determine the optimal boost converter currents i_{ij}^* with the solution obtained in step three using Eq. 2.12.
5. Calculate the optimal boost converter duty cycles from Eq. 2.10.

$$i_{ij}^* = \frac{v_{ij} - \sqrt{v_{ij}^2 - 4R_{ij}P_{ij}}}{2R_{ij}}, \quad (2.12)$$

$$i = 1 \dots \underline{m}_j, \quad j = 1 \dots p$$

$$P_{ij} = \frac{v_{ij}^2 (v_{B_j}^2 / R_{B_j} + P_{r,j} + v_{B_j}^2 R_{L_i} / \sum_{i=1}^{m_{L_j}})}{R_{ij} \sum_{i=1}^{m_j} \frac{v_{ij}^2}{R_{ij}}} \quad (2.13)$$

$$i = 1 \dots \underline{m}_j, \quad j = 1 \dots p$$

$$P_{r,j} = \sum_{\substack{k=1 \\ E_{jk} \neq 0 \\ v_{T_k} > v_{B_j}}}^q i_{C_{jk}} v_{B_j} - \sum_{\substack{k=1 \\ E_{jk} \neq 0 \\ v_{T_k} \leq v_{B_j}}}^q P_{C_{jk}}, \quad j = 1 \dots p \quad (2.14)$$

The utility of this approach is to reduce the number of computations required to calculate optimal control reference points for a networked microgrid system. An interesting result is each microgrid can operate locally optimally based on the requested power flow commands. This provides a method to reduce the optimization problem size down to the microgrid level.

2.2.2.3 Lagrange Multipliers

The approach described below requires the solution of $p + q$ nonlinear, coupled equations to obtain the optimal power apportionment solution. While this sounds daunting, it's important to note that the dominant computational complexity is invariant with respect to topology changes and is only dependent on the total number of participating microgrids and transmission lines. Furthermore, the reduced form of the

equations no longer requires a constrained optimization approach for solution because the constraints are integrated. Therefore, a numerically efficient nonlinear least squares solver can be applied to this approach.

The method begins with noticing that Eq. 2.7 consists of $\sum_{j=1}^p \sum_{k=1}^q E_{jk}$ quadratic equations in the currents $i_{C_{jk}}$ and they can be solved as shown in Eq. 2.15 where they are functions of the power $P_{C_{jk}}$. Again, the negative solution is used yielding the smallest current magnitude, and thus the lowest resistive losses.

$$i_{C_{jk}} = \begin{cases} \frac{v_{B_j} - \sqrt{v_{B_j}^2 - 4R_{C_{jk}}P_{C_{jk}}}}{2R_{C_{jk}}}, & v_{T_k} > v_{B_j} \\ \frac{v_{T_k} - \sqrt{v_{T_k}^2 - 4R_{C_{jk}}P_{C_{jk}}}}{2R_{C_{jk}}}, & v_{T_k} \leq v_{B_j} \end{cases} \quad (2.15)$$

$$j = 1 \dots p, \quad k = 1 \dots q \quad \forall \quad E_{jk} \neq 0$$

Equations 2.12 and 2.15 can be substituted into the objective function, Eq. 2.5, resulting in $J(P_{ij}, P_{C_{jk}})$ thus removing any explicit dependence of J on the currents. Similarly, Eq. 2.15 can be substituted into the constraints of Eq. 2.8 and Eq. 2.9 resulting in $\phi_{B_j}(P_{ij}, P_{C_{jk}}) = 0$ and $\phi_{T_k}(P_{ij}, P_{C_{jk}}) = 0$ and again, having no explicit dependence on currents.

The optimal power values, P_{ij}^* and $P_{C_{ij}}^*$, must satisfy the necessary conditions of

Eq. 2.16 where the Hamiltonian, H is given in Eq. 2.17 where the $p + q$ Lagrange multipliers, λ_{B_j} and λ_{T_k} , have been introduced.

$$\begin{aligned} \frac{\partial H}{\partial P_{ij}} &= 0, \quad i = 1 \dots \underline{m}_j, \quad j = 1 \dots p \\ \frac{\partial H}{\partial P_{C_{ij}}} &= 0, \quad j = 1 \dots p, \quad k = 1 \dots q \text{ and } E_{jk} \neq 0 \end{aligned} \quad (2.16)$$

$$H = J + \sum_{j=1}^p \lambda_{B_j} \phi_{B_j} + \sum_{k=1}^q \lambda_{T_k} \phi_{T_k} \quad (2.17)$$

Application of the necessary conditions of Eq. 2.16 allows the P_{ij}^* and $P_{C_{ij}}^*$ to be expressed in terms of the $p + q$ optimal Lagrange multipliers, in particular, $P_{ij}^* = P_{ij}(\lambda_{B_j}^*)$ and $P_{C_{ij}}^* = P_{C_{ij}}(\lambda_{B_j}^*, \lambda_{T_k}^*)$. Now that the optimal power expressions' explicit dependence is only on the Lagrange multipliers, they can be back substituted into the constraint equations, Eq. 2.8 and Eq. 2.9. This leaves $p + q$, nonlinear, coupled equations, $\phi_{B_j}(\lambda_{B_j}^*, \lambda_{T_k}^*) = 0$ and $\phi_{T_k}(\lambda_{B_j}^*, \lambda_{T_k}^*) = 0$. The optimal duty cycle and current values can be computed by first solving ϕ_{B_j} and ϕ_{T_k} for the optimal Lagrange multipliers $\lambda_{B_j}^*$ and $\lambda_{T_k}^*$, then substituting those values into the power expressions $P_{ij}^* = P_{ij}(\lambda_{B_j}^*)$ and $P_{C_{ij}}^* = P_{C_{ij}}(\lambda_{B_j}^*, \lambda_{T_k}^*)$. The optimal power values can then be used to compute the optimal currents from Eq. 2.12 and Eq. 2.15, and finally, the optimal duty cycle settings, D_{ij}^* and $D_{C_{ij}}^*$ are found from Eq. 2.10 and Eq. 2.11. The

$p + q$ nonlinear equations do not, in general, have a closed form solution and thus require a numerical solution approach.

2.2.2.4 Interconnection Currents

A more physical solution is given in this last approach and yields the same optimal power solution above. It also has the attractive feature of always producing a feasible solution. The price paid for these benefits is an increase in computational complexity. The method requires a numerical optimization solver to find $r = \sum_{j=1}^p \sum_{k=1}^q E_{jk} - q$ free variables representing a subset of the currents flowing between microgrids and transmission lines. After selecting values for the currents, the net power flow for each microgrid can be computed using a combination of Eq. 2.7, Eq. 2.8 and Eq. 2.9. Having established the power flow requirements for each microgrid, the optimal power apportionment for each microgrids' distributed generation can be computed using the solution presented in Section 2.2.2.2, specifically Eq. 2.12 through Eq. 2.14. Although the set of p solutions are locally optimal, the overall solution is optimal according to Bellman's *Principal of Optimality* [42]. This view alters the interpretation of Eq. 2.8 to being a power balance between the distributed generation and the microgrid's net power flow.

The process above can be implemented algorithmically for any connection scenario using the connectivity matrix E introduced earlier. A key part of the algorithm is to

assure that the currents selected for optimization do not over constrain a solution. To illustrate this consider the j th column of E which represents the connections between all the microgrids and the j th transmission line. An unacceptable set of currents, to be used for optimization, would be all currents associated with all the 1 elements of a column of E . More specifically, there needs to exist at least one current, associated with a 1 in a column of E , that is not used during the optimization process and can be used to enforce a constraint caused by Eq. 2.7 or Eq. 2.8. This observation motivates the algorithm for selecting the optimization currents and for solving for all the microgrid power flows and remaining currents that are not selected during the optimization process.

1. Define the k th column sum of E as $a_k = \sum_{j=1}^q E_{jk}$. For each of E 's k columns select the current corresponding to the $a_k - 1$ rows containing a 1. One approach is to start at the top of each column and continue selecting currents until the second to last 1 is reached. At this point an appropriate set of r currents have been selected for optimization. The remaining q currents are a function of the selected currents and will be resolved out.
2. Solve Eq. 2.7 for the $P_{C_{jk}}$ corresponding to the r currents in step 1.
3. Substitute the $P_{C_{jk}}$ powers from Step 2 into Eq. 2.8 or Eq. 2.9 corresponding to q the currents.
4. Solve the new Eq. 2.8 or Eq. 2.9 for the q currents, $i_{C_{jk}}$ using Eq. 2.15.

5. Solve Eq. 2.14 for $P_{r,j}$, then Eq. 2.13 for P_{ij}
6. Solve for the distributed generation currents, i_{ij} , using Eq. 2.12.
7. Compute the objective function of Eq. 2.5.

Once the power flows are established for each of the microgrids, the currents for all the distributed assets i_{ij} are computed that are optimal for each microgrid. Since the objective function J contains all the lost power terms for the entire grid the r currents determined by the numerical optimization process are optimal. This algorithm and the Lagrange Multipliers method are illustrated below for a simple example.

2.2.2.5 Lagrange Multipliers Example

The two-microgrid system, shown in Figure 2.4, is used to illustrate the Lagrange Multipliers strategy and later the Interconnection Currents approach. Consider a network where $p = 2$, $q = 1$, $\underline{m} = [2 \ 2]$, and $E = [1 \ 1]^T$. In addition $v_{B_1} < v_{T_1}$ and $v_{B_2} > v_{T_1}$. Applying Eq. 2.6 through Eq. 2.9 to this example results in the nine power balance equations of Eq. 2.18 through Eq. 2.21.

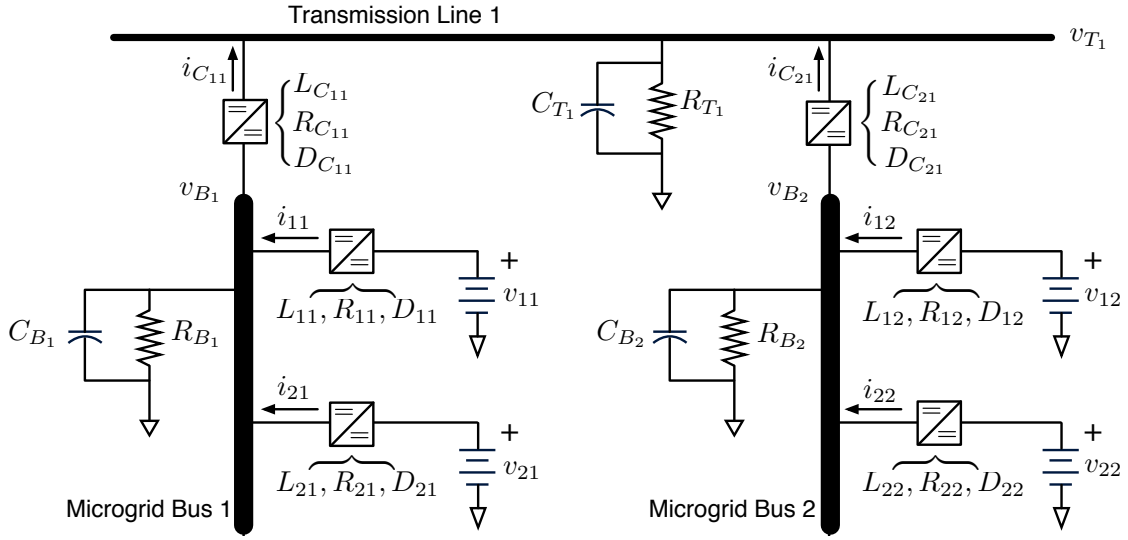


Figure 2.4: A two-microgrid networked configuration with one transmission line.

$$\begin{aligned}
 -R_{11}i_{11}^2 - P_{11} + v_{11}i_{11} &= 0 \\
 -R_{21}i_{21}^2 - P_{21} + v_{21}i_{21} &= 0 \\
 -R_{12}i_{12}^2 - P_{12} + v_{12}i_{12} &= 0 \\
 -R_{22}i_{22}^2 - P_{22} + v_{22}i_{22} &= 0
 \end{aligned} \tag{2.18}$$

$$\begin{aligned}
 -R_{C11}i_{C11}^2 - P_{C11} + v_{B1}i_{C11} &= 0 \\
 -R_{C21}i_{C21}^2 + v_{T1}i_{C21} - P_{C21} &= 0
 \end{aligned} \tag{2.19}$$

$$\phi_{B_1} = P_{11} + P_{21} - P_{B_1} - v_{B_1} i_{C_{11}} = 0 \quad (2.20)$$

$$\phi_{B_2} = P_{12} + P_{22} - P_{B_2} + P_{C_{21}} = 0$$

$$\phi_{T_1} = P_{C_{11}} - v_{T_1} i_{C_{21}} - P_{T_1} = 0 \quad (2.21)$$

with the objective function

$$J = \frac{1}{2} (R_{11} i_{11}^2 + R_{21} i_{21}^2 + R_{12} i_{12}^2 + R_{22} i_{22}^2 + R_{C_{11}} i_{C_{11}}^2 + R_{C_{21}} i_{C_{21}}^2) \quad (2.22)$$

and Hamiltonian

$$\begin{aligned} H = & \frac{1}{2} (R_{11} i_{11}^2 + R_{21} i_{21}^2 + R_{12} i_{12}^2 + R_{22} i_{22}^2 + R_{C_{11}} i_{C_{11}}^2 + R_{C_{21}} i_{C_{21}}^2) \\ & + \lambda_{B_1} (P_{11} + P_{21} - P_{B_1} - v_{B_1} i_{C_{11}}) + \lambda_{B_2} (P_{12} + P_{22} - P_{B_2} + P_{C_{21}}) \\ & + \lambda_{T_1} (P_{C_{11}} - v_{T_1} i_{C_{21}} - P_{T_1}) \end{aligned} \quad (2.23)$$

Applying the necessary conditions of Eq. 2.16 gives

$$\frac{\partial H}{\partial P_{ij}} + \frac{\partial H}{\partial i_{ij}} \frac{\partial i_{ij}}{\partial P_{ij}} = 0 \rightarrow P_{ij}^* \frac{v_{ij}^2}{R_{ij}} \cdot \frac{\lambda_{B_j}^* (\lambda_{B_j}^* - 1)}{(2\lambda_{B_j}^* - 1)^2}, \quad i = 1 \dots \underline{m}_j, \quad j = 1 \dots p \quad (2.24)$$

$$\frac{\partial H}{\partial P_{C_{11}}} + \frac{\partial H}{\partial i_{C_{11}}} \frac{\partial i_{C_{11}}}{\partial P_{C_{11}}} = 0 \rightarrow P_{C_{11}}^* = \frac{v_{B_1}^2}{R_{C_{11}}} \cdot \frac{(\lambda_{B_1}^* - \lambda_{T_1}^*) (1 - \lambda_{B_1}^* - \lambda_{T_1}^*)}{(2\lambda_{T_1}^* - 1)^2} \quad (2.25)$$

$$\frac{\partial H}{\partial P_{C_{21}}} + \frac{\partial H}{\partial i_{C_{21}}} \frac{\partial i_{C_{21}}}{\partial P_{C_{21}}} = 0 \rightarrow P_{C_{21}}^* = \frac{v_{T_1}^2}{R_{C_{21}}} \cdot \frac{(\lambda_{B_2}^* - \lambda_{T_1}^*) (1 - \lambda_{B_2}^* - \lambda_{T_1}^*)}{(2\lambda_{B_2}^* - 1)^2} \quad (2.26)$$

Since the power expressions above must be positive, several constraints on the Lagrange multipliers arise as shown in Eq. 2.27.

$$\begin{aligned} \lambda_{B_j}^* (\lambda_{B_j}^* + 1) &> 0, \quad i = 1 \dots \underline{m}_j, \quad j = 1 \dots p \\ (\lambda_{B_1}^* - \lambda_{T_1}^*) (1 - \lambda_{B_2}^* - \lambda_{T_1}^*) &> 0 \\ (\lambda_{T_1}^* - \lambda_{B_2}^*) (1 - \lambda_{B_2}^* - \lambda_{T_1}^*) &> 0 \end{aligned} \quad (2.27)$$

Substituting the optimal power expressions of Eq. 2.16 gives the optimal currents as a function of the optimal Lagrange multipliers, shown in Eq. 2.28 through 2.30.

$$i_{ij}^* = \frac{v_{ij}}{2R_{ij}} \cdot \left[1 - \left| \frac{1}{2\lambda_{B_j}^* - 1} \right| \right], \quad i = 1 \dots \underline{m}_j, \quad j = 1 \dots p \quad (2.28)$$

$$i_{C_{11}}^* = \frac{v_{B_1}}{2R_{C_{11}}} \cdot \left[1 - \left| \frac{2\lambda_{B_1}^* - 1}{2\lambda_{T_1}^* - 1} \right| \right] \quad (2.29)$$

$$i_{C_{21}}^* = \frac{v_{T_1}}{2R_{C_{21}}} \cdot \left[1 - \left| \frac{2\lambda_{T_1}^* - 1}{2\lambda_{B_2}^* - 1} \right| \right] \quad (2.30)$$

The constraint equations, Eq. 2.20 and Eq. 2.21, can be expressed in terms of three polynomial equations in the three optimal Lagrange multipliers of Eq. 2.31 through 2.33. After solving them for the $\lambda_{T_1}^*$, $\lambda_{B_1}^*$, and $\lambda_{B_2}^*$, their values can be substituted into Eq. 2.28 through 2.30 and Eq. 2.24 through 2.26 to compute reference currents and powers. Finally, the reference duty cycles are found with Eq. 2.10 and Eq. 2.11 to provide the optimal, feedforward required by the networked microgrid control system.

$$\frac{\lambda_{B_1}^* (\lambda_{B_1}^* + 1)}{(2\lambda_{B_1}^* - 1)^2} \sum_{i=1}^2 \frac{v_{i1}^2}{R_{i1}} - \frac{v_{B_1}^2}{2R_{C_{11}}} \left[1 - \left| \frac{2\lambda_{B_1}^* - 1}{2\lambda_{T_1}^* - 1} \right| \right] - P_{B_1} = 0 \quad (2.31)$$

$$\frac{\lambda_{B_2}^* (\lambda_{B_2}^* + 1)}{(2\lambda_{B_2}^* - 1)^2} \sum_{i=1}^2 \frac{v_{i2}^2}{R_{i2}} - \frac{v_{T_1}^2}{R_{C_{21}}} \cdot \frac{(\lambda_{T_1}^* - \lambda_{B_2}^*) (1 - \lambda_{B_2}^* - \lambda_{T_1}^*)}{(2\lambda_{B_2}^* - 1)^2} - P_{B_2} = 0 \quad (2.32)$$

$$\frac{v_{B_1}^2}{R_{C_{11}}} \cdot \frac{(\lambda_{B_1}^* - \lambda_{T_1}^*) (1 - \lambda_{B_2}^* - \lambda_{T_1}^*)}{(2\lambda_{T_1}^* - 1)^2} - \frac{v_{T_1}^2}{2R_{C_{21}}} \cdot \left[1 - \left| \frac{2\lambda_{T_1}^* - 1}{2\lambda_{B_2}^* - 1} \right| \right] - P_{T_1} = 0 \quad (2.33)$$

The two microgrid example solution above can be generalized to the set of $p + q$ nonlinear equations of Eq. 2.34 and 2.35. Once the optimal Lagrange multipliers are found numerically, Eq. 2.36 and 2.37 are used to solve for the optimal reference currents i_{ij}^* and connection reference currents $i_{C_{jk}}^*$. Eq. 2.6 and Eq. 2.7 are used to find the converter powers, P_{ij} and $P_{C_{jk}}$ leading to the reference duty cycles using Eq. 2.10 and Eq. 2.11.

$$\phi_{B_j} = \frac{\lambda_{B_j} (\lambda_{B_j} - 1)}{(2\lambda_{B_j} - 1)^2} \sum_{i=1}^{\underline{m}_j} \frac{v_{ij}^2}{R_{ij}} - \frac{1}{2} v_{B_j}^2 \sum_{k=1}^q \frac{\left(1 - \left| \frac{2\lambda_{B_j} - 1}{2\lambda_{T_k} - 1} \right| \right)}{R_{c_{jk}}} - P_{B_j} = 0, \quad (2.34)$$

$$j = 1 \dots p$$

$$\phi_{T_k} = \frac{1}{(2\lambda_{T_k} - 1)^2} \cdot \sum_{j=1}^p \frac{v_{B_j}^2 (\lambda_{B_j} - \lambda_{T_k}) (1 - \lambda_{B_j} - \lambda_{T_k})}{R_{C_{jk}}} - P_{T_k} = 0, \quad (2.35)$$

$$k = 1 \dots q$$

$$i_{ij}^* = \frac{v_{ij}}{2R_{ij}} \cdot \left[1 - \left| \frac{1}{2\lambda_{B_j}^* - 1} \right| \right], \quad i = 1 \dots \underline{m}_j, \quad j = 1 \dots p \quad (2.36)$$

$$i_{C_{jk}}^* = \frac{v_{T_k}}{2R_{C_{ij}}} \cdot \left[1 - \left| \frac{2\lambda_{T_k}^* - 1}{2\lambda_{B_j}^* - 1} \right| \right], \quad j = 1 \dots p, \quad k = 1 \dots q \quad \forall E_{jk} \neq 0 \quad (2.37)$$

2.2.2.6 Interconnection Currents Example

For this approach, which also utilizes Eq. 2.18 through Eq. 2.21, where $p = 2$ and $q = 1$, $i_{C_{11}}$ is the free variable to be determined through the optimization process under the constraint that $i_{C_{11}} \geq 0$. For any value of $i_{C_{11}}$, the first expression in Eq. 2.19 can be used to find $P_{C_{11}}$. Equation 2.21 leads to the $i_{C_{21}}$ of Eq. 2.38.

$$i_{C_{21}} = \frac{P_{C_{11}} - P_{T_1}}{v_{T_1}} \quad (2.38)$$

where another constraint is introduced, $P_{C_{11}} \geq P_{T_1}$. The second expression in Eq. 2.19 leads to a unique $i_{C_{21}}$ and another constraint that $P_{C_{21}} \geq 0$. Now that the power flows into and out of all the busses are known, the optimal power settings for all the distributed assets are given by Eq. 2.39 and 2.40 as described in Ref. [38].

$$P_{j1} = \frac{v_{j1}^2}{R_{j1}} \cdot \frac{P_{B_1} + v_{B_1} i_{C_{11}}}{\sum_{k=1}^2 \frac{v_{k1}^2}{R_{k1}}}, \quad j = 1, 2 \quad (2.39)$$

$$P_{j2} = \frac{v_{j2}^2}{R_{j2}} \cdot \frac{P_{B2} - P_{C21}}{\sum_{k=1}^2 \frac{v_{k2}^2}{R_{k2}}}, \quad j = 1, 2 \quad (2.40)$$

yielding another constraint that $P_{B2} \geq P_{C21}$. Finally, the corresponding currents for the distributed assets are computed using Eq. 2.18. Now that all the currents are known, the objective function Eq. 2.22 can be evaluated by the numerical optimization solver. In the next section, each of these algorithms were generalized to any number of microgrids, transmission lines, converter connections within a microgrid and topology (p , q , \underline{m}_j , and E) and then timed to compare their performance.

2.3 Results and Discussion

To quantify and compare the time-to-solution performance of the optimal reference command generators of Section 2.2 for increasing microgrid complexity two test cases were constructed. Both cases used a networked microgrid architecture with $q = 2$ transmission lines where in the first case the number of microgrids was fixed but the number of assets in each microgrid was increased. In the second case the number of assets in each microgrid was fixed but the number of microgrids was increased. The increasing assets case used $p = 4$ microgrids where each microgrid was connected to

both transmission lines as indicated by E_1 of Eq. 2.41. The number of generation assets on each microgrid was varied from $n = 1$ to $n = 100,000$ indicated by \underline{m}_1 of Eq. 2.41. In the increasing microgrids case the number of microgrids was varied from $h = 1$ to $h = 250$, shown in Eq. 2.42, where all of them were connected to both transmission lines and had five assets also shown in Eq. 2.41. The model parameters are listed in Table 2.1 along with the initial conditions for the numerical solvers.

Time trials were performed on a desktop computer equipped with an Intel i7-3770 3.4 GHz processor, 16 GB of memory, 240 GB SSD, 64 bit Windows 7 and MATLAB 2013a. Different MATLAB solvers were used depending on the reference generator. The All Currents and Duty Cycles (Section 2.2.2.1) and the Interconnection Currents and Duty Cycles (Section 2.2.2.2) approaches were solved with `fmincon`, the Interconnection Currents (Section 2.2.2.4) was solved with `fminunc`, and the Lagrange Multipliers method was solved with (Section 2.2.2.3) with `lsqnonlin`. Penalty terms were added to the objective function to help enforce current the duty cycle constraints of Table 2.1.

Table 2.1
Timing Comparison Model Setup

Variable	Value	Unit
R_{ij}, R_{Cjk}	0.5	Ω
R_{Bj}	100	Ω
R_{Lj}	0.0	Ω
R_{Tk}	50	Ω
v_{ij}	220	V
v_{Bj}	480	V
v_{Tk}	1000	V
$\min(D_{ij}), \min(D_{Cjk})$	0.1	%
$\max(D_{ij}), \max(D_{Cjk})$	99.9	%
$\min(i_{ij}), \min(i_{Cjk})$	-1000	A
$\max(i_{ij}), \max(i_{Cjk})$	1000	A
D_{ij} i.c.	42.0	%
D_{Cjk} initial condition	46.0	%
i_{ij} initial condition	10.0	A
i_{Cjk} initial condition	5.0	A

$$E_1 = \begin{bmatrix} 1 & 1 \\ 1 & 1 \\ 1 & 1 \\ 1 & 1 \end{bmatrix}, \underline{m}_1 = \begin{bmatrix} 1 & \cdots & n \\ 1 & \cdots & n \\ 1 & \cdots & n \\ 1 & \cdots & n \end{bmatrix} \quad (2.41)$$

$$E_2 = \begin{bmatrix} 1 & 1 \\ \vdots & \vdots \\ h & h \end{bmatrix}, \underline{m}_2 = \begin{bmatrix} 5 \\ \vdots \\ 5 \end{bmatrix} \quad (2.42)$$

2.3.1 Increasing Number of Assets Case

The timing results are shown in Figure 2.5. As expected, the All Currents and Duty Cycles approach (Section 2.2.2.1) solution time increased far faster than the three other approaches with the longest tested solution time of 106.8 s at 512 boost converters. For this same quantity of 512 boost converters, the Interconnection Currents and Duty Cycles (Section 2.2.2.2) solved in 0.017 s, the Interconnection Currents (Section 2.2.2.4), in 0.011 s and the fastest, the Lagrange Multiplier approach (Section 2.2.2.3), solved in 0.009 s. The All Currents and Duty Cycles solution was not run for more than 512 converters due to its long solution times.

The solution times remained relatively constant for the three more efficient methods, with some numerical “noise,” for less than 500 boost converters. Beyond 10,000 converters, the computational workload increased exponentially. For the largest sized

grid using over 130,000 converters the fastest solution was still the Lagrange Multiplier approach at 0.056 s. While a network of this size may have been theoretical in nature it allowed exploring the limitations of the algorithms developed and to quantify when sub second solutions were no longer possible. The Interconnection Currents and Duty Cycles and Interconnection Currents approaches were slower by over an order of magnitude at 0.909 s and 0.751 s respectively. At large numbers of boost converters, the Interconnection Currents and Duty Cycles and Interconnection Currents solution times increase at the same rates but with an offset, which is attributed to the reduced number of free variables in the Interconnection Currents approach.

A measure of solution error was computed by substituting the optimal solution into the steady state power flow equations, Eq. 2.6 through Eq. 2.9, and forming the L_2 norm of the non-zero errors. This was repeated for 100 unique solution runs where the maximum was always less than 10^{-5} , indicating valid solutions were found.

2.3.2 Increasing Number of Microgrids Case

This case posed a more numerically challenging problem for all the algorithms since the number of free variables increased with microgrid quantity as shown in Figure 2.6. At 250 microgrids, the performance trend was similar to that found in Section 2.3.1, but with reduced disparity between each method's solution time. The All Currents

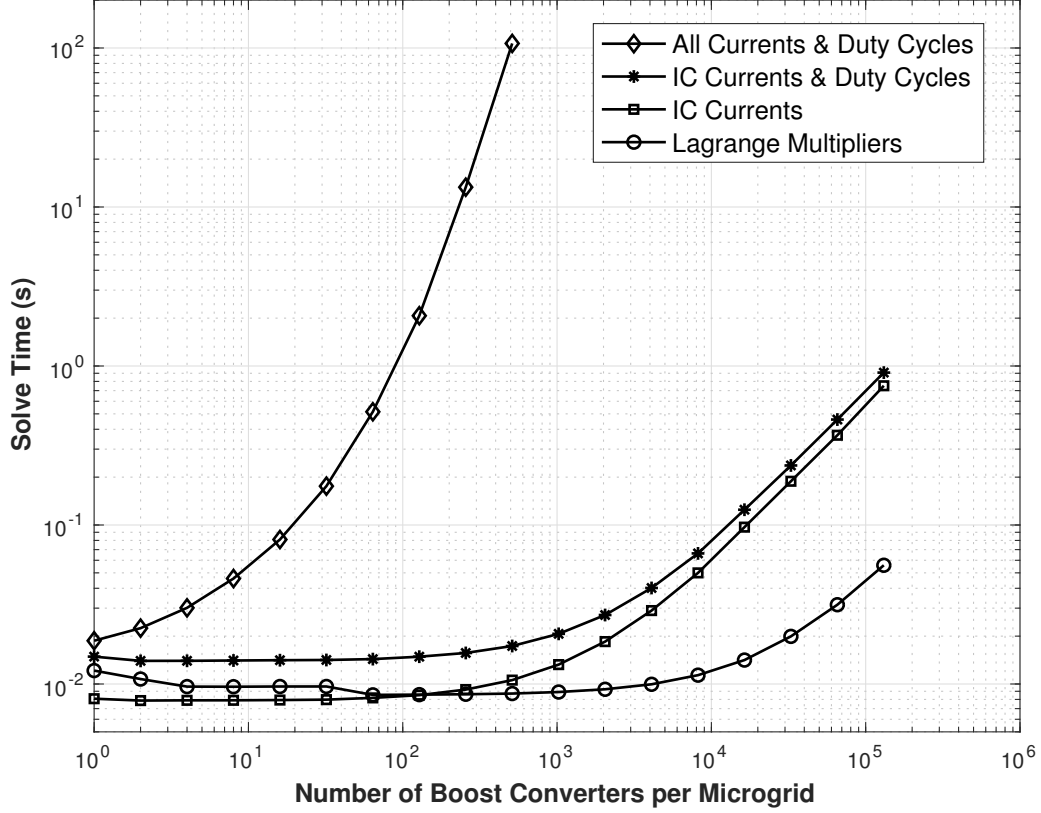


Figure 2.5: Time-to-solution comparison of reference command generators for the increasing number of assets case. Interconnection is abbreviated as IC.

and Duty Cycles approach solved 250 microgrids in 110.9 s while the Lagrange Multiplier method reduced this time to 0.237 s or approximately 470 times faster. The other two methods fall between these two times above eight microgrids. For single microgrids, the Interconnection Currents and Duty Cycles showed a 1.5 improvement factor over the All Currents and Duty Cycles approach. At eighty microgrids, a solution time cross over occurred between the Lagrange Multiplier and the Interconnection Currents approaches and is attributed to the fewer free variables in the Interconnection Currents approach below this number of microgrids. The residual error measurement remained below 10×10^{-9} for all the solutions obtained.

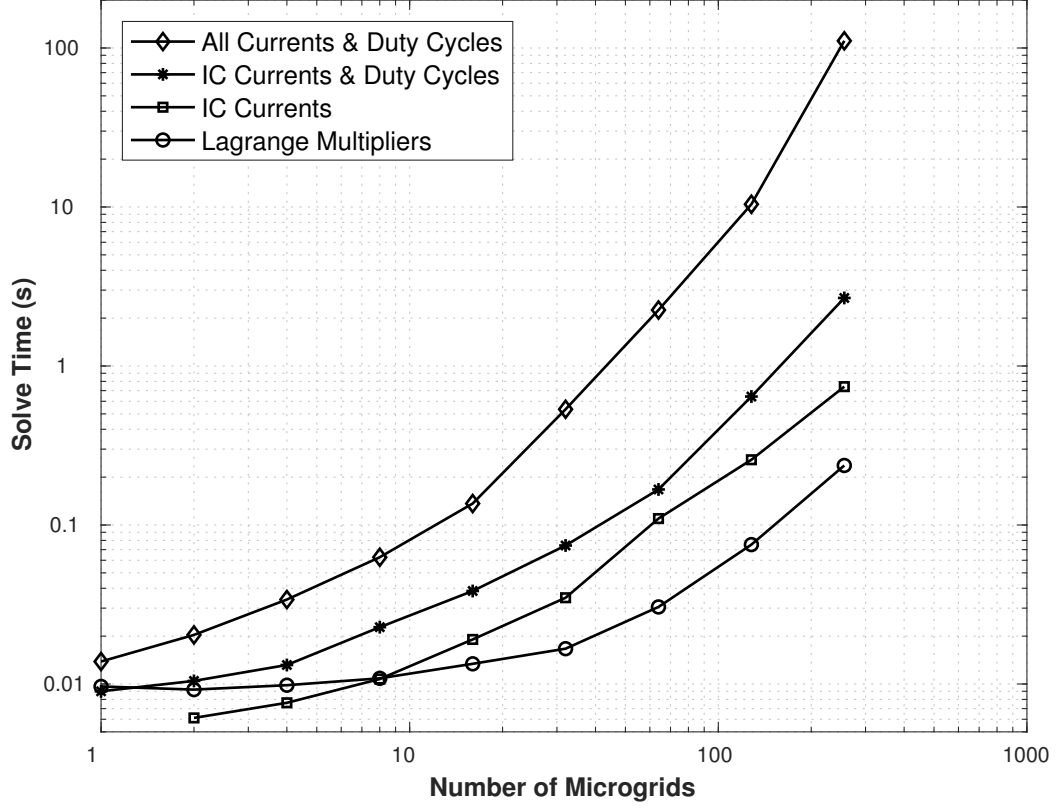


Figure 2.6: Time-to-solution comparison of reference command generators for the increasing number of microgrids case. Interconnection is abbreviated as IC.

2.4 Conclusions

Of the four optimal reference command generators shown in this paper, the Lagrange Multiplier approach achieved the fastest solution time at large problem sizes. This leads to the main conclusion that optimal duty cycle and reference commands can be generated for relatively large networked microgrids at the sub-second level. For the particular two transmission line configurations considered here the Lagrange Multiplier method should be used for more than 1,000 converters in a single microgrid

and more than 20 microgrids in a networked configuration. Below those values, any of the methods, except the All Currents and Duty Cycles method, could be used to achieve sub-second solutions. It should be noted that this was made possible by exploiting the closed form power loss optimal solution at the microgrid level. Without this combination of closed form plus numerical solution, it is very difficult to achieve fast solutions. This is consistent with the numerical solutions obtained for a multi-objective function with solution times of 25 s to 58 s [25].

While the Lagrange Multiplier approach appears most attractive, it does have some drawbacks. First, if a solution to the $p + q$ equations does not exist, then all that is known is that the configuration will not permit satisfaction of the specified loads while minimizing the power losses. It misses possible solutions where microgrids should be disconnected from the transmission line. For example, if flowing power from microgrid one to satisfy microgrid two's loads generates more lost power than simply isolating microgrid two from the transmission line, then Equations 2.31 through 2.33 will not produce a solution. No additional information is provided and a feasible power apportionment strategy will not be available. Second, the Lagrange multipliers physical interpretation does not provide useful information for the task at hand - generating reference duty cycle and current commands. The Lagrange multipliers describe the sensitivity of the total lost power, J , to changes in the required loads. For example, $\lambda_{B_1} = \partial J / \partial P_{B_1}$. Since the required loads are non-negotiable, there is little value in this information. However, load shedding strategies could exploit this

information and this is a possible area of further study.

For more physically founded solutions, the Interconnection Currents and Duty Cycles and Interconnection Currents approaches out performed the All Currents and Duty Cycles approach regardless of problem size and type. The Interconnection Currents had the drawback of requiring at least two transmission lines and this does limit its usefulness. For example, a zero interconnection current implies decoupling of a microgrid from the network. This is the recommended solution as long as the solution time is acceptable. For a specified set of possible topologies and assets, the simulation approach developed above can be easily used to determine a nominal solution time and thus guide the choice of the reference command generator. A drawback to the numerically efficient approaches that were developed is a dependence on the objective function selected, which allowed for a reduction in numerical work load. If a different multi-objective cost function is desired, then the All Currents and Duty Cycles approach must be used with the penalty of increased solution time.

Chapter 3

Exergy Optimal Multi-Physics

Aircraft Microgrid Control

Architecture¹

In this chapter, the HSSPFC is developed generally for networked microgrids which will work together with the optimization techniques developed in Chapter 2. The generalized networked microgrid architecture, from Chapter 2, was expanded in two ways. First, provisions for allowing microgrid buses to be sourced from higher voltage sources through buck converters were added. Secondly, buck/boost power converters were added for interconnecting microgrids at similar voltage levels enabling controlled

¹The material contained in this chapter has been submitted to *International Journal of Electrical Power & Energy Systems*.

flow power flow. A three bus networked microgrid system was developed where two buses have installed generation and connected via power converters. This allowed coordinated power flow between microgrids while optimizing exergy destruction. A pulsed device was the dominant system load. A thermal dynamic model was developed to capture the cooling demands imposed by both the power electronic devices and pulsed load. This produced coupling between the thermal and electrical systems. The model was explored in non-realtime using average mode power converters to provide proof of concept that the HSSPFC and the optimizations from Chapter 2 can work together. This example model is expanded to run in real-time on HIL simulators in Chapter 4.

3.1 Networked DC Microgrids with Similar Bus Voltages

A flexible set of networked microgrid circuit equations were originally developed by Wilson et al. [37] and further studied and improved by Trinklein et al. [43]. There are several improvements to the equations from [43] that have been addressed in this work. First, the microgrid sources and storage voltages can be above or below the transmission line voltages by adopting both buck and boost converter topologies as shown in Figure 3.1 and 3.2 respectively. In the boost and buck figures, only

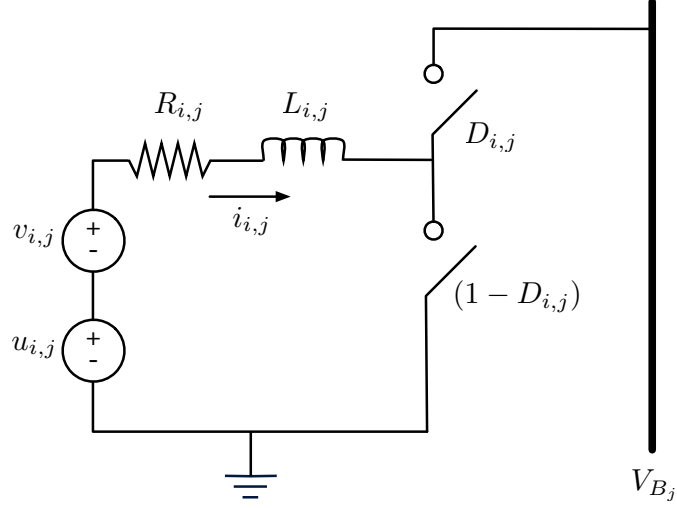


Figure 3.1: Microgrid Source Connected Through Boost to Voltage Bus, $v_{i,j} + u_{i,j} < V_{B_j}$

the power converter components are shown; loads and interconnections have been omitted. Secondly, the interconnection power converters were simplified by replacing the directionally selectable boost converters with a buck/boost architecture [44] and shown in Figure 3.3. The buck/boost converter allows power flow where similar voltages are present on both the microgrid voltage bus and the transmission line bus without reconfiguring the converter topology while online. If substantial voltages differences will exist between the microgrid and transmission line, then we recommend maintaining the boost converter architecture as originally presented in [37]. Thirdly, commas have been added to the notation defining the indexing between microgrids. This improves readability when numerical values are substituted for index values in large systems. The updated circuit equations are given as Eq. 3.1 through 3.4 and the indexing nomenclature is given below. Fourth, coupling to other multi-physical systems has been added by providing external current loads on the microgrid buses.

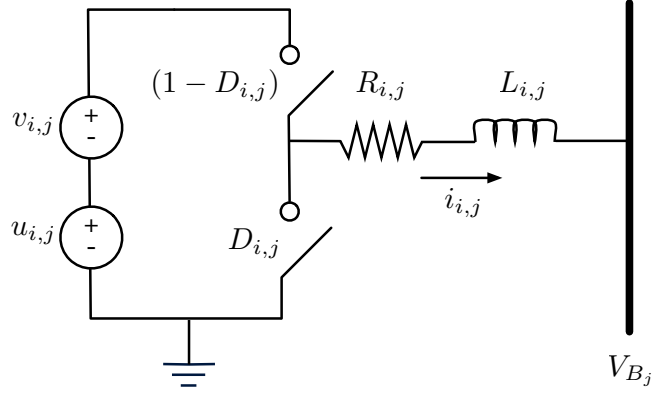


Figure 3.2: Microgrid Source Connected Through Buck Converter to Voltage Bus, $v_{i,j} + u_{i,j} > V_{B_j}$

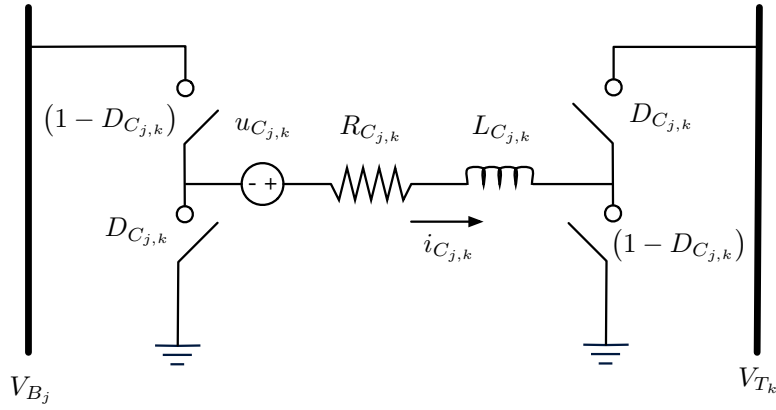


Figure 3.3: buck/Boost Power Converter Architecture with Integral Storage.

Let

i = i^{th} source converter,

j = j^{th} bus,

k = k^{th} transmission line,

p = total number of microgrids,

q = total number of transmission lines,

$E_{j,k} = p \times q$ connectivity matrix,

m_j = number of source converters on j^{th} bus,

$b_{i,j} = \max(m_j) \times p$ source converter type matrix,

m_{L_j} = additional resistive loads on j^{th} bus,

i_{L_j} = external current loads on j^{th} bus,

and governing dynamic equations be

[illegible]

$$L_{C_{j,k}} \frac{di_{C_{j,k}}}{dt} = -R_{C_{j,k}} i_{C_{j,k}} + (1 - D_{C_{j,k}}) v_{B_j} - D_{C_{j,k}} v_{T_k} + u_{C_{j,k}}, \quad (3.2)$$

$$j = 1 \dots p, \quad k = 1 \dots q, \quad \forall E_{jk} \neq 0$$

$$(3.3)$$

$$(3.4)$$

3.2 Hamiltonian Feed Forward and Feed Back Formulation

The Hamiltonian control formulation begins by placing the Eqs. 3.1 through 3.4 into state space form:

$$\mathbf{M}\dot{\mathbf{x}} = \mathbf{R}\mathbf{x} + \mathbf{D}^T\mathbf{v} + \mathbf{B}^T\mathbf{u} = [\bar{\mathbf{R}} + \tilde{\mathbf{R}}]\mathbf{x} + \mathbf{D}^T\mathbf{v} + \mathbf{B}^T\mathbf{u} \quad (3.5)$$

where

$$\mathbf{x} = \begin{bmatrix} i_{1,1} \\ \vdots \\ i_{m,p} \\ i_{C1,1} \\ \vdots \\ i_{Cp,q} \\ v_{B1} \\ \vdots \\ v_{Bp} \\ v_{T1} \\ \vdots \\ v_{Tq} \end{bmatrix}, \quad \mathbf{v} = \begin{bmatrix} v_{1,1} \\ \vdots \\ v_{m,p} \\ 0 \\ \vdots \\ 0 \\ 0 \\ \vdots \\ 0 \\ 0 \\ \vdots \\ 0 \end{bmatrix}, \quad \text{and} \quad \mathbf{u} = \begin{bmatrix} u_{1,1} \\ \vdots \\ u_{m,p} \\ u_{C1,1} \\ \vdots \\ u_{Cp,q} \\ u_{B1} \\ \vdots \\ u_{Bp} \\ u_{T1} \\ \vdots \\ u_{Tq} \end{bmatrix}.$$

\mathbf{R} can be decomposed into a diagonal matrix, $\bar{\mathbf{R}}$, and skew-symmetric matrix, $\tilde{\mathbf{R}}$.

The matrices \mathbf{M} , $\bar{\mathbf{R}}$, $\tilde{\mathbf{R}}$, \mathbf{D}^T , and \mathbf{B}^T can be found in Appendix B, where microgrid sources can have either buck or boost architectures.

The system error state and control inputs are defined as

$$\begin{aligned}\tilde{\mathbf{x}} &= \mathbf{e} = \mathbf{x}_R - \mathbf{x}, \\ \tilde{\mathbf{u}} &= \Delta \mathbf{u} = \mathbf{u}_R - \mathbf{u},\end{aligned}\tag{3.6}$$

where the reference state and control vectors are

$$\mathbf{M}\dot{\mathbf{x}}_R = \mathbf{R}\mathbf{x}_R + \mathbf{D}^T \mathbf{v} + \mathbf{B}^T \mathbf{u}_R.\tag{3.7}$$

The feedback control law is developed using an exergy formulation. The Hamiltonian of the system is stored exergy,

$$\mathbf{H} = \frac{1}{2}\tilde{\mathbf{x}}^T \mathbf{M}\tilde{\mathbf{x}} + \frac{1}{2}\left(\int_0^t \tilde{\mathbf{x}} d\tau\right)^T \mathbf{B}^T \mathbf{K_I} \mathbf{B} \left(\int_0^t \tilde{\mathbf{x}} d\tau\right),\tag{3.8}$$

where $\mathbf{K_I}$ is a positive definite integral controller gain. Noting that \mathbf{M} is positive

definite, the static stability conditions are met [36]. The first time derivative of the Hamiltonian is

$$\dot{\mathbf{H}} = \tilde{\mathbf{x}}^T \mathbf{M} \dot{\tilde{\mathbf{x}}} + \tilde{\mathbf{x}}^T \mathbf{B}^T \mathbf{K}_I \mathbf{B} \left(\int_0^t \tilde{\mathbf{x}} d\tau \right), \quad (3.9)$$

where $\dot{\mathbf{H}} < 0$ must be met for dynamic stability. This will be accomplished through the proper definition of the feedback control law. Noting that integral feedback is an exergy generator and proportional feedback provides exergy storage, a proportional-integral (PI) feedback controller is selected

$$\Delta \mathbf{u} = -\mathbf{K}_P \mathbf{B} \tilde{\mathbf{x}} - \mathbf{K}_I \mathbf{B} \int_0^t \tilde{\mathbf{x}} d\tau, \quad (3.10)$$

where \mathbf{K}_P is a positive definite proportional controller gain. Substituting (3.5) and (3.6) into (3.9) and simplifying yields,

$$\begin{aligned}
\dot{\mathbf{H}} &= \tilde{\mathbf{x}}^T [\mathbf{M} (\dot{\mathbf{x}}_{\mathbf{R}} - \dot{\mathbf{x}})] + \tilde{\mathbf{x}}^T \mathbf{B}^T \mathbf{K}_{\mathbf{I}} \mathbf{B} \left(\int_0^t \tilde{\mathbf{x}} d\tau \right), \\
&= \tilde{\mathbf{x}}^T [\mathbf{R} \tilde{\mathbf{x}} + \mathbf{B}^T \Delta \mathbf{u}] + \tilde{\mathbf{x}}^T \mathbf{B}^T \mathbf{K}_{\mathbf{I}} \mathbf{B} \left(\int_0^t \tilde{\mathbf{x}} d\tau \right).
\end{aligned} \tag{3.11}$$

Substituting (3.10) into (3.11) eliminates the integral term and simplifies to

$$\dot{\mathbf{H}} = \tilde{\mathbf{x}}^T \mathbf{R} \tilde{\mathbf{x}} - \tilde{\mathbf{x}}^T \mathbf{B}^T \mathbf{K}_{\mathbf{P}} \mathbf{B} \tilde{\mathbf{x}}. \tag{3.12}$$

The dynamic stability requirement $\dot{\mathbf{H}} < 0$ provides the stability constraint condition on the selection of $\mathbf{K}_{\mathbf{P}}$. Taking advantage of $\tilde{\mathbf{x}}^T \tilde{\mathbf{R}} \tilde{\mathbf{x}} = 0$ yields,

$$\dot{\mathbf{H}} = -\tilde{\mathbf{x}}^T [\mathbf{B}^T \mathbf{K}_{\mathbf{P}} \mathbf{B} - \bar{\mathbf{R}}] \tilde{\mathbf{x}} < 0 \quad \forall \tilde{\mathbf{x}} \neq 0. \tag{3.13}$$

For feedback control dynamic stability, combine (3.6), (3.7), and (3.10) to arrive at

$$\mathbf{u} = \mathbf{u}_R - \Delta \mathbf{u} = [\mathbf{B}^T]^{-1} [\mathbf{M}\dot{\mathbf{x}}_R - \mathbf{R}\mathbf{x}_R - \mathbf{D}^T \mathbf{v}] + \mathbf{K}_P \mathbf{B} \tilde{\mathbf{x}} + \mathbf{K}_I \mathbf{B} \int_0^t \tilde{\mathbf{x}} d\tau. \quad (3.14)$$

Substituting (3.14) into (3.5) and simplifying yields

$$\dot{\tilde{\mathbf{x}}} = \mathbf{M}^{-1} \left[(\mathbf{R} - \mathbf{B}^T \mathbf{K}_P \mathbf{B}) \tilde{\mathbf{x}} - \mathbf{B}^T \mathbf{K}_I \mathbf{B} \int_0^t \tilde{\mathbf{x}} d\tau \right]. \quad (3.15)$$

The second time derivative of the Hamiltonian is,

$$\ddot{\mathbf{H}} = -2\tilde{\mathbf{x}}^T [\mathbf{B}^T \mathbf{K}_P \mathbf{B} - \bar{\mathbf{R}}] \dot{\tilde{\mathbf{x}}} \quad (3.16)$$

Substituting (3.15) into (3.16) provides

$$\begin{aligned} \ddot{\mathbf{H}} &= -2\tilde{\mathbf{x}}^T [\mathbf{B}^T \mathbf{K}_P \mathbf{B} - \bar{\mathbf{R}}] \mathbf{M}^{-1} \left[(\mathbf{R} - \mathbf{B}^T \mathbf{K}_P \mathbf{B}) \tilde{\mathbf{x}} - \mathbf{B}^T \mathbf{K}_I \mathbf{B} \int_0^t \tilde{\mathbf{x}} d\tau \right] \\ &= 0 \quad \forall \tilde{\mathbf{x}} = 0. \end{aligned} \quad (3.17)$$

Substituting (3.15) into the third time derivative of the Hamiltonian and simplifying

returns

$$\ddot{\mathbf{H}} = -2 \left[\mathbf{M}^{-1} \mathbf{B}^T \mathbf{K}_I \mathbf{B} \int_0^t \tilde{\mathbf{x}} d\tau \right]^T [\mathbf{B}^T \mathbf{K}_P \mathbf{B} - \bar{\mathbf{R}}] \left[\mathbf{M}^{-1} \mathbf{B}^T \mathbf{K}_I \mathbf{B} \int_0^t \tilde{\mathbf{x}} d\tau \right] < 0, \quad (3.18)$$

and

$$\ddot{\mathbf{H}} = 0 \quad \forall \int_0^t \tilde{\mathbf{x}} d\tau = 0. \quad (3.19)$$

Since three is an odd number, the dynamical system is asymptotically stable via Schaub and Junkins [45].

3.3 Aircraft Microgrid Model

A electro-thermal multi-physics model of a fighter aircraft was developed with a block diagram of the system components given in Figure 3.4.

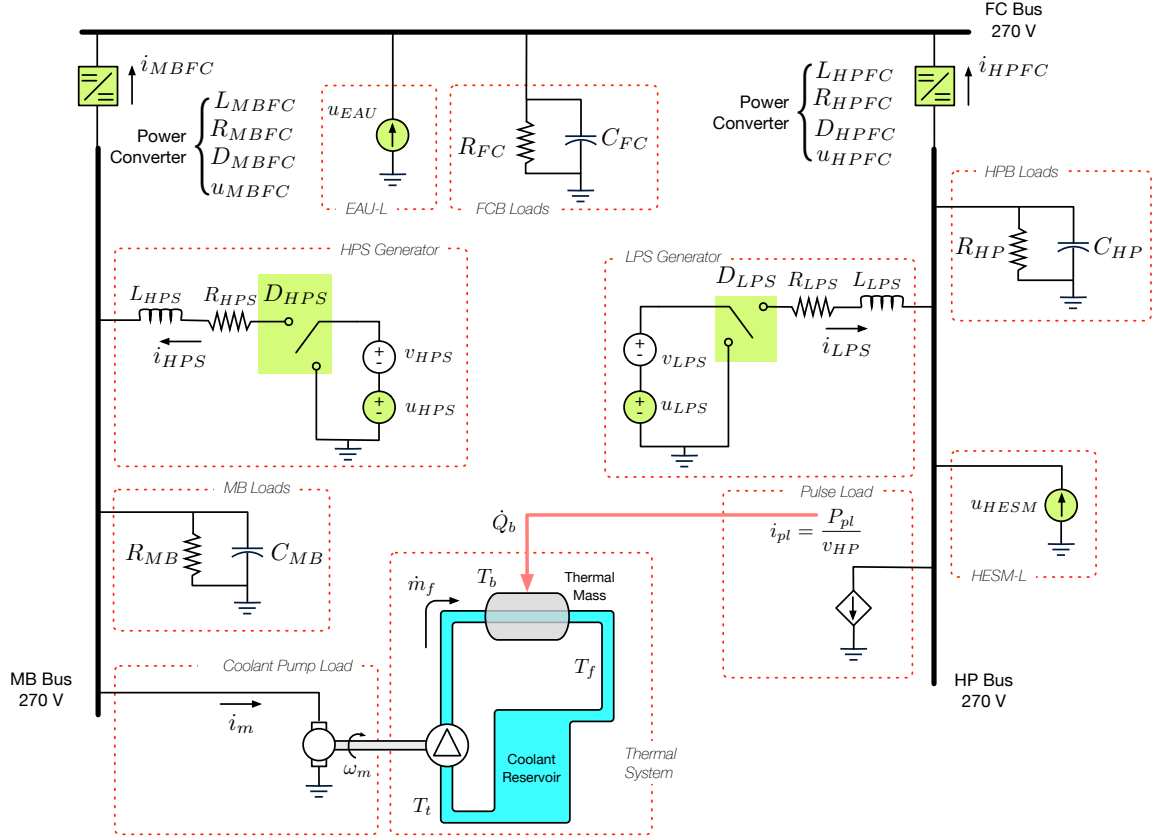


Figure 3.4: Aircraft Electrical Distribution System Modeled as Two Networked Microgrids.

3.3.1 Electrical System

The example system was developed first in generalized form and then translated into a more realistic format. In the example, let the indices be $p = 2$, $q = 1$, $m = [1 \ 1]^T$, $m_L = [0 \ 0]^T$, and $E_{j,k} = [1 \ 1]^T$ with the both microgrid sources as buck converters and no storage on microgrid 1, yields Eq. 3.20 through 3.23. Potential storage elements u_{HPS} , u_{LPS} , u_{MBFC} , and u_{HPFC} from Figure 3.4 were set to zero while u_{EAU} , u_{HESM} were implemented.

$$\begin{aligned}
L_{1,1} \frac{di_{1,1}}{dt} &= -R_{1,1}i_{1,1} - v_{B_1} + D_{1,1}(v_{1,1} + u_{1,1}) \\
L_{1,2} \frac{di_{1,2}}{dt} &= -R_{1,2}i_{1,2} - v_{B_2} + D_{1,2}(v_{1,2} + u_{1,2})
\end{aligned} \tag{3.20}$$

$$\begin{aligned}
L_{C_{1,1}} \frac{di_{C_{1,1}}}{dt} &= -R_{C_{1,1}}i_{C_{1,1}} + (1 - D_{C_{1,1}})v_{B_1} - D_{C_{1,1}}v_{T_1} + u_{C_{1,1}} \\
L_{C_{2,1}} \frac{di_{C_{2,1}}}{dt} &= -R_{C_{2,1}}i_{C_{2,1}} + (1 - D_{C_{2,1}})v_{B_2} - D_{C_{2,1}}v_{T_1} + u_{C_{2,1}}
\end{aligned} \tag{3.21}$$

$$\begin{aligned}
C_{B_1} \frac{dv_{B_1}}{dt} &= (1 - D_{C_{1,1}})i_{C_{1,1}} - \frac{v_{B_1}}{R_{B_1}} - i_{L_1} \\
C_{B_2} \frac{dv_{B_2}}{dt} &= (1 - D_{C_{2,1}})i_{C_{2,1}} - \frac{v_{B_2}}{R_{B_2}} - i_{L_2} + u_{B_2}
\end{aligned} \tag{3.22}$$

$$C_{T_1} \frac{dv_{T_1}}{dt} = D_{C_{1,1}}i_{C_{1,1}} + D_{C_{2,1}}i_{C_{2,1}} - \frac{v_{T_1}}{R_{T_1}} + u_{T_1} \tag{3.23}$$

Now application specific notation for the electrical system will be mapped to the generalized equations. The purpose is to show how a realistic system can be represented using the generalized form by modifying the notation from that given in Eq. 3.20 through 3.23 to the model specific notation of Eq. 3.24 through 3.27 and shown in Figure 3.4.

$$\begin{aligned}
L_{HPS} \frac{di_{HPS}}{dt} &= -R_{HPS} i_{HPS} - v_{MB} + D_{HPS} (v_{HPS} + u_{HPS}) \\
L_{LPS} \frac{di_{LPS}}{dt} &= -R_{LPS} i_{LPS} - v_{HP} + D_{LPS} (v_{LPS} + u_{LPS})
\end{aligned} \tag{3.24}$$

$$\begin{aligned}
L_{MBFC} \frac{di_{MBFC}}{dt} &= -R_{MBFC} i_{MBFC} + (1 - D_{MBFC}) v_{MB} - D_{MBFC} v_{FC} + u_{MBFC} \\
L_{HPFC} \frac{di_{HPFC}}{dt} &= -R_{HPFC} i_{HPFC} + (1 - D_{HPFC}) v_{HP} - D_{HPFC} v_{FC} + u_{HPFC}
\end{aligned} \tag{3.25}$$

$$\begin{aligned}
C_{MB} \frac{dv_{MB}}{dt} &= (1 - D_{MBFC}) i_{MBFC} - \frac{v_{MB}}{R_{MB}} - i_m \\
C_{HP} \frac{dv_{HP}}{dt} &= (1 - D_{HPFC}) i_{HPFC} - \frac{v_{HP}}{R_{HP}} - i_{pl} + u_{HESM}
\end{aligned} \tag{3.26}$$

$$C_{FC} \frac{dv_{FC}}{dt} = D_{MBFC} i_{MBFC} + D_{HPFC} i_{HPFC} - \frac{v_{FC}}{R_{FC}} + u_{EAU} \tag{3.27}$$

3.3.2 Pulsed Load and Thermal System

The aircraft model's thermal and pulsed load system was adopted from the ship cooling system presented in Trinklein et al. [46] and simplified where applicable. A

Table 3.1
Aircraft Model Electrical Setup

Variable	Value	Unit
R_{HPS}, R_{LPS}	0.5	Ω
R_{MB}, R_{HP}	100	Ω
R_{FC}	50	Ω
R_{MBFC}, R_{HPFC}	0.5	Ω
L_{HPS}, L_{LPS} L_{MBFC}, L_{HPFC}	0.002	H
C_{MB}, C_{HP}, C_{FC}	0.1	F
v_{HPS}, v_{LPS}	480	V
v_{HP}, v_{MB}, v_{FC}	270	V
$\min(D_{HPS}, D_{LPS},$ $D_{MBFC}, D_{HPFC})$	0.1	%
$\max(D_{HPS}, D_{LPS},$ $D_{MBFC}, D_{HPFC})$	9.99	%
$\min(i_{HPS}, i_{LPS})$	0	A
$\min(i_{MBFC}, i_{HPFC})$	-1000	
$\max(i_{HPS}, i_{LPS},$ $i_{MBFC}, i_{HPFC})$	1000	A

list of system parameters associated with the thermal model are given in Table 3.2. A single fixed displacement pump circulates coolant fluid through the pulsed load coolant passages and coolant tank. A single lumped parameter K_{pump} relates the pump's rotation speed, ω_m , to its current draw, i_m , based on the bus voltage, v_{MB} in Eq. 3.28. The pump is modeled as a closed loop speed system with resulting first order dynamics captured in Eq. 3.29 where τ_{pump} is the time constant, $\omega_{m,cmd}$ is the commanded pump speed, and ω_m is the resulting output speed. The pump mass flow rate, \dot{m}_f , is related to ω_m through Eq. 3.30, where the cooling fluid is assumed to be kerosene of density ρ_f and D_{pump} is the pump's displacement.

Table 3.2
Aircraft Model Thermal System Parameters

Variable	Value	Unit
D_{pump}	7.57E-4	m ³ /rev
K_{pump}	0.2	N·s·m
K_{heat}	0.8	W/W
R_m	3.0	Ω
ρ_f	810	kg/m ³
τ_{pump}	0.1	s
c_{pf}	2.0	kJ/(kg·K)
c_{pb}	0.38	kJ/(kg·K)
C_t	6132	kJ/K
C_{fb}	20	kJ/K
C_b	10	kJ/K
r_f	0.01	K/W
r_b	0.1	K/W

$$v_{MB} i_m = K_{pump} \omega_m^2 \quad (3.28)$$

$$\frac{\omega_m}{\omega_{m,cmd}} = \frac{1}{\tau_{pump} s + 1} \quad (3.29)$$

$$\dot{m}_f = \frac{\omega_m \rho_f D_{pump}}{2\pi} \quad (3.30)$$

3.3.2.1 Lumped Thermal Model

The pulsed load is applied to the electrical system through a current source to ground, i_{pl} , as shown in Figure 3.4 and in Eq. 3.31. A portion of the electrical power, specified

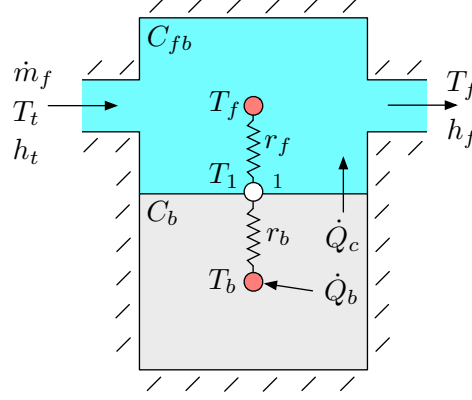


Figure 3.5: Pulsed Load Thermal Model.

by K_{heat} in Eq. 3.32, increases the internal energy of the lumped thermal body via \dot{Q}_{pl} . The total heat rate applied to the lumped thermal mass is given in Eq. 3.33 where the pulsed load contribution is added to the losses from pumping and the losses within the power converters which also require cooling. The pumping losses are equal to $i_m^2 R_m$ where R_m accounts for both the ohmic losses within the motor and its mechanical efficiency. In Figure 3.5, the lumped mass of the fluid within the coolant passages for the thermal load had a thermal capacitance of C_{fb} . Similarly, the thermal mass associated with the heat generating portions of the pulsed load, power converters, and coolant pump had a thermal capacitance of C_b . Heat transfer from the pulse load body to the coolant is given by \dot{Q}_c . The inlet coolant temperature from the tank T_t is assumed to completely mix within the coolant passages to a temperature of T_f and equal to the temperature returned to the tank. The boundary temperature between the coolant passage and pulsed load is denoted T_1 . Constant thermal conductive resistances, r_f and r_b model heat flow as temperature differences between the two lumped masses.

$$i_{pl} = \frac{P_{pl}}{v_{HP}} \quad (3.31)$$

$$\dot{Q}_{pl} = P_{pl} K_{heat} \quad (3.32)$$

$$\dot{Q}_b = \dot{Q}_{pl} + i_m^2 R_m + \left[i_{HPS}^2 R_{HPS} + i_{MBFC}^2 R_{MBFC} + i_{LPS}^2 R_{LPS} + i_{HPFC}^2 R_{HPFC} \right] \quad (3.33)$$

Two temperature differential equations can be written for the coolant contained within the coolant passages and pulsed load body by applying conservation of energy, yielding Eq. 3.34. The change in enthalpy between the inlet and outlet is approximated by $h_t - h_f = c_{pf} (T_t - T_f)$, where c_{pf} represents the average specific heat capacity.

$$\begin{aligned} C_{fb} \dot{T}_f + \left(\dot{m}_f c_{pf} + \frac{1}{r_f + r_b} \right) T_f - \left(\frac{1}{r_f + r_b} \right) T_b &= \dot{m}_f c_{pf} T_t \\ C_b \dot{T}_b - \left(\frac{1}{r_f + r_b} \right) T_f + \left(\frac{1}{r_f + r_b} \right) T_b &= \dot{Q}_b \end{aligned} \quad (3.34)$$

The entropy generation rate, which is proportional to the exergy destruction rate, for cooling the pulsed load is based on simplifying both the model notation of [46]

and considering the pulse load system as insulated from its surroundings, is given as Eq. 3.35.

$$\dot{S}_{gen,pl} = \frac{(T_b - T_f)^2}{T_b T_f (r_f + r_b)} + \dot{m}_f c_{pf} \left[\ln \left(\frac{T_f}{T_t} \right) - \frac{T_f - T_t}{T_f} \right] \quad (3.35)$$

3.3.2.2 Coolant Tank

The coolant tank, depicted in Figure 3.6, represents the bulk fuel storage for the aircraft and serves as thermal storage to which waste heat is rejected from the pulsed load. The tank is insulated from the ambient surroundings. For the sake of simplicity, the fuel volume is considered constant in this study, although would be changing in a physical system.

A temperature differential equation for the tank temperature, T_t , can be written as Eq. 3.36, where we define the thermal capacitance as C_t , and average specific heat capacity for the tank fluid as c_{pt} . As follows from [46], the entropy generation rate for the tank is found to be Eq. 3.37.

$$c_{th,t} \dot{T}_t = \dot{m}_f c_{pt} (T_f - T_t) \quad (3.36)$$

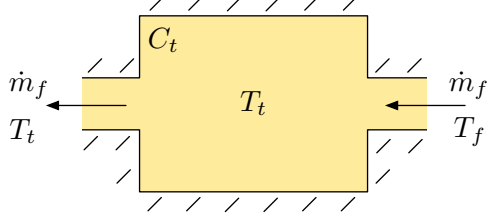


Figure 3.6: Coolant Tank Thermal Model.

$$\dot{S}_{gen,t} = c_{pt} \dot{m}_f \left[\frac{T_f - T_t}{T_t} - \ln \left(\frac{T_f}{T_t} \right) \right] \quad (3.37)$$

The exergy destruction associated with the pulsed load and coolant system, \dot{X}_{th} is given in Eq. 3.38, where the entropy generation rates are multiplied by the dead state temperature, T_0 .

$$\dot{X}_{th} = \left(\dot{S}_{gen,pl} + \dot{S}_{gen,t} \right) T_0 \quad (3.38)$$

3.4 Optimal Electrical Grid Management

The Hamiltonian control strategy in Section 3.2 requires setting reference values, \mathbf{x}_R , to guide the system to desired operating points. For the aircraft networked microgrid architecture, minimizing storage contribution and system wide exergy destruction are

reasonable goals aligned with minimizing heat signature and maximizing flight time. To achieve these ends, we apply a general optimization method to the model specific system equations of Eq. 3.24 through Eq. 3.27.

An exergy optimal cost function based on ohmic losses within the power converters is given in Eq. 3.39 as applied to the aircraft problem. When minimizing J , the solution must satisfy the power flow equations given as Eq. 3.40 where the dynamics have been considered steady state and the storage contributions set to zero.

$$J = \frac{1}{2} \left(i_{HPS}^2 R_{HPS} + i_{MBFC}^2 R_{MBFC} + i_{LPS}^2 R_{LPS} + i_{HPFC}^2 R_{HPFC} \right) \quad (3.39)$$

$$\begin{aligned} 0 &= -R_{HPS} i_{HPS} - v_{MB} + D_{HPS} (v_{HPS}) \\ 0 &= -R_{LPS} i_{LPS} - v_{HP} + D_{LPS} (v_{LPS}) \\ 0 &= -R_{MBFC} i_{MBFC} + (1 - D_{MBFC}) v_{MB} - D_{MBFC} v_{FC} \\ 0 &= -R_{HPFC} i_{HPFC} + (1 - D_{HPFC}) v_{HP} - D_{HPFC} v_{FC} \\ 0 &= (1 - D_{MBFC}) i_{MBFC} - \frac{v_{MB}}{R_{MB}} - i_m \\ 0 &= (1 - D_{HPFC}) i_{HPFC} - \frac{v_{HP}}{R_{HP}} - i_{pl} \\ 0 &= D_{MBFC} i_{MBFC} + D_{HPFC} i_{HPFC} - \frac{v_{FC}}{R_{FC}} \end{aligned} \quad (3.40)$$

The optimization strategy was implemented in Simulink by calling `fmincon` within level-2 M-coded S-function. The nonlinear constraints and cost function were implemented in C-Code and called through MEX wrapper functions to improve execution speed. The initial conditions are configured by a script for the first optimization step and further optimization runs start with the previously obtained solution to further reduce execution time and works well if the present system's operating point is its previously optimized value.

3.5 Simulation Runs

In the following simulation runs, the pulsed load was exercised on a continuous basis where the pulsed power electrical load was equal to 100 kW with a 50 % duty cycle and two second period for a total of 30 pulses.

3.5.1 Exergy Based Thermal Management

The boundary temperature within the coolant passages, denoted T_1 in Figure 3.5, must remain below 162.8 °C which is the fouling temperature of kerosene. An infinite amount of temperature set points exist for T_1 and are bound by the aforementioned upper limit and the present tank temperature as an increasing lower limit. Allowable

coolant flow rates also factor into the cooling performance as the tank temperature approaches the desired boundary temperature, cooling can no longer be achieved and theoretical flow rates tend toward infinity. To study the affects of different temperature set points had on the overall system exergy destruction a PI closed loop controller was implemented on the coolant pump flow rate. In Eq. 3.41, the pump command is $\dot{m}_{f,cmd}$, the boundary temperature T_1 and the desired reference temp T_{ref} . The negative sign on the error term, e_{pump} signifies the controller is reverse acting where higher flow rates equal lower temperatures. The gains were selected to provide adequate performance through a range of operating temperatures and set to $P_{pump} = 1.0$, $I_{pump} = 0.4$. Commanded flow rates were limited between $\dot{m}_{cmd,ll} = 0.001$ kg/s and $\dot{m}_{cmd,ul} = 10$ kg/s and integral windup was handled by clamping the output between these limits.

$$\begin{aligned}\dot{m}_{f,cmd} &= P_{pump} e_{pump} + \int_{t_0}^{t_1} I_{pump} e_{pump} \\ e_{pump} &= -(T_{ref} - T_1) \\ \dot{m}_{cmd,ll} &\leq \dot{m}_{cmd} \leq \dot{m}_{cmd,ul}\end{aligned}\tag{3.41}$$

Time domain evolution of particular states for a single execution, as opposed to only their final values used later, is given in Figure 3.7. The thermal masses boundary temperature T_1 is allowed to heat until the reference temperature T_{ref} is reached at 34 s when the pump is engaged and active cooling begins. The tank temperature,

T_t remains essentially constant at 20 °C until 34 s when it begins to rise due to the mixing with the heated coolant and reaching 22.6 °C at 60 s. The total heat energy, Q_d applied to the thermal mass is integrated over time from Eq. 3.33. The pump's energy consumption, $\int v_{MB} i_m$, was negligible prior to 34 s and follows a similar trend to the systems total exergy destruction reaching 90.2 kJ after 60 s for this case. The trends observed here suggest that if T_{ref} were set higher than 104 °C, less exergy would be destroyed for the same number of pulses, the pump energy use would be lower and potentially more pulses could be handled due to a lower final tank temperature.

To explore the affects of set point and fuel levels, the model was executed for fifty linearly spaced temperatures ranging from $T_{ref} = 60$ °C to 150 °C and four tank thermal capacitances $C_t = 1020.6$ kJ/K to 6124 kJ/K; a thermal capacitance of 6124 kJ/K is equivalent to 2000 US gal of Jet A-1 fuel. We have chosen the maximum T_{ref} as 150 °C providing head room from the 162.8 °C limit. A total of 30 pulses occurred during each 60 s execution and final values of interest were recorded in Figure 3.8. As C_t was reduced, so was total exergy destruction regardless of the temperature set point T_{ref} for the boundary point T_1 . This reduced exergy destruction was due to the tank temperature increasing more rapidly for the lower capacitance cases and the output temperature between the fluid in the body and tank were closer together thereby reducing entropy production. Lower C_t values also resulted in higher final tank temperatures for the same number of pulses. Pump utilization was higher for lower C_t values due to the rising tank temperatures. Now considering the variation of

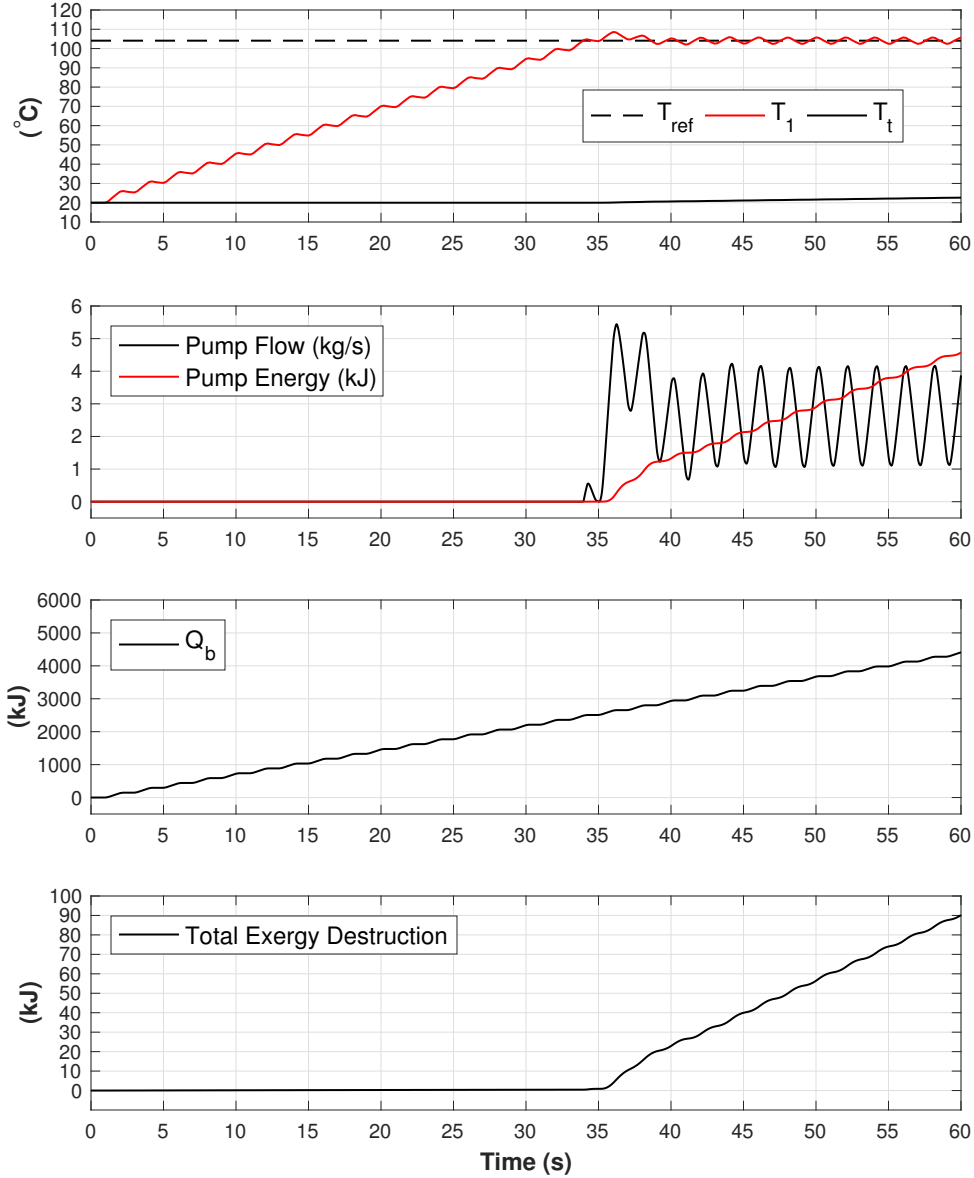


Figure 3.7: Dominant Thermal Model States where $C_t = 3855.9$ kJ/K and $T_{ref} = 104.0$ °C.

T_{ref} , a maximum exergy destruction is observed in the 90 °C to 100 °C range depending upon C_t and should be avoided if possible. If minimum exergy destruction was sought, two potential solutions could be arrived at if the T_{ref} maximum temperature were lower than the tested value of 150 °C. For example, for C_t , a similar exergy

destruction was found at $T_{ref} = 60$ °C and $T_{ref} = 125$ °C. Upon further investigation, the system efficiency can be greatly improved by selecting the higher 125 °C set point. If allowable, considering other constraints beyond just fouling temperature of the coolant, selecting an operating temperature of $T_{ref} = 150$ °C resulted in the least exergy destruction, lowest tank temperatures, and least pump utilization. Even more interesting is each of the three metrics, exergy, energy, and tank temperature converge to the same solution of maximizing the T_{ref} set point and essentially, not cooling the load.

3.5.2 Bus Voltage Regulation Performance Relative to Optimization Update Rate

Bus regulation performance is affected by the optimization update rate and performance improves with increased rates. Update rate is limited by algorithm's execution rate which is dependent on grid size and the algorithm's implementation as studied by Trinklein et al. [43]. A timing study of the presented optimization strategy is given in Table 3.3, where increasing the update rate from 0.2 s to 0.02 s, a ten fold increase, resulted in taking 5.5 times longer on average for the full simulation. This lower growth rate of execution time, less than 1 to 1, is attributed optimal set point solutions be closer together for smaller time steps where the solutions steps converge to similar answers as the time step is reduced at each optimization epoch.

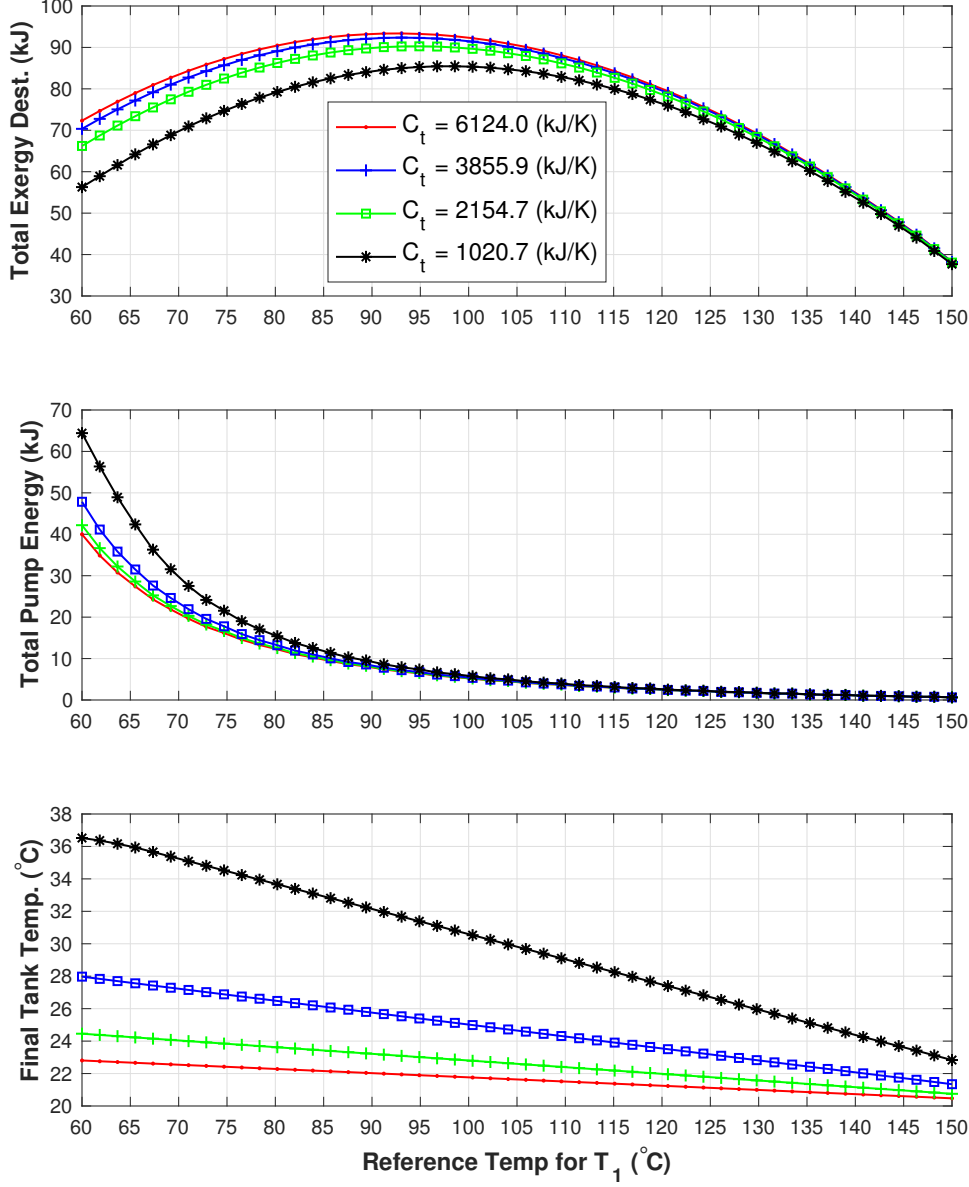


Figure 3.8: System Exergy, Pump Energy, and Tank Temperature as a Function of T_{ref} and C_t .

There is a trade off between optimization update rate, bus voltage performance, and storage utilization. To show the bus performance as a function of optimization update rate, four rates 0.02 s, 0.05 s, 0.1 s, and 0.2 s were plotted vs. the bus voltages in Figure 3.9. The simulation is shown at 34.5 s to 37.5 s into the run to show the

Table 3.3
Normalized Simulation Timing Study of Optimization Update Rate

Execution Time (s/s)	dt (s)
1	0.2
1.5	0.1
2.4	0.05
5.5	0.02

point where the reference temperature of T_1 has reached T_{ref} and the coolant pump is activated and the results are consistent those in Figure 3.7.

All voltages busses were maintained within 3 % (± 8.1 V) of their 270 V set points. The v_{FC} bus maintained $270 \text{ V} \pm 0.1 \text{ V}$ or 0.03 %, stabilized by u_{EAU} , therefore not plotted. The MB bus lacks storage and therefore its voltage is maintained solely by the optimization strategy and benefits from higher update rates. The time varying load on MB was the pump where a peak power of 640 W or a current of 2.37 A was applied. The 100 kW pulse load, P_{pl} , was applied to the HP bus and stabilized by the Hamiltonian through u_{HSEM} storage. Here, the benefit of increased optimization update rate is apparent where the storage is nullified after 0.05 s for $dt = 0.02$ s and remains active for 0.2 s with $dt = 0.2$ s. This shows that shortening the update rate lowers the required energy capacity for the storage, although the required power delivery remains similar for each of the update rates. The initial transient behavior events, aligned with changes in P_{pl} at 35 s or 36 s, was observed for each update rate to the extent that the voltage excursions lie on top of one-another. Then, depending on the update rate, a second voltage excursion occurs to nullify the storage command.

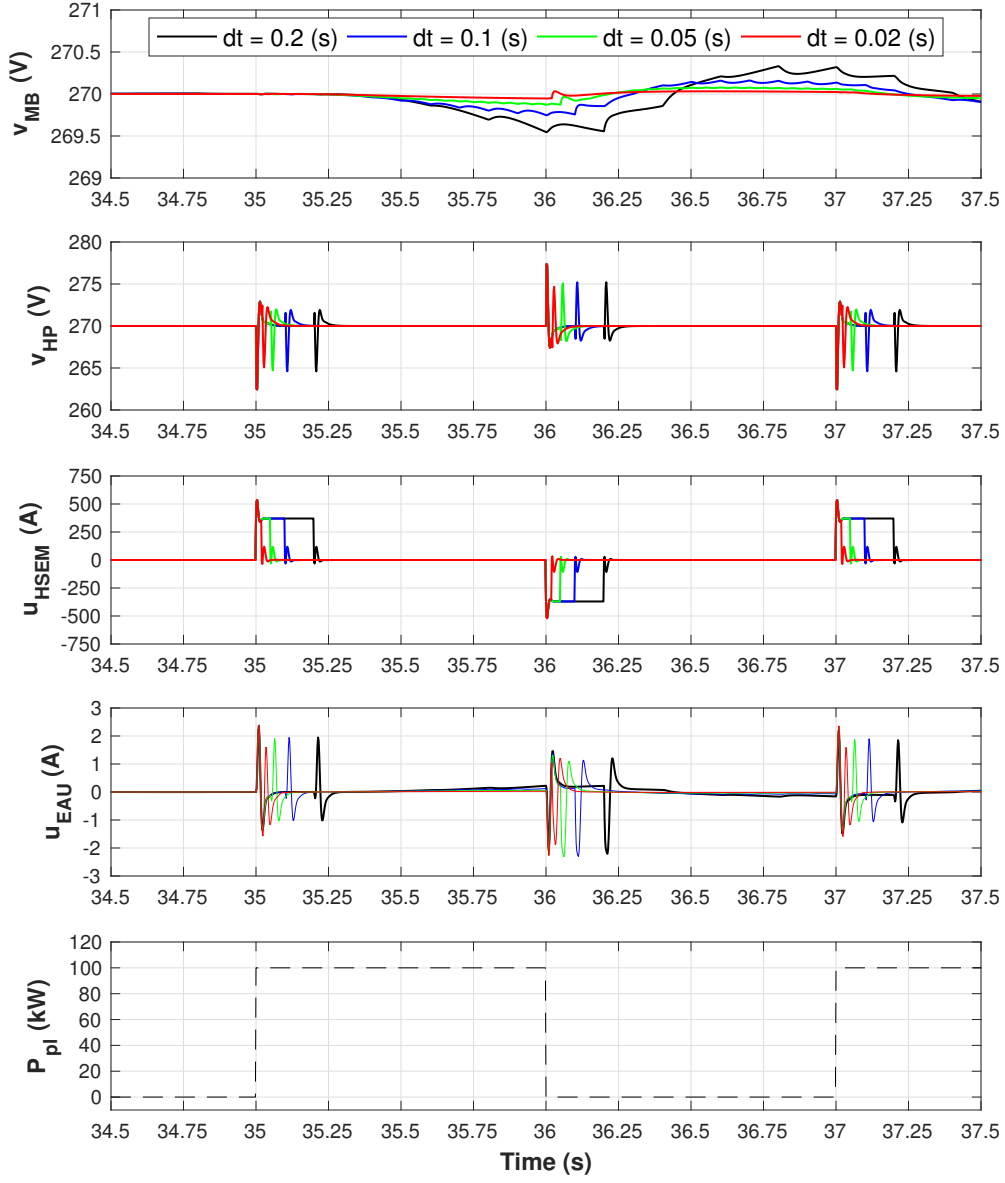


Figure 3.9: Bus Voltages vs. Optimization Update Rate, dt , where $C_t = 3855.9$ kJ/K and $T_{ref} = 104.0$ °C.

3.6 Conclusions

Operating the coolant system at the near limiting temperatures, resulted in the lowest exergy destruction, most electrically efficient operation of the coolant pump and allowed lower tank temperatures. However, cooling the load is a necessary task and other constraints, beyond the 162.8 °C fuel limit might be imposed. In such cases, operating at a peak exergy destruction point may result in the most electrically efficient operation from the pump energy stand point. This result is somewhat unintuitive from an engineering standpoint where keeping system boundary temperature as low as possible is a likely solution.

The Hamiltonian controller and optimal set point generation scheme share a symbiotic relationship. The Hamiltonian controller provides asymptotic system stability through idealized, distributed, storage but requires the generation set points to minimize storage utilization. Alternately, the optimal set point generator provides a minimal exergy solution and avoids storage use but may lack sufficient update to stabilize bus voltages and the assumption that the system has reached steady state at each optimization epoch is violated on occasion. When operated together, both control strategies provide adequate bus voltage regulation and system stability.

In future work, adding loss terms to the storage elements and tying their heat generation into the thermal mass would add realism and allow for better performance comparisons between control strategies that achieve stability through installed generation only.

Chapter 4

Hardware-in-the-Loop Verification of Exergy Optimal Microgrid Control Strategy¹

In this chapter, the networked microgrid model from Chapter 3 is expanded to run at real-time on HIL simulators. The numerical optimization technique from Chapter 2 was extended to interact with the HIL microgrid through UDP Ethernet communication. Grid stability is managed by the HSSPFC strategy. Implementation details are given including wiring, calibration, and signal scaling. Some of the major challenges and their solutions are described for operating the HIL simulators and optimization

¹The material contained in this chapter has been submitted to *International Journal of Electrical Power & Energy Systems*.

strategy together. This chapter summarizes the development of a co-simulation test bench used to verify the aforementioned optimization strategy and could be used as the basis for future advanced control techniques.

4.1 Microgrid Model

The microgrid model is broken into two parts, the electrical circuit which runs on a Typhoon HIL 600 and a thermal cooling model for the pulsed load which runs on an Opal-RT OP5700 system.

4.1.1 Electrical System - Typhoon HIL

A three bus microgrid system was proposed in [1] and utilized in this work, where two buses have a single generator and are interconnected through bi-directional power converters, as shown in Figure 4.1. A pulsed 100 kW load on the FC bus represents the dominant system load. A pumping load from a cooling system couples the electrical and thermal models. The FC bus and HP bus have current injections managed by a Hamiltonian control strategy. In this work, the circuit was implemented on a Typhoon HIL 600 where switching dynamics are modeled in real-time. The top level subsystem model is shown in Figure 4.2 and detailed circuit diagrams of each

subsystem are located in Appendix C.

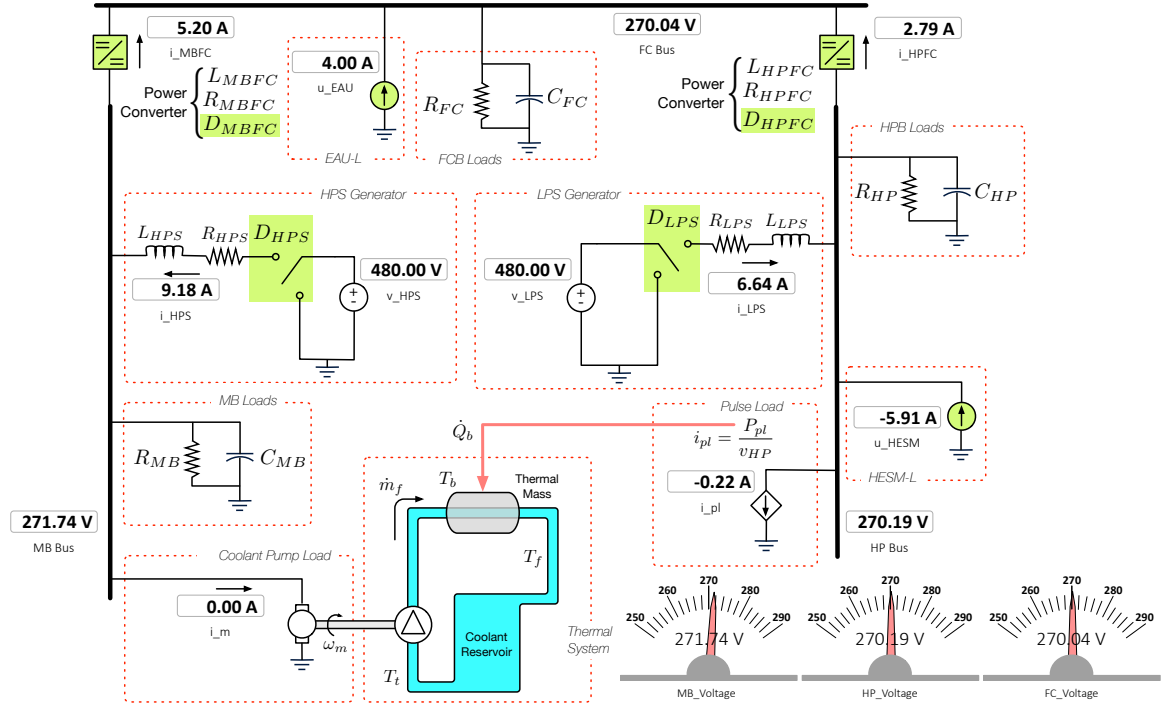


Figure 4.1: SCADA Interface of Three Bus Interconnected Microgrid Block Diagram and based on [1].

Applying Kirchhoff's voltage and current laws, the electrical dynamic equations for the three bus system can be written as Eq. 4.1 for the generator buck converters, the interconnecting buck-boost power converters, and the three buses, from [1]. Examples of inductance values are denoted as L_{HPS} , resistance values as R_{HPS} , voltages as v_{MB} , currents as i_{MBFC} , and duty cycles as D_{MBFC} where the values used in this model can be found in Table 3.1 of Chapter 3. The basis of an optimal model based control strategy of Section 4.3.3 is the average mode electrical dynamic equations of Eq. 4.1.

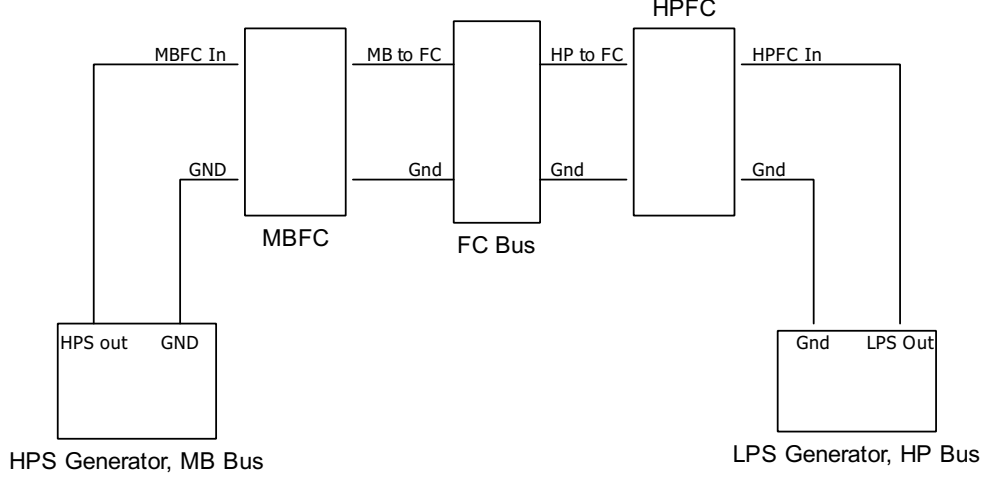


Figure 4.2: Top Level Model Schematic as implemented on the Typhoon HIL 600.

$$\begin{aligned}
 L_{HPS} \frac{di_{HPS}}{dt} &= -R_{HPS} i_{HPS} - v_{MB} + D_{HPS} v_{HPS} \\
 L_{LPS} \frac{di_{LPS}}{dt} &= -R_{LPS} i_{LPS} - v_{HP} + D_{LPS} v_{LPS} \\
 L_{MBFC} \frac{di_{MBFC}}{dt} &= -R_{MBFC} i_{MBFC} + (1 - D_{MBFC}) v_{MB} - D_{MBFC} v_{FC} \\
 L_{HPFC} \frac{di_{HPFC}}{dt} &= -R_{HPFC} i_{HPFC} + (1 - D_{HPFC}) v_{HP} - D_{HPFC} v_{FC} \\
 C_{MB} \frac{dv_{MB}}{dt} &= (1 - D_{MBFC}) i_{MBFC} - \frac{v_{MB}}{R_{MB}} - i_m \\
 C_{HP} \frac{dv_{HP}}{dt} &= (1 - D_{HPFC}) i_{HPFC} - \frac{v_{HP}}{R_{HP}} - i_{pl} + u_{HESM} \\
 C_{FC} \frac{dv_{FC}}{dt} &= D_{MBFC} i_{MBFC} + D_{HPFC} i_{HPFC} - \frac{v_{FC}}{R_{FC}} + u_{EAU}
 \end{aligned} \tag{4.1}$$

4.1.2 Pulsed Load and Thermal System - Opal-RT

The system's thermal model is from [1], can be found as a block diagram in Figure 4.1, and is summarized below. The 100 kW pulse device was implemented through the current source of i_{pl} on the HP bus and also applies 80 % of this power as heat rate, \dot{Q}_b , into a lumped thermal mass. Additionally, the pump's $i^2 R$ losses and those from the power converters as also applied to the thermal mass in Eq 4.2. The thermal mass has a temperature of T_b and is actively cooled by fluid, in this case kerosene, from a coolant reservoir with temperature T_t . The coolant reservoir and thermal mass are insulated from the environment. The coolant flows through the thermal mass where heat is exchanged by conduction and convection. A coolant pump produces a mass flow rate, \dot{m}_f through the thermal mass and is coupled to the MB bus by current draw i_m .

$$\begin{aligned} \dot{Q}_b = & k_{heat} i_{pl} v_{HP} + i_m^2 R_{pump} + i_{HPS}^2 R_{HPS} + i_{LPS}^2 R_{LPS} + i_{MBFC}^2 R_{MBFC} \\ & + i_{HPFC}^2 R_{HPFC} \end{aligned} \quad (4.2)$$

4.2 Hardware Description

There are three key pieces of hardware utilized in this model configuration, as shown in Figure 4.3. The electrical model is implemented on the Typhoon HIL 600 simulator allowing a 1 MHz update rate of the electrical system. Communications between the Typhoon and Opal-RT systems were accomplished using an analog/digital I/O board on the Typhoon and the FPGA based analog/digital I/O on the Opal-RT. The Opal-RT OP5700 system is responsible for running the Hamiltonian control strategy, the thermal model, and providing an Ethernet UDP interface to the optimization control strategy and executed at 500 Hz. A Dell 7720 Windows 10 Laptop was responsible for building and executing the different HIL models and for implementing an optimization strategy for computing the power converter duty cycle settings at 50 Hz. Other useful development features are the Supervisory Control and Data Acquisition (SCADA) interface, the IP power outlet allowing remote utilization of the HIL system, and Tektronix oscilloscope for debugging of electrical connections.

4.2.1 Connections Between Equipment

Analog and digital connections between the Opal-RT and Typhoon allow for the co-simulation of the full microgrid system. The buck and boost PWM signals are

generated in the Opal-RT and for commutation of the respective power converter switches on the Typhoon. Required voltage and current signals are transmitted via the Typhoon I/O board to the Opal-RT by 22 ga multi-conductor cables, as detailed in Table C.1 and Table C.2. In these tables, the connections are from the perspective of the Typhoon, which has a smaller I/O configuration than the Opal-RT. Pulse Width Modulated (PWM) frequencies were selected to provide relatively low converter current fluctuation by skewing the frequencies between the converters. The buck/boost converters are configured with the same complimentary duty cycle frequency to ensure proper operation. For the analog signals, the physical voltage limits are -5 to 5 volts which are then scaled to the appropriate level within both the Opal-RT and Typhoon models as shown in Table C.2.

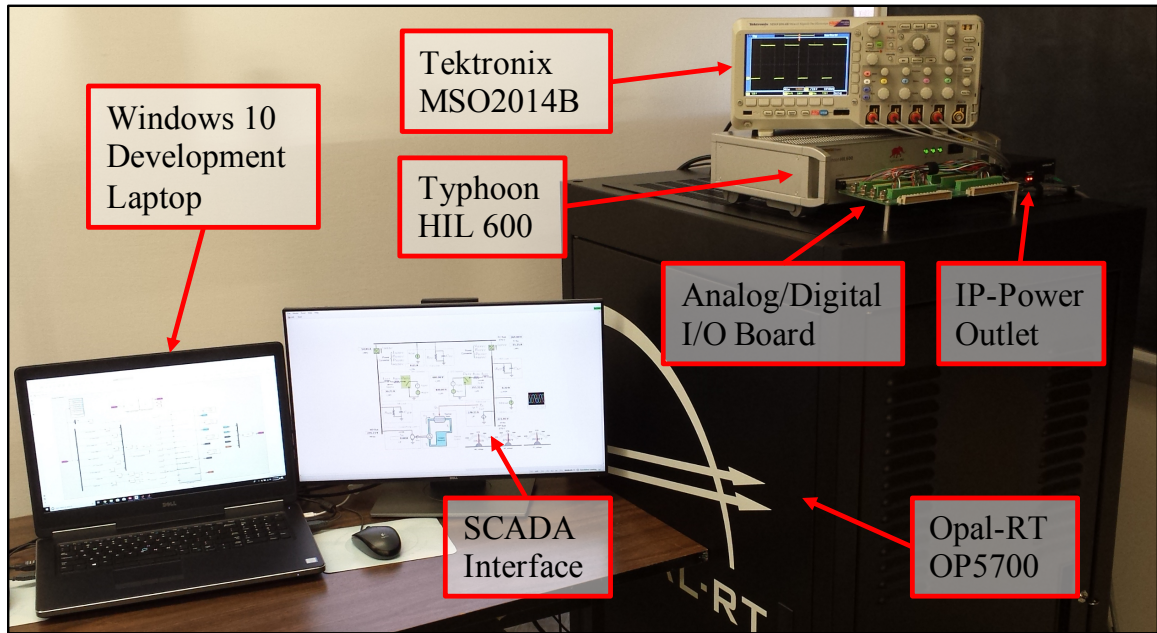


Figure 4.3: HIL Hardware Setup.

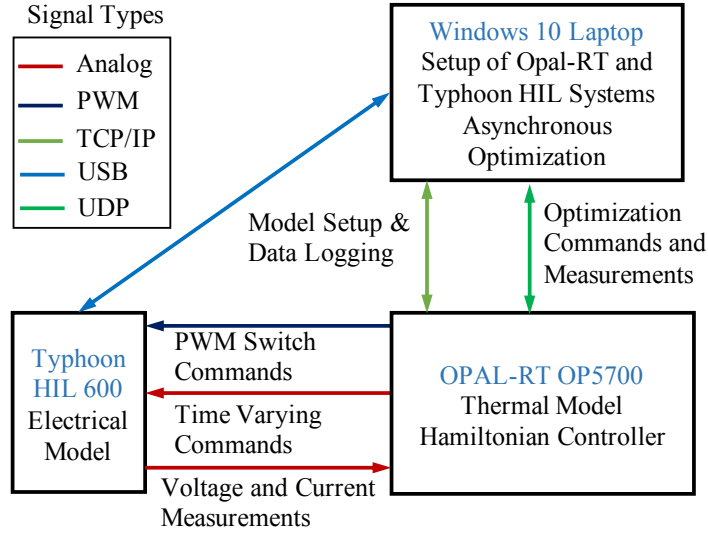


Figure 4.4: Block Diagram of Co-Simulation and Communication Signal Types.

4.2.2 Data and Model Synchronization

Co-simulation of the thermal and electrical models on two different hardware platforms pose certain challenges. The first is to synchronize data logging for analysis and plotting. This was accomplished by having a repeating digital synchronization pulse sequence recorded by both the Opal-RT and Typhoon systems. A second digital signal was used to trigger the Typhoon's SCADA data logging. The trigger, activated by the user on the Opal-RT Console, was also used on the Opal-RT for starting its data logging. Additionally, to easy comparisons across multiple simulation runs, the thermal system was prevented from increasing in temperature by nullifying the \dot{Q}_b until data logging and pulse device loading had started on both systems. Otherwise, starting temperatures of the cooling system could vary between runs.

4.2.3 Analog Channel Calibration

A critical step in configuring the Opal-RT to Typhoon HIL connections was calibrating the analog I/O channels. The Typhoon HIL 600 had a total of 8 analog inputs and 16 outputs which is a subset of the I/O provided by the Opal-RT OP5700. To simplify future model development all of the Typhoon's analog I/O channels were connected and calibrated with the following semi-automated procedure. Both the Opal-RT and Typhoon were configured for each analog channel repeatably cycle through three voltage levels of -4.5 V, 0.0 V, and 4.5 V, holding at each set point for 2 S. The -4.5 V to 4.5 V applied range accounts for 90 % of the full range voltage; providing headroom for bias and noise on the raw data. Data was then collected from both systems and processed with a MATLAB script and computation function with the steps as follows:

1. At a given voltage set point, define a search range of ± 1.5 V.
2. Extract subset of data within the the search range.
3. Find longest contagious block of data (approximately 2 s).
4. Removed the first and last 5 % of this data to remove transitions.
5. Compute the mean value of this data block, resulting in a calibration point.
6. Repeat steps 1 through 5 for the other calibration levels.

7. Apply a linear regression to the calibration points to determine gain and bias values.
8. Repeat steps 1 through 7 for each analog channel.

The results of this procedure are shown in Figure 4.5 where both the raw data and calibrated data are shown overlaid. This three point calibration was sufficient in this case although more calibration points could be added to this procedure with the limitation becoming the search range set in step 1 of the procedure.

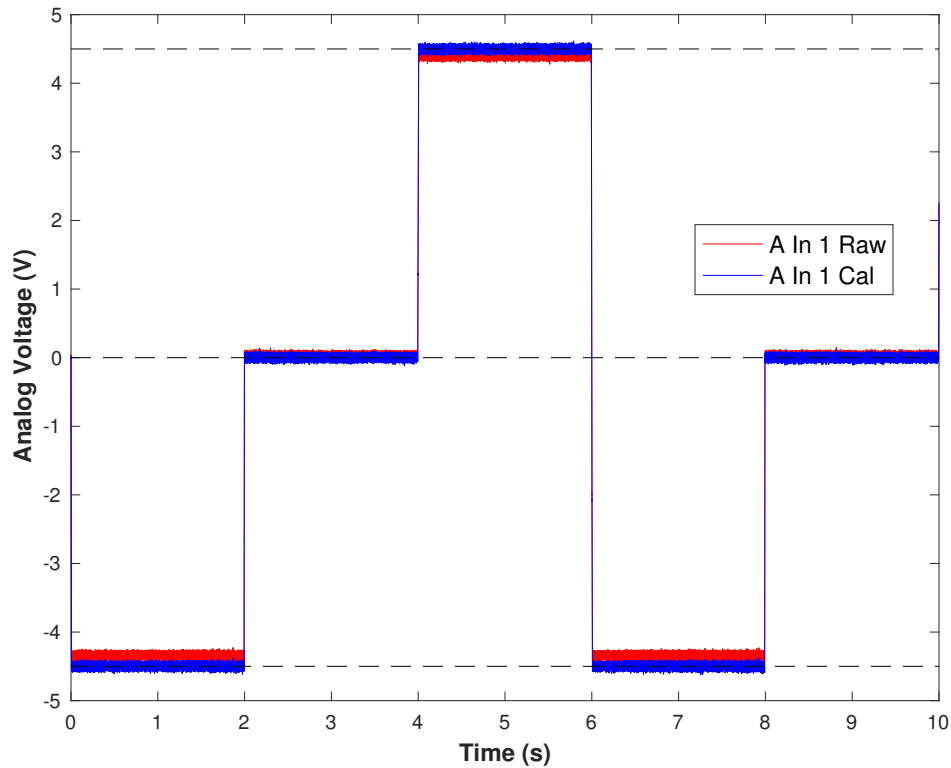


Figure 4.5: Calibration Result of Typhoon Analog Channel 1.

4.2.4 Online Duty Cycle Bias Determination

During the development of the optimal control strategy, the computed PWM duty cycles and reference currents did not produce the expected bus voltages on the HIL system. Upon investigation, the PWM duty cycles D_{HPS} , D_{HPS} , D_{MBFC} , and D_{HPFC} were within duty cycle value of 0.025 or 2.5 % of considering their full range values between 0 and 1. This difference is attributed to model differences such as small additional impedance required on the HIL for dividing the electrical circuit across multiple FPGA cores and dead time between switching events on the connection buck/boost converters introducing un-modeled nonlinear behavior.

The quality of the optimal control strategy depends on congruence between the HIL and theoretical model. Therefore, a method for determining the bias values of the commanded PWM duty cycles as a function of system loading was deemed necessary. At first inspection, a method of trial and error could produce acceptable agreement between the HIL and theory models for a single load value. For multiple load levels, as expected on any real system, an automated methodology is recommended. While many approaches could be used for this task, an interactive optimization strategy was developed.

The bias determination minimization problem is defined in Eq. 4.4 where the goals are to bring the bus voltages within an acceptable tolerance of $V_{err} = 2.7$ V or 1 % of the nominal bus voltage and to drive the resulting duty cycle values to also produce the theoretical power balance in the grid. The stored duty cycle values, e.g. D_{HPS}^* are the optimal solutions found from Section 4.3.3. The duty cycles were allowed to vary by $\beta = 5$ % of their optimal settings.

$$\begin{aligned}
& \min J_{bias}(D_{HPS}, D_{HPS}, D_{MBFC}, D_{HPFC}, i_m, i_{pl}) \\
& \text{subject to:} \\
& D_{HPS}^* \gamma \leq D_{HPS} \leq D_{HPS}^* \lambda \\
& D_{LPS}^* \gamma \leq D_{LPS} \leq D_{LPS}^* \lambda \\
& D_{MBFC}^* \gamma \leq D_{MBFC} \leq D_{MBFC}^* \lambda \\
& D_{HPFC}^* \gamma \leq D_{HPFC} \leq D_{HPFC}^* \lambda \\
& |V_{MB,ref} - V_{MB}| - V_{err} \leq 0 \\
& |V_{HP,ref} - V_{HP}| - V_{err} \leq 0 \\
& |V_{FC,ref} - V_{FC}| - V_{err} \leq 0
\end{aligned} \tag{4.3}$$

where:

$$J_{bias} = (V_{MB,ref} - V_{MB})^2 + (V_{HP,ref} - V_{HP})^2 + (i_{MBFC}^* - i_{MBFC})^2$$

$$\gamma = (1 - \beta)$$

$$\lambda = (1 + \beta)$$

The resulting duty cycle differences between the optimal values as compared to their calibrated true values, e.g. ΔD_{HPS} , were plotted against the dominant load i_{pl} are shown in Figure 4.6. Here we consider the True duty cycles found with Eq.4.4 and Optimal values as those found using Eq. 4.4. Due to the flatness of the duty cycle differences over the loading range, constant mean values was selected for the calibration. This avoided load dependence on the computed duty cycles which could arise if a linear or higher order fit were chosen for the calibration. The calibration values for each of the duty cycles are printed above each mean value line between 250 A and 350 A in Figure 4.6. The pumping load, i_m was not studied in this calibration because its full scale value was two orders of magnitude lower than the pulsed load value.

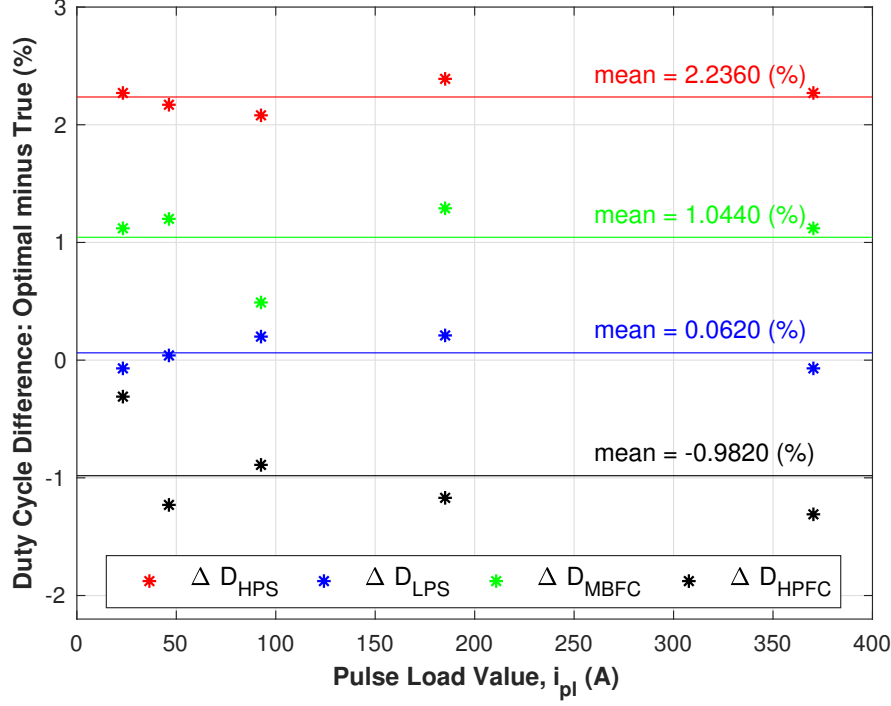


Figure 4.6: Calibration Result of Online Duty Cycle Determination Optimization.

4.3 Microgrid Control Strategy

A three pronged control strategy manages the pulsed load temperatures, bus voltages, and exergy optimal power flow control. The Hamiltonian controller provides closed loop bus voltage control to the HP and FC buses through usage of storage elements. The power flow optimization drives the storage use to zero while balancing the power flow throughout the electric grid. The pulsed load temperatures is managed by PI controller.

4.3.1 Hamiltonian Control

The Hamiltonian control strategy was implemented as described in [1]. The utility of this approach is to allow for asymptotic stabilization of the electric grid through strategically placed energy storage. In this case, the storage elements are the current injections of u_{EAU} and u_{HESM} . This distributed storage requires management so its utilization is minimized and main generators are used most effectively. A methodology for providing sub-second optimal grid storage and bus voltage management is explained in Section 4.3.3.

4.3.2 Thermal Controller

A PI controller regulates the boundary temperature, T_1 , of the thermal mass at the interface between coolant and inner surface of the thermal mass by varying the pump's flow rate. The exergy minimal solution from [1] is to operate the thermal system near its maximum allowable temperature, which for kerosene is 162.8 °C [47]. In this research, the temperature set point for T_1 was selected as 150.0 °C which yields near optimal exergy set point while avoiding the operating limits of the cooling fluid.

4.3.3 Optimizer Implementation

An exergy optimal electrical grid management strategy was developed in [1] which had been explored in [43] where the $i^2 R$ losses within each of the power converters were minimized. The optimization is defined formally in Eq. 4.4 where the constraints were the steady state power flow equations derived from Eq. 4.1. To drive the storage contributions, u_{HESM} and u_{EAU} to zero, their currents are omitted, forcing the solution to utilize the HPS and LPS generators for bus voltage regulation. Objective function and constraints implemented with as mexFunctions and called from within a Level 2 MATLAB S-function.

4.3.3.1 UDP Ethernet Communication

The optimization strategy implemented in MATLAB/Simulink utilizes the non-linear optimization tool `fmincon` which presently does not allow compilation to c-code, preventing direct integration onto the HIL system. A solution was to implement `fmincon` asynchronously using a separate model and UDP Ethernet as the communication technique between the Opal-RT OP5700 and a laptop executing the optimization strategy with an update rate of 50 Hz. The Simulink Desktop Real-Time UDP send and receive blocks in MATLAB 2018a were implemented to transfer data between the

systems. The laptops main Network Interface Card (NIC) was configured to an IP address of 192.168.8.12, gateway of 255.255.255.0, and local port 16384. The Opal-RT OP5700 had a dedicated four port Ethernet expansion card and used the AsyncEthernet communication drivers. One of the four expansion ports was configured with an IP address of 192.168.8.101, gateway of 255.255.255.0 and local port 55948.

Data exchanged between the models was cast to single precision floating point. The data sent to the optimizer was a combination of state data i_{HPS} , i_{LPS} , i_{MBFC} , i_{HPFC} , v_{MB} , v_{HP} , v_{FC} and load information i_m , i_{pl} . For the main optimization strategy explained in Section 4.3.3 the load information represents time dependent data while the other inputs to the constraint and objective functions are considered constant. In contrast, the online duty cycle bias determination optimization scheme of Section 4.2.4 uses the state information. The outputs transmitted back to the Opal are the optimal duty cycles applied to the Typhoon D_{HPS}^* , D_{LPS}^* , D_{MBFC}^* , D_{HPFC}^* , and current values i_{HPS}^* , i_{LPS}^* , i_{MBFC}^* , i_{HPFC}^* , used as references to the Hamiltonian controller. Debug information about the optimization solution is also transmitted to the Opal-RT. A USB to Ethernet converter was used for laptop to Opal-RT communication and model execution. This was done to avoid unnecessary network traffic while operating optimization strategy while also operating the Opal-RT system.

$$\min J_{ex} \left(D_{HPS}, D_{HPS}, D_{MBFC}, D_{HPFC}, i_{HPS}, i_{MBFC}, i_{HPFC} \right)$$

subject to:

$$0 = -R_{HPS}i_{HPS} - v_{MB} + D_{HPS}v_{HPS}$$

$$0 = -R_{LPS}i_{LPS} - v_{HP} + D_{LPS}v_{LPS}$$

$$0 = -R_{MBFC}i_{MBFC} + (1 - D_{MBFC})v_{MB} - D_{MBFC}v_{FC}$$

$$0 = -R_{HPFC}i_{HPFC} + (1 - D_{HPFC})v_{HP} - D_{HPFC}v_{FC} \quad (4.4)$$

$$0 = (1 - D_{MBFC})i_{MBFC} - \frac{v_{MB}}{R_{MB}} - i_m$$

$$0 = (1 - D_{HPFC})i_{HPFC} - \frac{v_{HP}}{R_{HP}} - i_{pl}$$

$$0 = D_{MBFC}i_{MBFC} + D_{HPFC}i_{HPFC} - \frac{v_{FC}}{R_{FC}}$$

where:

$$J_{ex} = \frac{1}{2} \left(R_{HPS}i_{HPS}^2 + R_{LPS}i_{LPS}^2 + R_{MBFC}i_{MBFC}^2 + R_{HPFC}i_{HPFC}^2 \right)$$

4.4 Results and Discussion

The 100 kW pulsed device was operated continuously at a 50 % duty cycle and two second period beyond the point where the pulse device's boundary temperature T_1 reached T_{ref} and required active cooling. The results collected span at least six orders of magnitude considering switching dynamics at approximately 10000 Hz to

the coolant response curve covering hundreds of seconds. Therefore the results are selected at different time scales to show salient details of how the models and control schemes interact, where the dominant dynamic responses are of interest. In the following plots, optimizer off means the duty cycles are fixed to provide bus voltages of 270 V at the loading case of $i_m = i_{pl} = 0$ A.

The behavior of the optimization strategy with respect to the time varying loads is shown in Figure 4.7 where the time frame shows three consecutive pulses and when the cooling system is active. At each load transition, e.g. 141 s and 142 s, new optimal duty cycles D_{HPS}^* through D_{HPFC}^* are computed. Duty cycle adjustments also occur in response to the cooling load P_m but are too small to be observed on in Figure 4.7 since the change in the D_{HPS}^* duty cycle was from 59.84 % to 59.91 % over the time frame of 141 s to 142 s. The difference in coolant loading, P_m , between Optimizer off vs. on might, at first interpretation, seem as though the performance worsens with optimal control enabled. This is actually an unfair comparison and will be explored further below.

A comparison of the optimizer off vs. on and the resulting bus voltages (v_{MB} , v_{HP} , & v_{FC}), Hamiltonian controller current injections (u_{HESM} & u_{EAU}), and the dominant pulse load power, P_{pl} is shown in Figure 4.8 over the same time frame as Figure 4.7. Each of the three bus voltages fall within 5 % or better of the nominal 270 V reference voltages. Voltage v_{MB} deviates from 270 V by approximately 1.5 V for two reasons,

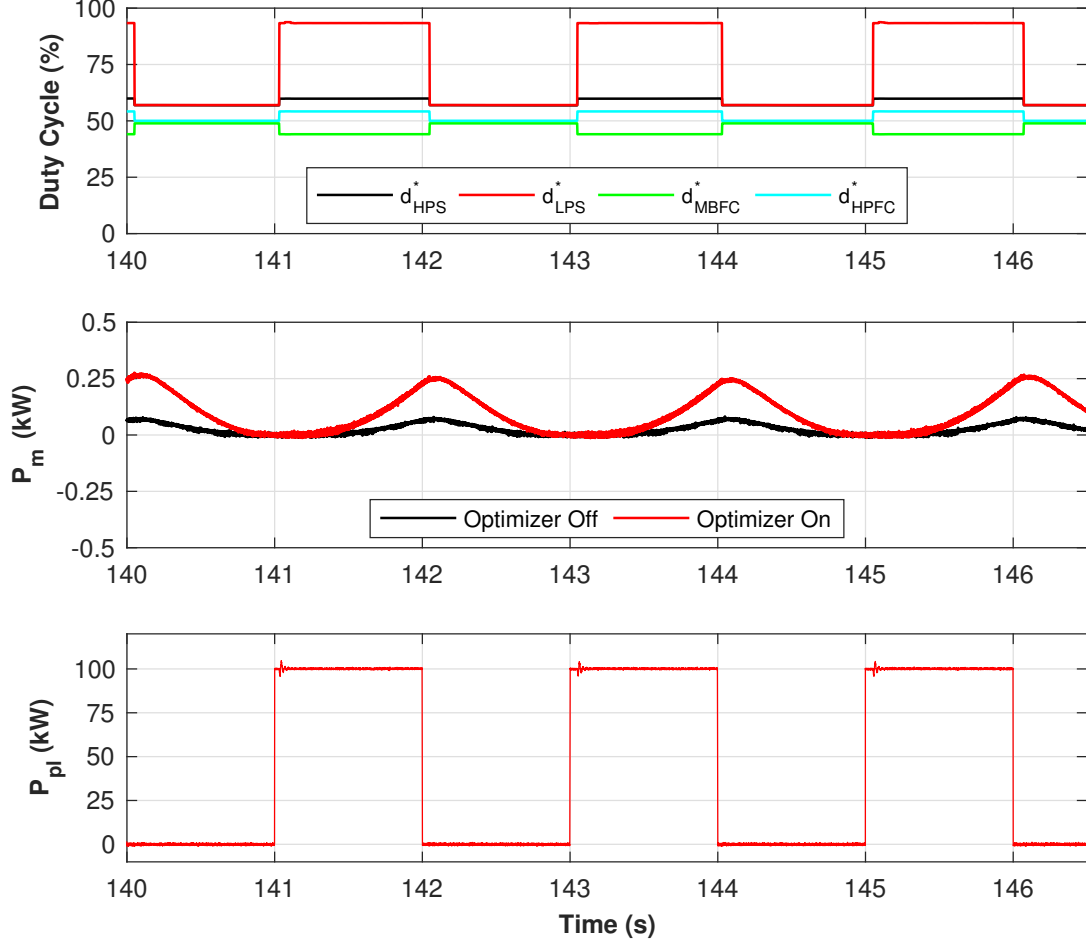


Figure 4.7: Optimal Duty Cycle Settings vs. Time Varying Load Powers.

the first being it lacks a Hamiltonian current injection and second there is error in the duty cycle settings even after applying the averaged duty cycle biases as computed with Eq. 4.4.

The Hamiltonian controller requires generation set points upon which it actuates storage to maintain bus voltages. Therefore, matching the generation to the load conditions is necessary to minimize storage utilization. Mismatch of generation to load conditions can be observed on u_{HESM} in Figure 4.8, where the optimizer substantially

reduces stored energy. Furthermore, errors in the duty cycle settings cause non-zero storage utilization on u_{EAU} when the pulse loading is disabled. This suggests that selecting the mean duty cycle bias from Section 4.2.4 maybe oversimplified for bringing the storage utilization to zero after loading changes. Storage utilization could be improved by adding a load dependence to the duty cycle bias correction.

In Table 4.1, the energy supplied to the electric grid by the Hamiltonian storage elements is given. A net negative energy reflects that the Hamiltonian storage was charging. Storage utilization was reduced by 42 fold using the optimized duty cycles compared to fixed duty cycles, by shifting the demanded load to the generators when computed as ϕ in Eq. 4.5. In Eq. 4.5, on means the optimizer is enabled, $t_1 = 0$ s and $t_2 = 150$ s. Ideally, the amount energy supplied by storage would tend towards zero when the optimizer is enabled. However, energy storage management at the minutes to hours time scale is still required for an actual system deployment and was not studied here.

$$\phi = \frac{|E_{HESM,off}| + |E_{EAU,off}|}{|E_{HESM,on}| + |E_{EAU,on}|},$$

where:

$$\begin{aligned} E_{HESM,i} &= \int_{t_1}^{t_2} u_{HESM}(t) v_{HP}(t) dt, \quad i = on, off \\ E_{EAU,i} &= \int_{t_1}^{t_2} u_{EAU}(t) v_{FC}(t) dt, \quad i = on, off \end{aligned} \tag{4.5}$$

Table 4.1
Energy Storage Requirements for u_{HESM} and u_{EAU} for 75 Pulses (kJ)

Optimizer Off		Optimizer On	
E_{HESM}	E_{EAU}	E_{HESM}	E_{EAU}
7303	166	-113	67

To better understand the optimizer's behavior to load changes, a zoomed in view of Figure 4.8 around 141.0 s is shown in Figure 4.9. The second order oscillatory behavior of v_{HP} bus can be clearly observed in response the optimizer input and u_{HESM} . There is a time delay from when the pulse load changes and when the disturbance occurs on v_{HP} . This disturbance is actually caused when the optimal solution is applied and the u_{HESM} storage is removed at around 141.02 s. There is a finite computation time (50 Hz update rate), network latencies, clock drift, and Windows 10 OS effects at play between the Opal-RT and optimization on the Dell laptop resulting in the time delay. The communication delay was timed using a loopback test while the optimizer was executed with the results found in Table 4.2. The best case communication delay is the 0.02 s or aligned exactly with the optimizer update rate. On average, the delay was found to be 0.053 s and with a maximum of 0.404 s from the data collected. Increases in time delay do not jeopardize bus voltage stability since the Hamiltonian controller maintains the bus voltage at the cost of increased storage utilization.

The thermal systems response is plotted in Figure 4.10 where both optimizer cases, on v.s off are studied. As mentioned above, the optimizer appears to cause the thermal

Table 4.2
UDP Round Trip Statistics (s)

Min	Median	Mean	Max
0.020	0.044	0.053	0.404

system to heat up more quickly than when it is disabled. In reality, there are missing loss terms associated with Hamiltonian current injections and not accounted for in the \dot{Q}_b of Eq. 4.2. This difference results in nearly a factor of two increase heat rate during pulse events or approximately $\dot{Q}_b = 147$ kW when the optimizer is on vs. $\dot{Q}_b = 80$ kW optimizer off in Figure 4.10. One method for accounting for losses within the storage would be to add in-line resistances with the current injections as in [48] and to add their heat rates to Eq. 4.2.

For this system, the number of pulse events is limited by the coolant thermal capacitance. Once the thermal mass boundary temperature $T_1 = 150$ °C is met this causes the cooling system to become active at 53.5 s and 98.0 s respectively for optimizer on vs. off. The pulse load can continue operation until the coolant tank temperature T_t approaches $T_{ref} = 150$ °C at which cooling is no longer possible. Beyond this point, active cooling of the tank would be required to continue pulsed device operation.

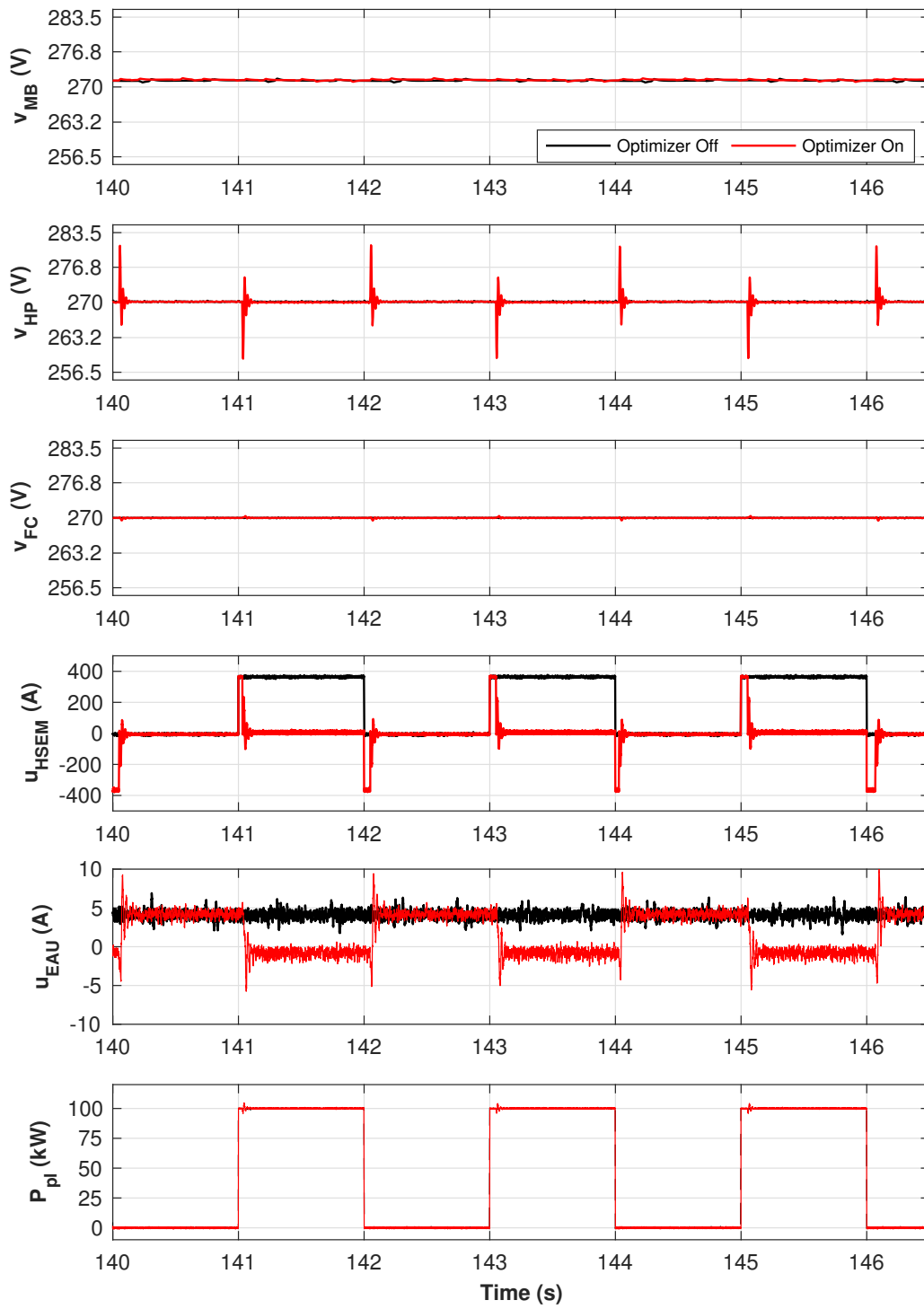


Figure 4.8: Bus Voltage Comparison Of Three Pulses With and Without Optimal Duty Cycle Settings.

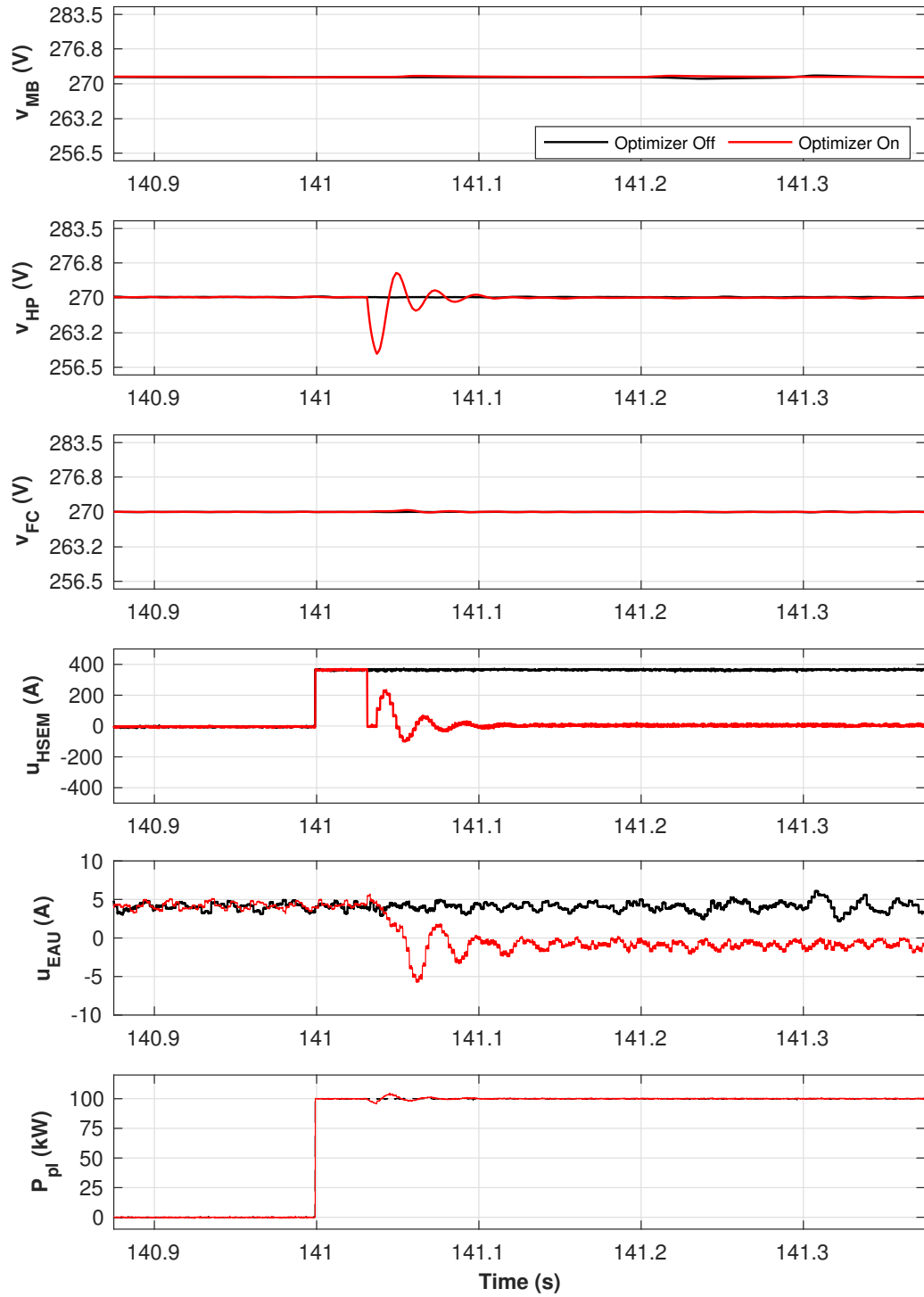


Figure 4.9: Zoomed In View of Bus Voltage Comparison.

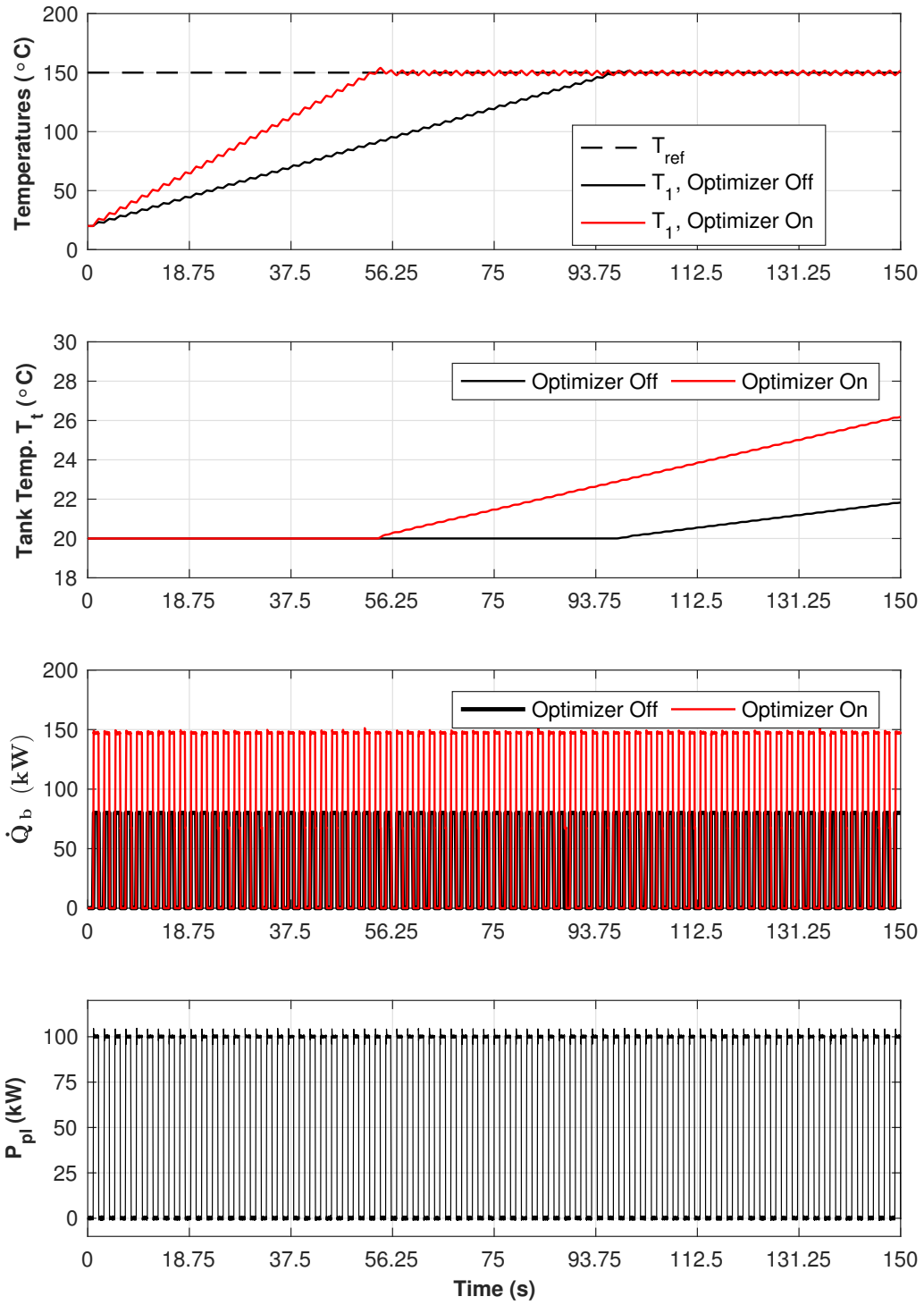


Figure 4.10: Thermal System Response Comparison With and Without Optimal Duty Cycle Settings.

4.5 Conclusions and Future Work

A Hardware-in-the-loop microgrid co-simulation system was developed using an Opal-RT OP5700 and Typhoon HIL 600 real-time simulators. The electrical connections, calibration procedures, and configuration details are provided. The microgrid model consisted of three dc buses, two generators, interconnecting power electronics and a thermal system responsible for cooling the power electronics and a pulsed load. A Hamiltonian control strategy was employed to ensure bus voltage stability for those buses with attached storage. An exergy based optimization strategy was deployed to control power flow within the microgrid at an update rate of 50 Hz. Communication between Opal-RT and a laptop running the optimization strategy was implemented through UDP ethernet communication. The optimization strategy reduced energy requirements by 42 fold as compared to fixed generation at the cost of transient bus voltage regulation. Voltage regulation was within 5 % for all three buses in both optimized and non-optimized cases.

In future work, the Hamiltonian control strategy requires more realistic storage models which include losses and thermal coupling for a fair comparison of the optimization's performance. Longer term energy management beyond second time scales would be required to ensure realistic storage constraints are met. Such a management system could interact with the optimization scheme developed in this work to

provide a slower outer loop control. The storage utilization could be further reduced by improving the UDP communication reliability. By reducing communication delay, the generation settings could be adapted more quickly and reduce storage use. A dedicated computer executing the optimization strategy is likely a solution vs. a single laptop operating the Typhoon, Opal-RT, and optimization simultaneously as studied in this work.

Chapter 5

Conclusion and Future Work

5.1 Conclusions

An exergy based networked microgrid optimization control strategy was developed to manage storage utilization in concert with recently developed control strategies such as the HSSPFC. There is a trade off between the optimization update rate and storage utilization. Additionally, the size of the microgrid and number of generation assets can change over time. Therefore, scalable and efficient optimization techniques were developed in three phases. First, combinations of closed-form and numerical methods were explored where time to solution was of interest as studied in Chapter 2. Second, a notional three bus microgrid model was implemented in offline simulation where

Hamiltonian and optimal control strategies were combined in Chapter 3. Third, the offline microgrid model was expanded to run as a co-simulation between two real-time HIL simulators where the optimization strategy was executed asynchronously through Ethernet communication, Chapter 4.

5.2 Suggestions for Future Work

The optimization strategy developed in this work is a proof-of-concept. Two steps could further improve its performance. First, there is likely a reduction in computational overhead that could be achieved by coding the optimization strategy in dedicated optimization software as opposed to MATLAB and Simulink. Second, the Ethernet UDP communication variability could be reduced using embedded hardware along with low overhead operating systems such as Linux.

To realize the optimization and control techniques explored in this work on real hardware, an outer loop energy management system would be needed. Such a system would provide longer term storage references in the minutes to hours time frame. This would also require more realistic storage models that take into consideration the internal losses, state of charge, and implementation specific details.

References

- [1] E. H. Trinklein, M. D. Cook, G. G. Parker, and W. W. Weaver Jr., *Exergy Optimal Multi-Physics Aircraft Microgrid Control Architecture*. International Journal of Electrical Power & Energy Systems, 2019, manuscript submitted for publication.
- [2] P. Asmus, *Microgrids, Virtual Power Plants and Our Distributed Energy Future*. The Electricity Journal, 2010, no. 10.
- [3] P. L. Joskow, *Chapter 16 Regulation of Natural Monopoly*, ser. Handbook of Law and Economics, A. Polinsky and S. Shavell, Eds. Elsevier, 2007, vol. 2.
- [4] R. H. Lasseter and P. Paigi, *Microgrid: a conceptual solution*. 2004 IEEE 35th Annual Power Electronics Specialists Conference, 2004, vol. 6.
- [5] E. Alegria, T. Brown, E. Minear, and R. H. Lasseter, “CERTS microgrid demonstration with large-scale energy storage and renewable generation,” *IEEE Transactions on Smart Grid*, vol. 5, no. 2, pp. 937–943, 2014.

- [6] W. V. Torre, N. Bartek, and B. Washom, “The san diego regional experience in developing microgrids, a collaboration between utility and a local university,” in *2012 IEEE Power and Energy Society General Meeting*, 2012, pp. 1–2.
- [7] H. Harris and J. Hodson, “Combined heat and power for industry,” in *2014 IEEE Electrical Power and Energy Conference*, 2014, pp. 281–283.
- [8] C. Wouters, E. S. Fraga, and A. M. James, “An energy integrated, multi-microgrid, milp (mixed-integer linear programming) approach for residential distributed energy system planning—a south australian case-study,” *Energy*, vol. 85, pp. 30–44, 2015.
- [9] M. Smith and D. Ton, “Key connections: The U.S. department of energy’s microgrid initiative,” *IEEE Power and Energy Magazine*, vol. 11, no. 4, pp. 22–27, 2013.
- [10] D. Boroyevich, I. Cvetkovic, D. Dong, R. Burgos, F. Wang, and F. Lee, “Future electronic power distribution systems a contemplative view,” in *Optimization of Electrical and Electronic Equipment (OPTIM), 2010 12th International Conference on*, 2010, pp. 1369–1380.
- [11] A. K. Srivastava, B. Annabathina, and S. Kamalasadan, “The challenges and policy options for integrating plug-in hybrid electric vehicle into the electric grid,” *The Electricity Journal*, vol. 23, no. 3, pp. 83 – 91, 2010.

- [12] C. Marnay, G. Venkataramanan, M. Stadler, A. Siddiqui, R. Firestone, and B. Chandran, “Optimal technology selection and operation of commercial-building microgrids,” *IEEE Transactions on Power Systems*, vol. 23, no. 3, pp. 975–982, 2008.
- [13] F. Kanellos, G. Tsekouras, and N. Hatziargyriou, “Optimal demand-side management and power generation scheduling in an all-electric ship,” *IEEE Transactions on Sustainable Energy*, vol. 5, no. 4, pp. 1166–1175, 2014.
- [14] D. J. Hammerstrom, “AC versus dc distribution systems did we get it right?” in *2007 IEEE Power Engineering Society General Meeting*, 2007, pp. 1–5.
- [15] R. Rudervall, C. J.P., and R. S., “High voltage direct current (HVDC) transmission systems technology review paper,” 2000.
- [16] J. Simpson-Porco, F. Dorfler, F. Bullo, Q. Shafiee, and J. Guerrero, “Stability, power sharing, and distributed secondary control in droop-controlled microgrids,” in *Smart Grid Communications (SmartGridComm), 2013 IEEE International Conference on*, 2013, pp. 672–677.
- [17] A. Basu, A. Bhattacharya, S. Chowdhury, and S. P. Chowdhury, “Planned scheduling for economic power sharing in a CHP-based micro-grid,” *IEEE Transactions on Power Systems*, vol. 27, no. 1, pp. 30–38, 2012.
- [18] E. Trinklein, G. Parker, W. Weaver, R. Robinett, L. G. Babe, C.-W. Ten, W. Power, S. Glover, and S. Bukowski, “Scoping study : Networked microgrids,”

Sandia National Laboratories, Albuquerque, NM, Tech. Rep. SAND2014-17718, 2014.

- [19] Z. Alaywan, “The tres amigas superstation: Linking renewable energy and the nation’s grid,” in *Power and Energy Society General Meeting, 2010 IEEE*. IEEE, 2010, pp. 1–5.
- [20] R. A. Rodriguez, S. Becker, and M. Greiner, “Cost-optimal design of a simplified, highly renewable pan-european electricity system,” *Energy*, vol. 83, pp. 658–668, 2015.
- [21] P.-O. Pineau, D. Dupuis, and T. Cenesizoglu, “Assessing the value of power interconnections under climate and natural gas price risks,” *Energy*, vol. 82, pp. 128–137, 2015.
- [22] T. Sousa, H. Morais, Z. Vale, and R. Castro, “A multi-objective optimization of the active and reactive resource scheduling at a distribution level in a smart grid context,” *Energy*, vol. 85, pp. 236–250, 2015.
- [23] E. H. Trinklein, G. G. Parker, R. D. Robinett, and W. W. Weaver, “Towards online optimal power flow of a networked dc microgrid system,” *IEEE Journal of Emerging and Selected Topics in Power Electronics*, vol. PP, no. 99, 2017.
- [24] S. Fazlollahi, G. Becker, A. Ashouri, and F. Maréchal, “Multi-objective, multi-period optimization of district energy systems: IV-A case study,” *Energy*, vol. 84, pp. 365–381, 2015.

- [25] M. Ghasemi, S. Ghavidel, M. M. Ghanbarian, M. Gharibzadeh, and A. A. Vahed, “Multi-objective optimal power flow considering the cost, emission, voltage deviation and power losses using multi-objective modified imperialist competitive algorithm,” *Energy*, vol. 78, pp. 276–289, 2014.
- [26] D. Neves and C. A. Silva, “Optimal electricity dispatch on isolated mini-grids using a demand response strategy for thermal storage backup with genetic algorithms,” *Energy*, vol. 82, pp. 436–445, 2015.
- [27] M. Elsied, A. Oukaour, H. Gualous, and R. Hassan, “Energy management and optimization in microgrid system based on green energy,” *Energy*, vol. 84, pp. 139–151, 2015.
- [28] E. H. Trinklein and G. G. Parker, “Optimal control of a networked ship microgrid,” in *Advanced Machinery Technology Symposium (AMTS) 2016*. American Society of Naval Engineers (ANSE), 2016.
- [29] Y. Guan, J. C. Vasquez, and J. M. Guerrero, “A simple autonomous current-sharing control strategy for fast dynamic response of parallel inverters in islanded microgrids,” in *2014 IEEE International Energy Conference (ENERGYCON)*, 2014, pp. 182–188.
- [30] L. Meng, T. Dragicevic, J. Roldan-Perez, J. C. Vasquez, and J. M. Guerrero,

- “Modeling and sensitivity study of consensus algorithm-based distributed hierarchical control for dc microgrids,” *IEEE Transactions on Smart Grid*, vol. 7, no. 3, pp. 1504–1515, 2016.
- [31] M. Razmara, M. Maasoumy, M. Shahbakhti, and R. Robinett, “Optimal exergy control of building HVAC system,” *Applied Energy*, vol. 156, no. Supplement C, pp. 555 – 565, 2015.
- [32] M. Razmara, M. Bidarvatan, M. Shahbakhti, and R. R. III, “Optimal exergy-based control of internal combustion engines,” *Applied Energy*, vol. 183, pp. 1389 – 1403, 2016.
- [33] E. H. Trinklein, G. G. Parker, and T. J. McCoy, in *Modeling, Optimization, and Control of Ship Energy Systems Using Exergy Methods*. 2ND INTERNATIONAL CONFERENCE ON MODELLING AND OPTIMISATION OF SHIP ENERGY SYSTEMS, 2019, manuscript submitted for publication.
- [34] A. Chaboki, L. Thurmond, G. Grater, D. Bauer, F. Beach, and D. Clayton, “Integration of electromagnetic rail gun into future electric warships,” in *High Powered Weapons Systems for Electric Ship Conference*, 2004.
- [35] H. Obering and M. Gunzinger, “July 28, 2015 directed energy summit summary report,” August 2015.
- [36] R. D. Robinett III and D. G. Wilson, *Nonlinear power flow control design*:

utilizing exergy, entropy, static and dynamic stability, and Lyapunov analysis.

Springer Science & Business Media, 2011.

- [37] D. G. Wilson, J. C. Neely, M. Cook, S. F. Glover, J. Young, R. D. Robinett *et al.*, “Hamiltonian control design for dc microgrids with stochastic sources and loads with applications,” in *Power Electronics, Electrical Drives, Automation and Motion (SPEEDAM), 2014 International Symposium on.* IEEE, 2014, pp. 1264–1271.
- [38] W. W. Weaver and G. G. Parker, “Real-time hardware-in-the-loop simulation for optimal dc microgrid control development,” in *Control and Modeling for Power Electronics (COMPEL), 2014 IEEE 15th Workshop on.* IEEE, 2014, pp. 1–6.
- [39] G. Parker, W. Weaver, R. Robinett, and D. Wilson, “Optimal dc microgrid power apportionment and closed loop storage control to mitigate source and load transients,” in *Proceedings of Resilience Week 2015.* IEEE, 2015.
- [40] M. Harfman Todorovic, L. Palma, and P. Enjeti, “Design of a wide input range DC-DC converter with a robust power control scheme suitable for fuel cell power conversion,” *IEEE Transactions on Industrial Electronics*, vol. 55, no. 3, pp. 1247–1255, 2008.
- [41] Z. Amjadi and S. Williamson, “Power-electronics-based solutions for plug-in hybrid electric vehicle energy storage and management systems,” *IEEE Transactions on Industrial Electronics*, vol. 57, no. 2, pp. 608–616, 2010.



- [42] R. Bellman, *Dynamic Programming*. New Jersey, USA: Princeton University Press, 1957.
- [43] E. H. Trinklein, G. G. Parker, R. D. Robinett, and W. W. Weaver, “Toward online optimal power flow of a networked dc microgrid system,” *IEEE Journal of Emerging and Selected Topics in Power Electronics*, vol. 5, no. 3, pp. 949–959, 2017.
- [44] H. Sira-Ramírez and R. Silva-Ortigoza, *Control design techniques in power electronics devices*. Springer Science & Business Media, 2006.
- [45] H. Schaub and J. L. Junkins, *Analytical mechanics of space systems*. American Institute of Aeronautics and Astronautics, 2003.
- [46] E. H. Trinklein, G. G. Parker, T. J. McCoy, R. D. Robinett III, and W. W. Weaver Jr., “Reduced order multi-domain modeling of shipboard systems for exergy-based control investigations,” *Naval Engineers Journal*, vol. 103, no. 3, pp. 45–63, 2018.
- [47] W. A. Hudson and M. L. Levin, “Integrated aircraft fuel thermal management system,” 1988, US Patent 4,776,536.
- [48] G. G. Parker, E. H. Trinklein, R. D. Robinett III, and T. J. McCoy, in *Exergy Analysis of Ship Power Systems*. 14th International Naval Engineering Conference, 2018.

Appendix A


Letters of Permission

A.1 Letter of Permission for Chapter 2

11/19/2018 Rightslink® by Copyright Clearance Center



[Home](#) [Create Account](#) [Help](#)



Requesting permission to reuse content from an IEEE publication

Title: Toward Online Optimal Power Flow of a Networked DC Microgrid System

Author: Eddy H. Trinklein

Publication: Emerging and Selected Topics in Power Electronics, IEEE Journal of

Publisher: IEEE

Date: Sept. 2017

Copyright © 2017, IEEE

LOGIN

If you're a [copyright.com](#) user, you can login to RightsLink using your copyright.com credentials.

Already a [RightsLink](#) user or want to [learn more?](#)

Thesis / Dissertation Reuse

The IEEE does not require individuals working on a thesis to obtain a formal reuse license, however, you may print out this statement to be used as a permission grant:

Requirements to be followed when using any portion (e.g., figure, graph, table, or textual material) of an IEEE copyrighted paper in a thesis:

- 1) In the case of textual material (e.g., using short quotes or referring to the work within these papers) users must give full credit to the original source (author, paper, publication) followed by the IEEE copyright line © 2011 IEEE.
- 2) In the case of illustrations or tabular material, we require that the copyright line © [Year of original publication] IEEE appear prominently with each reprinted figure and/or table.
- 3) If a substantial portion of the original paper is to be used, and if you are not the senior author, also obtain the senior author's approval.

Requirements to be followed when using an entire IEEE copyrighted paper in a thesis:

- 1) The following IEEE copyright/ credit notice should be placed prominently in the references: © [year of original publication] IEEE. Reprinted, with permission, from [author names, paper title, IEEE publication title, and month/year of publication]
- 2) Only the accepted version of an IEEE copyrighted paper can be used when posting the paper or your thesis on-line.
- 3) In placing the thesis on the author's university website, please display the following message in a prominent place on the website: In reference to IEEE copyrighted material which is used with permission in this thesis, the IEEE does not endorse any of [university/educational entity's name goes here]'s products or services. Internal or personal use of this material is permitted. If interested in reprinting/republishing IEEE copyrighted material for advertising or promotional purposes or for creating new collective works for resale or redistribution, please go to http://www.ieee.org/publications_standards/publications/rights/rights_link.html to learn how to obtain a License from RightsLink.

If applicable, University Microfilms and/or ProQuest Library, or the Archives of Canada may supply single copies of the dissertation.

[BACK](#) [CLOSE WINDOW](#)

Copyright © 2018 [Copyright Clearance Center, Inc.](#) All Rights Reserved. [Privacy statement](#). [Terms and Conditions](#).
Comments? We would like to hear from you. E-mail us at customercare@copyright.com

Figure A.1: Permission Grant for Chapter 2

Appendix B

Support Matrices and Notation

For Chapter 3

For both boost and buck architecture,

$$\mathbf{M} = \begin{bmatrix} L_{1,1} & \dots & 0 & 0 & \dots & 0 & 0 & \dots & 0 & 0 & \dots & 0 \\ 0 & \ddots & 0 & 0 & \dots & 0 & 0 & \dots & 0 & 0 & \dots & 0 \\ 0 & \dots & L_{m,p} & 0 & \dots & 0 & 0 & \dots & 0 & 0 & \dots & 0 \\ 0 & \dots & 0 & L_{C_{1,1}} & \dots & 0 & 0 & \dots & 0 & 0 & \dots & 0 \\ 0 & \dots & 0 & 0 & \ddots & 0 & 0 & \dots & 0 & 0 & \dots & 0 \\ 0 & \dots & 0 & 0 & \dots & L_{C_{p,q}} & 0 & \dots & 0 & 0 & \dots & 0 \\ 0 & \dots & 0 & 0 & \dots & 0 & C_{B,1} & \dots & 0 & 0 & \dots & 0 \\ 0 & \dots & 0 & 0 & \dots & 0 & 0 & \ddots & 0 & 0 & \dots & 0 \\ 0 & \dots & 0 & 0 & \dots & 0 & 0 & \dots & C_{B,p} & 0 & \dots & 0 \\ 0 & \dots & 0 & 0 & \dots & 0 & 0 & \dots & 0 & C_{T,1} & \dots & 0 \\ 0 & \dots & 0 & 0 & \dots & 0 & 0 & \dots & 0 & 0 & \ddots & 0 \\ 0 & \dots & 0 & 0 & \dots & 0 & 0 & \dots & 0 & 0 & \dots & C_{T,q} \end{bmatrix}, \quad (\text{B.1})$$

For buck architecture,

$$\mathbf{R} = \begin{bmatrix} -R_{1,1} & \dots & 0 & 0 & \dots & 0 & -1 & \dots & 0 & 0 & \dots & 0 \\ \vdots & \ddots & \vdots & \vdots & \dots & \vdots & \vdots & \ddots & \vdots & \vdots & \dots & \vdots \\ 0 & \dots & -R_{m,p} & 0 & \dots & 0 & 0 & \dots & -1 & 0 & \dots & 0 \\ 0 & \dots & 0 & -R_{C_{1,1}} & \dots & 0 & 1-D_{C_{1,1}} & \dots & 0 & -D_{C_{1,1}} & \dots & 0 \\ \vdots & \dots & \vdots & \vdots & \ddots & \vdots & \vdots & \ddots & \vdots & \vdots & \ddots & \vdots \\ 0 & \dots & 0 & 0 & \dots & -R_{C_{p,q}} & 0 & \dots & 1-D_{C_{p,q}} & 0 & \dots & -D_{C_{p,q}} \\ 1 & \dots & 0 & -(1-D_{C_{1,1}}) & \dots & 0 & -R_1^* & \dots & 0 & 0 & \dots & 0 \\ \vdots & \ddots & \vdots & \vdots & \ddots & \vdots & \vdots & \ddots & \vdots & \vdots & \dots & \vdots \\ 0 & \dots & 1 & 0 & \dots & -(1-D_{C_{p,q}}) & 0 & \dots & -R_P^* & 0 & \dots & 0 \\ 0 & \dots & 0 & D_{C_{1,1}} & \dots & 0 & 0 & \dots & 0 & -1/R_{T,1} & \dots & 0 \\ \vdots & \dots & \vdots & \vdots & \ddots & \vdots & \vdots & \dots & \vdots & 0 & \ddots & \vdots \\ 0 & \dots & 0 & 0 & \dots & D_{C_{p,q}} & 0 & \dots & 0 & 0 & \dots & -1/R_{T,q} \end{bmatrix}, \quad (\text{B.2})$$

and for boost architecture,

$$\mathbf{R} = \begin{bmatrix} -R_{1,1} & \dots & 0 & 0 & \dots & 0 & -D_{1,1} & \dots & 0 & 0 & \dots & 0 \\ \vdots & \ddots & \vdots & \vdots & \dots & \vdots & \vdots & \ddots & \vdots & \vdots & \dots & \vdots \\ 0 & \dots & -R_{m,p} & 0 & \dots & 0 & 0 & \dots & -D_{m,p} & 0 & \dots & 0 \\ 0 & \dots & 0 & -R_{C_{1,1}} & \dots & 0 & 1-D_{C_{1,1}} & \dots & 0 & -D_{C_{1,1}} & \dots & 0 \\ \vdots & \dots & \vdots & \vdots & \ddots & \vdots & \vdots & \ddots & \vdots & \vdots & \ddots & \vdots \\ 0 & \dots & 0 & 0 & \dots & -R_{C_{p,q}} & 0 & \dots & 1-D_{C_{p,q}} & 0 & \dots & -D_{C_{p,q}} \\ D_{1,1} & \dots & 0 & -(1-D_{C_{1,1}}) & \dots & 0 & -R_1^* & \dots & 0 & 0 & \dots & 0 \\ \vdots & \ddots & \vdots & \vdots & \ddots & \vdots & \vdots & \ddots & \vdots & \vdots & \dots & \vdots \\ 0 & \dots & D_{m,p} & 0 & \dots & -(1-D_{C_{p,q}}) & 0 & \dots & -R_P^* & 0 & \dots & 0 \\ 0 & \dots & 0 & D_{C_{1,1}} & \dots & 0 & 0 & \dots & 0 & -1/R_{T,1} & \dots & 0 \\ \vdots & \dots & \vdots & \vdots & \ddots & \vdots & \vdots & \dots & \vdots & 0 & \ddots & \vdots \\ 0 & \dots & 0 & 0 & \dots & D_{C_{p,q}} & 0 & \dots & 0 & 0 & \dots & -1/R_{T,q} \end{bmatrix}, \quad (\text{B.3})$$

where

$$-R_j^* = -\left(\frac{1}{R_{B,j}} + \sum_{i=1}^{m_{L,j}} \frac{1}{R_{L,i}}\right). \quad (\text{B.4})$$

\mathbf{R} can be decomposed into a diagonal matrix, $\bar{\mathbf{R}}$, and skew-symmetric matrix, $\tilde{\mathbf{R}}$.

This results in the same $\bar{\mathbf{R}}$ for both buck and boost architectures,

$$\bar{\mathbf{R}} = \begin{bmatrix} -R_{1,1} & \dots & 0 & 0 & \dots & 0 & 0 & \dots & 0 & 0 & \dots & 0 \\ \vdots & \ddots & \vdots & \vdots & \dots & \vdots & \vdots & \dots & \vdots & 0 & \dots & \vdots \\ 0 & \dots & -R_{m,p} & 0 & \dots & 0 & 0 & \dots & 0 & 0 & \dots & 0 \\ 0 & \dots & 0 & -R_{C_{1,1}} & \dots & 0 & 0 & \dots & 0 & 0 & \dots & 0 \\ \vdots & \dots & 0 & 0 & \ddots & 0 & 0 & \dots & 0 & 0 & \dots & 0 \\ 0 & \dots & 0 & 0 & \dots & -R_{C_{p,q}} & 0 & \dots & 1 & 0 & \dots & 0 \\ 0 & \dots & 0 & 0 & \dots & 0 & -R_1^* & \dots & 0 & 0 & \dots & 0 \\ \vdots & \dots & 0 & 0 & \dots & 0 & 0 & \ddots & 0 & 0 & \dots & 0 \\ 0 & \dots & 0 & 0 & \dots & 0 & 0 & \dots & -R_p^* & 0 & \dots & 0 \\ 0 & \dots & 0 & 0 & \dots & 0 & 0 & \dots & 0 & -1/R_{T,1} & \dots & 0 \\ \vdots & \dots & 0 & 0 & \dots & 0 & 0 & \dots & 0 & 0 & \ddots & 0 \\ 0 & \dots & 0 & 0 & \dots & 0 & 0 & \dots & 0 & 0 & \dots & -1/R_{T,q} \end{bmatrix}. \quad (\text{B.5})$$

For buck architecture,

$$\tilde{\mathbf{R}} = \begin{bmatrix} 0 & \dots & 0 & 0 & \dots & 0 & -1 & \dots & 0 & 0 & \dots & 0 \\ \vdots & \ddots & \vdots & \vdots & \dots & \vdots & \vdots & \ddots & \vdots & \vdots & \dots & \vdots \\ 0 & \dots & 0 & 0 & \dots & 0 & 0 & \dots & -1 & 0 & \dots & 0 \\ 0 & \dots & 0 & 0 & \dots & 0 & (1-D_{C_{1,1}}) & \dots & 0 & -D_{C_{1,1}} & \dots & 0 \\ \vdots & \vdots & \vdots & \vdots & \ddots & \vdots & \vdots & \ddots & \vdots & \vdots & \dots & \vdots \\ 0 & \dots & 0 & 0 & \dots & 0 & 0 & \dots & (1-D_{C_{p,q}}) & 0 & \dots & -D_{C_{p,q}} \\ 1 & \dots & 0 & -(1-D_{C_{1,1}}) & \dots & 0 & 0 & \dots & 0 & 0 & \dots & 0 \\ \vdots & \vdots & \vdots & \vdots & \ddots & \vdots & \vdots & \ddots & \vdots & \vdots & \dots & \vdots \\ 0 & \dots & 1 & 0 & \dots & -(1-D_{C_{p,q}}) & 0 & \dots & 0 & 0 & \dots & 0 \\ 0 & \dots & 0 & D_{C_{1,1}} & \dots & 0 & \vdots & \dots & 0 & 0 & \dots & 0 \\ \vdots & \vdots & \vdots & \vdots & \ddots & \vdots & \vdots & \ddots & \vdots & \vdots & \dots & \vdots \\ 0 & \dots & 0 & 0 & \dots & D_{C_{p,q}} & 0 & \dots & 0 & 0 & \dots & 0 \end{bmatrix}, \quad (\text{B.6})$$

and for boost architecture,

$$\tilde{\mathbf{R}} = \begin{bmatrix} 0 & \dots & 0 & 0 & \dots & 0 & -D_{1,1} & \dots & 0 & 0 & \dots & 0 \\ \vdots & \ddots & \vdots & \vdots & \ddots & \vdots & \vdots & \ddots & \vdots & \vdots & \ddots & \vdots \\ 0 & \dots & 0 & 0 & \dots & 0 & 0 & \dots & -D_{m,p} & 0 & \dots & 0 \\ 0 & \dots & 0 & 0 & \dots & 0 & (1-D_{C_{1,1}}) & \dots & 0 & -D_{C_{1,1}} & \dots & 0 \\ \vdots & \dots & \vdots & \vdots & \ddots & \vdots & \vdots & \ddots & \vdots & \vdots & \ddots & \vdots \\ 0 & \dots & 0 & 0 & \dots & 0 & 0 & \dots & (1-D_{C_{p,q}}) & 0 & \dots & -D_{C_{p,q}} \\ D_{1,1} & \dots & 0 & -(1-D_{C_{1,1}}) & \dots & 0 & 0 & \dots & 0 & 0 & \dots & 0 \\ \vdots & \ddots & \vdots & \vdots & \ddots & \vdots & \vdots & \ddots & \vdots & \vdots & \ddots & \vdots \\ 0 & \dots & D_{m,p} & 0 & \dots & -(1-D_{C_{p,q}}) & 0 & \dots & 0 & 0 & \dots & 0 \\ 0 & \dots & 0 & D_{C_{1,1}} & \dots & 0 & \vdots & \dots & 0 & 0 & \dots & 0 \\ \vdots & \dots & \vdots & \vdots & \ddots & \vdots & \vdots & \ddots & \vdots & \vdots & \ddots & \vdots \\ 0 & \dots & 0 & 0 & \dots & D_{C_{p,q}} & 0 & \dots & 0 & 0 & \dots & 0 \end{bmatrix}. \quad (\text{B.7})$$

The final differences between the architectures exist in the \mathbf{D}^T and \mathbf{B}^T matrices. For buck converters,

$$\mathbf{B}^T = \mathbf{D}^T = \begin{bmatrix} D_{1,1} & \dots & 0 & 0 & \dots & 0 & 0 & \dots & 0 & 0 & \dots & 0 \\ 0 & \ddots & 0 & 0 & \dots & 0 & 0 & \dots & 0 & 0 & \dots & 0 \\ 0 & \dots & D_{m,p} & 0 & \dots & 0 & 0 & \dots & 0 & 0 & \dots & 0 \\ 0 & \dots & 0 & 0 & \dots & 0 & 0 & \dots & 0 & 0 & \dots & 0 \\ 0 & \dots & 0 & 0 & \ddots & 0 & 0 & \dots & 0 & 0 & \dots & 0 \\ 0 & \dots & 0 & 0 & \dots & 0 & 0 & \dots & 0 & 0 & \dots & 0 \\ 0 & \dots & 0 & 0 & \dots & 0 & 0 & \dots & 0 & 0 & \dots & 0 \\ 0 & \dots & 0 & 0 & \dots & 0 & 0 & \dots & 0 & 0 & \dots & 0 \\ 0 & \dots & 0 & 0 & \dots & 0 & 0 & \dots & 0 & 0 & \ddots & 0 \\ 0 & \dots & 0 & 0 & \dots & 0 & 0 & \dots & 0 & 0 & \dots & 0 \end{bmatrix}. \quad (\text{B.8})$$

For boost converters, \mathbf{B}^T and \mathbf{D}^T are both the identity matrix.

Appendix C

Support Tables and Circuit

Schematics for Chapter 4

Table C.1
Opal-RT to Typhoon HIL 600 PWM Connections

Signal	D-IN	Frequency (Hz)
D_{HPS}	Pin 1	9999
D_{LPS}	Pin 2	10009
$1 - D_{MBFC}$	Pin 3	9998
D_{MBFC}	Pin 4	9998
$1 - D_{HPFC}$	Pin 5	10005
D_{HPFC}	Pin 6	10005

Table C.2
Opal-RT to Typhoon HIL 600 Analog Connections

Signal	A-IN	Signal Scaling
i_{pl}	Pin 1	$[-5, 5]$ (V) to $[0, 400]$ (A)
i_m	Pin 2	$[-5, 5]$ (V) to $[0, 5]$ (A)
u_{HESM}	Pin 3	$[-5, 5]$ (V) to $[-600, 600]$ (A)
u_{EAU}	Pin 4	$[-5, 5]$ (V) to $[-20, 20]$ (A)
Signal	A-OUT	Signal Scaling
i_{HPS}	Pin 1	$[10, 70]$ (A) to $[-5, 5]$ (V)
i_{LPS}	Pin 2	$[0, 400]$ (A) to $[-5, 5]$ (V)
v_{MB}	Pin 3	$[230, 310]$ (V) to $[-5, 5]$ (V)
v_{HP}	Pin 4	$[230, 310]$ (V) to $[-5, 5]$ (V)
i_{MBFC}	Pin 5	$[-75, 75]$ (A) to $[-5, 5]$ (V)
i_{HPFC}	Pin 6	$[-75, 75]$ (A) to $[-5, 5]$ (V)
v_{FC}	Pin 7	$[230, 310]$ (V) to $[-5, 5]$ (V)

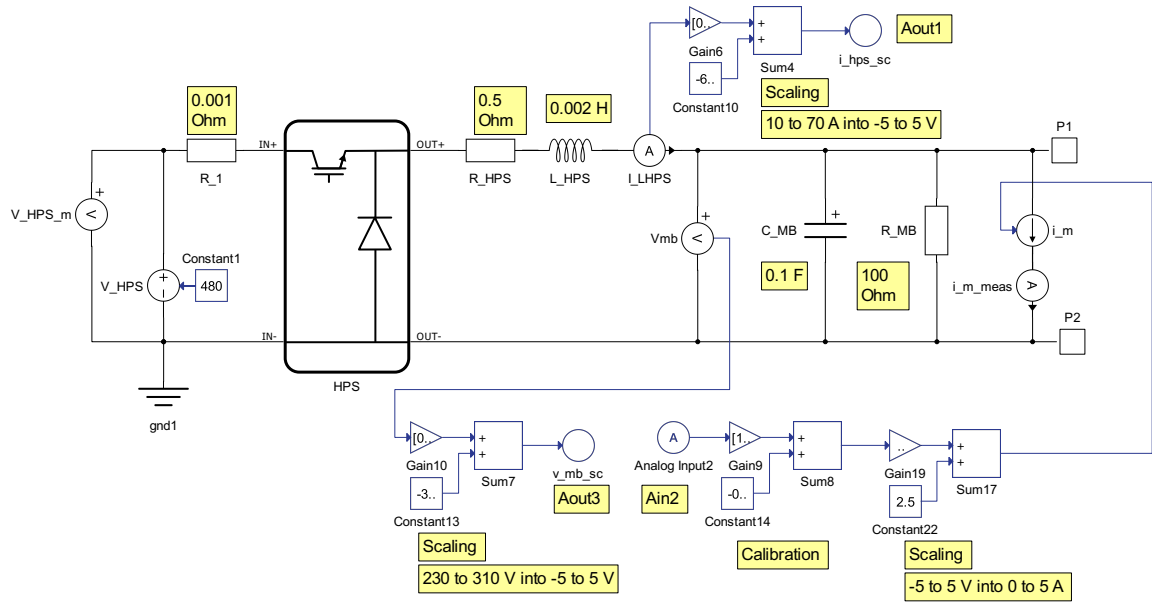


Figure C.1: Typhoon HIL 600 HPS Generator & MB Bus Schematic.

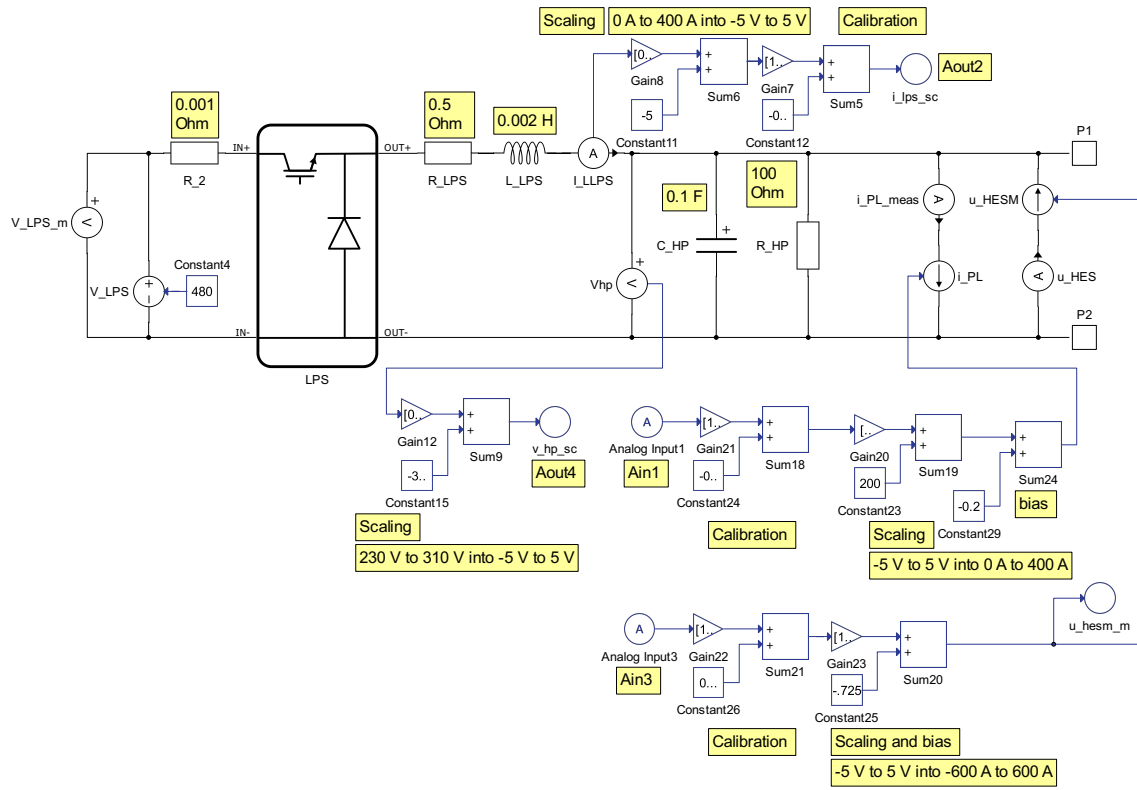


Figure C.2: Typhoon HIL 600 LPS Generator & HP Bus Schematic.

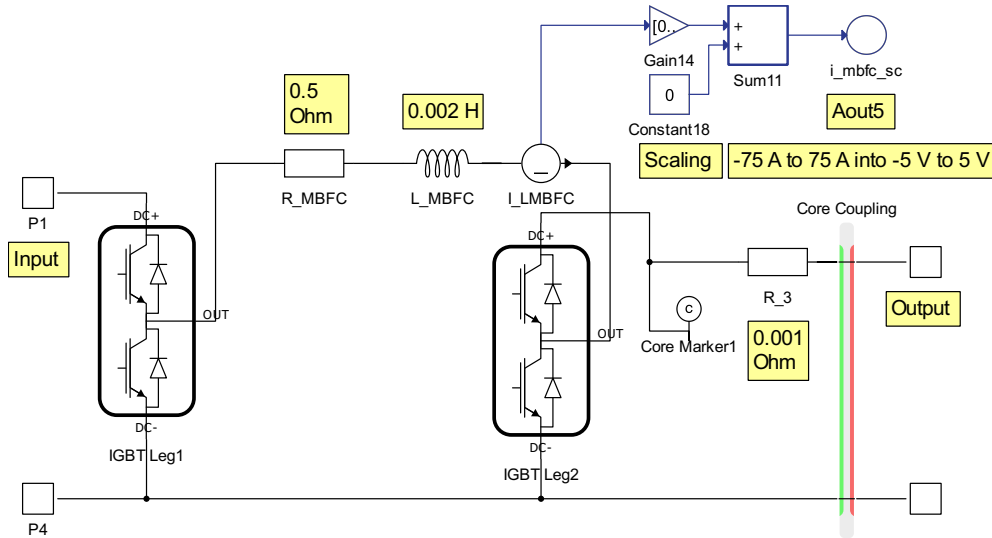


Figure C.3: Typhoon HIL 600 MBFC Power Converter Schematic.

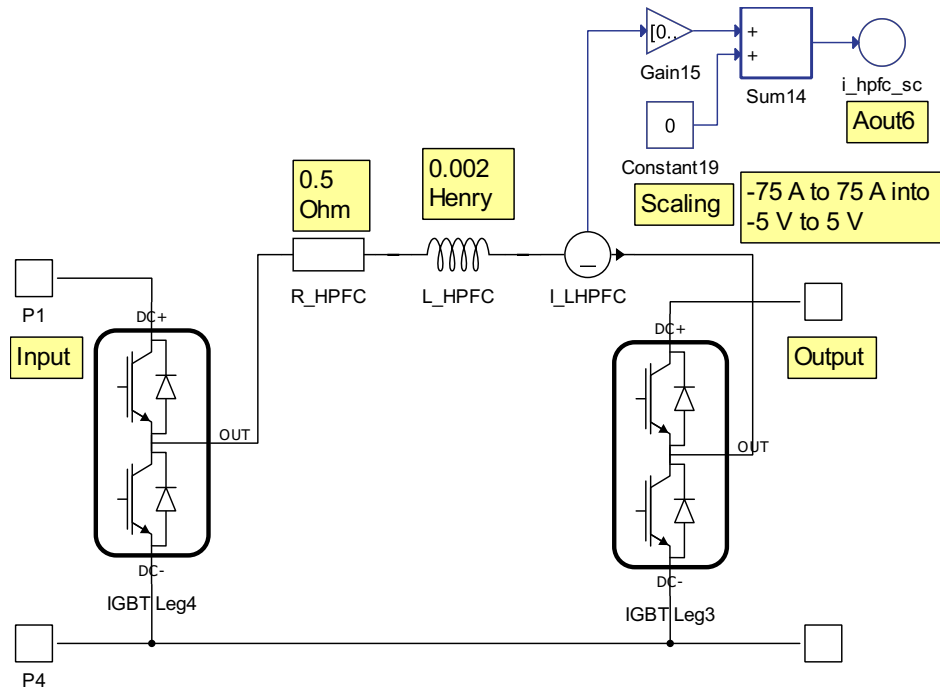


Figure C.4: Typhoon HIL 600 HPFC Power Converter Schematic.

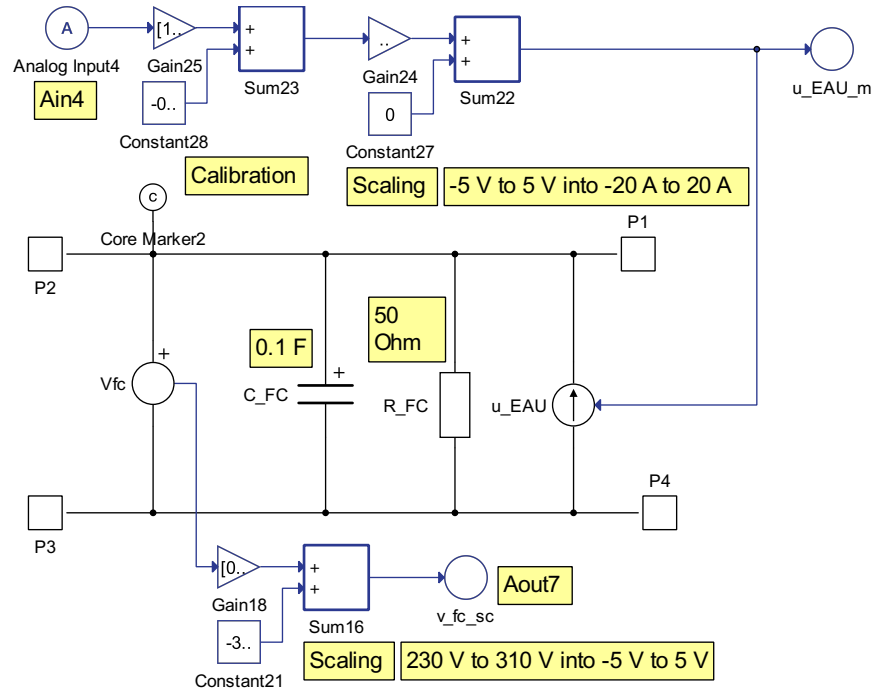


Figure C.5: Typhoon HIL 600 FC Bus Schematic.